MAGNETORESISTANCE AND SURFACE ACOUSTIC WAVES MEASUREMENTS OF QUANTUM MATERIALS

A Dissertation

Presented to the Faculty of the Graduate School

of Cornell University

in Partial Fulfillment of the Requirements for the Degree of

Doctor of Philosophy

by

Yawen Fang

August 2022

MAGNETORESISTANCE AND SURFACE ACOUSTIC WAVES MEASUREMENTS OF QUANTUM MATERIALS

Yawen Fang, Ph.D.

Cornell University 2022

This thesis consists of three separate parts. The first part of the thesis focuses on the quantum oscillation study of the quasiparticle properties of thin-film Sr_2RuO_4 grown on a $(LaAlO_3)_{0.29}$ $(SrAl_{1/2}Ta_{1/2}O_3)_{0.71}$ substrate. The second part concerns the magnetotransport study of the Fermi surface of the high-T_c cuprate, $La_{1.6-x}Nd_{0.4}Sr_xCuO_4$. The third part of the thesis focuses on the development of contactless, finite-wavelength quantum transport in high-quality 2D heterostructures using surface acoustic waves (SAWs).

In the first part of the thesis, first, we show that in clean materials where the mean free path of the electron is long compared to the cyclotron radius, the Shubikov-de Hass effect can be observed in these materials, and the quasiparticle properties, including the Fermi surface volumes, cyclotron effective masses, and quantum lifetimes, can be accurately determined from the quantum oscillation analysis. An extensive quantum oscillation analysis of thin-film Sr_2RuO_4 grown on an $(LaAlO_3)_{0.29}$-$(SrAl_{1/2}Ta_{1/2}O_3)_{0.71}$ substrate is presented. The transport lifetime is calculated by solving the semiclassical Boltzmann transport equation. We find that the transport lifetime is longer than the quantum lifetime, indicating that extended defects are the dominant source of quasiparticle scattering, confirmed by cross-sectional scanning transmission electron microscopy.

In the second part of the thesis, we show that with angle-dependent magnetoresistance (ADMR) measurement, the Fermi surface and the quasiparticle lifetime can also be accurately determined, in materials where the mean free path is short, and quantum oscillation cannot be observed with an achievable magnetic field. We perform a thorough angle-dependent study of the high-T_c cuprate, $La_{1.6-x}Nd_{0.4}Sr_xCuO_4$ at two dopings, one above

the critical doping and one below. Simulations of the ADMR are performed by numerically solving the Boltzmann transport equation. We find that the ADMR data can be described by a Fermi surface geometry consistent with angle-resolved photoemission data and a highly anisotropic scattering rate outside the pseudogap phase. In the pseudogap phase, we find that the ADMR is qualitatively different. We tested several scenarios, including quasiparticle scattering rate change and Fermi surface reconstruction. We find that the data is best described by a Fermi surface consisting of small, nodal hole pockets.

In the third part of the thesis, we focus on the development of SAW resonant cavities on $LiNbO_3$ substrates for contactless conductivity measurements in the quantum transport regime of 2D heterostructures. There are two major challenges, finding a suitable substrate, compatible with high-mobility device fabrication and electrostatic gating and increasing signal size. In this thesis, we try to address both of them. To address the first challenge, we analyze the basic property of SAWs and their interaction with a 2D conducting sample placed near the substrate surface and pick the piezoelectric material $LiNbO_3$ as substrate material. To address the second challenge, we compare the two ways of performing SAW measurement, using SAW delay lines and SAW resonators, and show that the resonant cavity geometry increases signal-to-noise by two orders of magnitude over the traditional delay-line geometry. Finally, we demonstrate that the substrate is compatible with high-mobility device fabrication and electrostatic gating, and the quantum transport regime is achieved with a detailed analysis of the quantum oscillations in the SAW cavity frequency in the quantum Hall regime of graphene.

BIOGRAPHICAL SKETCH

Yawen Fang was born in 1994 in the city of Guangzhou, China. During high school, seasons 1 & 2 of the popular TV series "the big bang theory" started her interest in physics and motivated her to work hard on studying science. This further led to the decision to major in physics at the Hong Kong University of science and technology, where she got a chance to gain experience in experimental research in physics. During her undergraduate, she got experience working on building numerical simulation code for modeling 2D Supramolecular assembly with Prof. Nian Lin at HKUST, performing data analysis on the simulation and experimental data from the Compact Muon Solenoid (CMS) at the Large Hadron Collider (LHC) with Prof. Steve Schnetzer at Rutgers, and building experiment setup for the measurement and performing bandstructure calculation of analog topological material with Prof. Wing Yim Tam and Prof. Che Ting Chan at HKUST. The exposure to various areas of physics using vastly different techniques turned out to be highly beneficial in her later Ph.D. research.

She started her Ph.D. in physics at Cornell University, where she joined Brad Ramshaw's research group as one of its first members in 2017. She primarily worked on three different projects. When she first started, she worked on quantum oscillation measurement and its analysis of topological materials. Then, she started her project on the angle-dependent magnetoresistance study on Nd-LSCO. At the same time, she also started working on the development of surface acoustic wave measurement techniques.

This document is dedicated to all Cornell graduate students.

ACKNOWLEDGEMENTS

During my six-year journey as a Ph.D. student, I have received help and support from many people, and this work would be impossible without them.

First and foremost, I want to thank my supervisor, Prof. Brad Ramshaw, for his invaluable advice, support, and guidance during my Ph.D. study. Brad has always been a great teacher and mentor since I joined the ground in 2017. I thank him for teaching me all the lab skills required for building a working experiment, ranging from polishing samples to micron-scale thickness by hand to soldering electronic components on circuit boards, the techniques for writing a clear scientific paper and making scientific presentations, and most importantly, the way of identifying new interesting problems and getting started. His optimism and enthusiasm toward fundamental research motivate me to dive deep and pay attention to details, without which I would not have made the findings presented in the thesis.

I am grateful to Prof. Kin Fai Mak and Prof. Michael Lawler for serving on my committee. The enlightening discussion with Fai on the surface acoustic wave (SAW) project led to our device's first design; without its success, we probably won't be so confident about the project.

I am thankful to our collaborator, Benyamin Davaji, for his help setting up the SAW experiment, his recipe for the SAW devices fabrication, and the multiple discussions on the SAW results. I also want to thank our collaborators, Yang Xu and Kaifei Kang. The conversations with them on the SAW result helped me understand the graphene data and bring insight into the device's design. I want to thank our collaborator, David Graf, for his help with the high magnetic field measurements in the NHMFL at Tallahassee. Moreover, I want to thank all the other people I had scientific collaborations and discussions with both within and outside Cornell.

I want to thank all the members of the Ramshaw Group, Sayak, Patrick, Florian, Avi, and Gael, for their help and support. It has been a great time sharing an office with and

learning from them.

Experiments are always working, and there are ups and downs during these six years of Ph.D. study. I am very grateful to have met such a group of supportive friends; they make this long and tough journey a lot more fun and enjoyable. Without their support, I could not have gone through all of this.

Finally, I want to thank my parents for their unconditional love and support for me. They have always been very supportive of all the decisions I made and encouraged me to pursue my dream without worrying too much about the outcome. I really can't thank them enough.

CONTENTS

LIST OF TABLES

LIST OF FIGURES

CHAPTER 1

INTRODUCTION

In recent years, quantum material research has been the absolute focus in the condensed matter physics community. On a trivial level, all materials can be described by the law of quantum mechanics, which relates to how atoms bond and electrons interact. However, in quantum materials, the electronic or magnetic properties can no longer be described by classical particles or calculations. For example, in graphene, where the electrons behave like massless Dirac fermions, originally predicted to occur at unreachable high energy [15]. Some examples of quantum materials are unconventional superconductors, topological semimetals, quantum spin liquids, graphene, and 2D heterostructures. In most of these materials, electrons can no longer be considered independent particles and, driven by strong interaction, give rise to collective excitations known as quasiparticles, acquiring completely different properties from regular electrons. Research on quantum material is of great interest for mainly two reasons.

One of the reasons is that in these quantum material systems, the interaction and entanglement between the $\sim 10^{23}$ electrons give rise to emergent phenomena, and developing a macroscopic understanding of such a complex system with many degrees of freedom is a fundamentally challenging and interesting problem. For example, since its discovery in 1986, the cuprate superconductors have been one of the most studied quantum materials. The strong correlation and interaction between electrons in the material give rise to an extremely rich phase diagram as a function of doping, including the superconductivity phase with the record high transition temperature under ambient pressure. Their intriguing superconducting and normal state properties challenged the conventional understanding of solids.

The second reason is that many quantum materials have exotic electronic and magnetic properties, and understanding the governing physics may allow further tailoring of their al-

ready rich properties, enabling completely new applications, like new routes toward building a quantum computer. An example would be the study of thin-film Sr_2RuO_4. As a chiral spin-triplet superconductor candidate, it has possible application to quantum computation, as chiral spin-triplet superconductors are predicted to host Majorana zero modes in their vortices. Although it has been shown that the bulk material is essentially not a spin-triplet superconductor [16], it might still be possible to push Sr_2RuO_4 into a spin-triplet state by applying biaxial strain via substrate engineer of epitaxially grown films [17, 18].

Understanding these quantum materials requires understanding their quasiparticles' properties and Fermi surfaces. Although interactions and correlations can be strong in these quantum materials, most of them can still be described with Landau's Fermi liquid theory, a theoretical model of interacting fermions. The idea is that, at sufficiently low temperature, the quasiparticles in the interacting system can still be thought of as non-interacting fermions, with renormalized properties, such as the quasiparticle mass, representing the collective interactions of the system. However, many quantum materials have shown non-Fermi liquid behavior in recent years. For example, in one of the materials studied in this thesis, a hole-doped cuprate $La_{1.6-x}Nd_{0.4}Sr_xCuO_4$, at a doping p = 0.24, the resistivity as a function of temperature is linear down to the lowest measured temperatures, violating the standard quadratic temperature dependence expected of Fermi liquid theory. It has been shown that the Fermi surface information is still very useful in understanding the non-Fermi liquid behavior [19].

One of the most powerful tools that provide information on quasiparticle properties and their Fermi surfaces is quantum oscillation measurements. However, the observation of quantum oscillations requires the mean free path of the quasiparticles to be long compared to the cyclotron radius. When the mean free path is short and the quantum oscillation can not be observed, the Fermi surfaces and the quasiparticle lifetime can also be measured with the angle-dependent magnetoresistance (ADMR) measurement. The two techniques can be

combined together, revealing detailed information on the Fermi surfaces and quasiparticle properties, forming the basis for understanding other quantum phenomena in the quantum materials. An excellent example of using the two techniques to extract detailed information about the Fermi surface and quasiparticles properties and using that information in disentangling issues relevant to the unconventional superconductivity in Sr_2RuO_4 is given in Bergemann *et al.* [20].

In recent years, 2D material has emerged as a relatively new family of quantum materials compared to the semiconductor-based 2D electron gas system in the quantum hall regime and 3D strongly correlated materials like cuprates. Many similar quantum collective phenomena have been discovered in 2D heterostructures, such as the quantum Hall effect, the fractional quantum Hall effect, superconductivity, and quantum critical behavior. Moreover, it is possible to engineer new 2D devices with emergent exotic properties by stacking these atomically thin 2D materials with different properties or twisting them relative to one another, opening opportunities to design and build new quantum devices.

One way to start understanding these 2D systems is to develop new probes on top of the well-developed experimental tools for studying other "old " quantum materials. Techniques like angle-resolved photoemission spectroscopy (ARPES) studies and scanning tunneling microscopes (STM) have been some of the most powerful tools in studying strongly correlated physics in bulk/ thin-film quantum materials. They have been adapted for probing the 2D heterostructures and help gain valuable insight into understanding these systems [21, 22].

The surface acoustic waves (SAWs) technique has been a successful probe in studying the electron correlation and interaction in GaAs/ AlGaAs 2D electron system in the quantum Hall and the fractional quantum Hall regime. Sound waves traveling across the surface (SAWs) of a piezoelectric material create an oscillating electric field at the wavelength of the sound, ranging from tens of microns to tens of nanometers, and the interaction between this electric field and the 2D electron system results in a change in the velocity and attenuation

of the SAWs. Thus, the conductivity of the nearby 2D electron system at a finite wavelength can be obtained by measuring the change in sound velocity and attenuation.

Here is one of the examples of the physical discovery made with this technique. In the fractional quantum hall regime, at the filling factor 1/2, each electron combined with two flux quanta forms composite fermions. As all the magnetic field has been taken into account in forming composite fermions, the resulting composite particles experience a vanishing effective magnetic field; hence, a compressible Fermi sea of composite fermions is formed. Near the filling factor 1/2, using SAWs with wavelength below one micron, the geometric resonance of the composite fermions' cyclotron orbit and the ultrasound wavelength allow measurements of the composite fermion's Fermi wavevector, which is inaccessible with any other techniques [23].

SAWs would be a unique technique for 2D heterostructures for several reasons: it measures the conductivity of the sample without ohmic contacts, measures the bulk conductivity at a finite wavelength, and is compatible with low temperature and high magnetic fields. It would be particularly useful in measuring samples, where it can be difficult to make electrical contact and where there are emergent and engineered length scales such as charge density wavelengths and Moirs periodicities. There are also various theoretical predictions for wavelength-dependent quantum phenomena that can be probed with SAWs, including the search for the crossover from Dirac to Schrodinger-like behavior in the longitudinal conductivity of graphene [24] and measuring the SAW attenuation of a twisted bilayer graphene device as a function of chemical potential in search of non-Fermi-liquid signatures [25].

1.1 Thesis layout

This thesis is organized as follows.

In Chapter 2, we present the first quantum oscillations analysis in superconducting thin

films of Sr_2RuO_4 and determine the Fermi surface volumes, the effective cyclotron masses, and both the transport and quantum quasiparticle lifetimes. We find that the transport lifetimes are longer than the quantum lifetimes, indicating that extended defects are the dominant quasiparticle scattering source, which are then observed and characterized using cross-sectional scanning transmission electron microscopy.

In Chapter 3, we present the first ADMR measurement of high-temperature superconductors, cuprates, in the pseudogap phase, in the regime of $T- > 0$ without superconductivity. First, we calibrate our measurement technique with the ADMR analysis in Nd-LSCO at $p = 0.24$, above the critical doping p^* and outside the pseudogap phase. We find the ADMR data can be perfectly reproduced in a numerical simulation of the Boltzmann transport equation, with a Fermi surface geometry that is in excellent agreement with angle-resolved photoemission data. We then measure ADMR at $p = 0.21$, below p^* and inside the pseudogap phase. The data are qualitatively different from the data p $p = 0.24$. We try different scattering rate models and Fermi surface models to fit the data and find that only the model with a reconstruction of the Fermi surface by a $Q = (\pi, \pi)$ wavevector reproduces the data.

In Chapter 4, we present the development of SAW resonant cavities using $LiNbO_3$ substrates for contactless conductivity measurements at a finite wavelength of 2D heterostructures. First, we detail how SAW interacts with a 2D conducting sample nearby and the conversion between the measured quantities, sound velocity and attenuation, and the conductivity of the 2D conducting sample. Then, we compare two experimental setups, SAW delay lines and resonant cavity, showing that the resonant cavity geometry increases the signal-to-noise ratio by three orders of magnitude over the delay line geometry. Several measurement techniques for the characterization and measurement of SAW resonators are discussed. This is followed by a discussion on the design and fabrication of two-port SAW resonators. Then, we detail two finite element models for the simulation of the interaction between the SAWs and samples and the effect of critical design parameters on the per-

formance of resonators. Finally, we present our measurement results for several hexagonal boron nitrides (hBN) encapsulated graphene heterostructures.

CHAPTER 2

QUANTUM OSCILLATIONS AND QUASIPARTICLE PROPERTIES OF THIN FILM Sr_2RuO_4

This chapter is adapted from a Phys. Rev. B paper, Quantum oscillations and quasiparticle properties of thin film Sr_2RuO_4, with Hari P. Nair, Ludi Miao, Berit Goodge, Nathaniel J. Schreiber, Jacob P. Ruf, Lena F. Kourkoutis, Kyle M. Shen, Darrell G. Schlom, and B. J. Ramshaw.[26]

We measure the Shubnikov-de Haas effect in thin-film Sr_2RuO_4 grown on an $(LaAlO_3)_{0.29}$-$(SrAl_{1/2}Ta_{1/2}O_3)_{0.71}$ substrate. We detect all three known Fermi surfaces and extract the Fermi surface volumes, cyclotron effective masses, and quantum lifetimes. We show that the electronic structure is nearly identical to that of single-crystal Sr_2RuO_4, and that the quasiparticle lifetime is consistent with the T_c of comparably clean, single-crystal Sr_2RuO_4. Unlike single-crystal Sr_2RuO_4, where the quantum and transport lifetimes are roughly equal, we find that the transport lifetime is 1.3 ± 0.1 times longer than the quantum lifetime. This may suggest that extended (rather than point) defects could be the dominant source of quasiparticle scattering in these films. To test this hypothesis, we perform cross-sectional scanning transmission electron microscopy and find that out-of-phase boundaries extending the entire thickness of the film occur with a density that is consistent with the quantum mean free path. The long quasiparticle lifetimes make these films ideal for studying the unconventional superconducting state in Sr_2RuO_4 through the fabrication of devices—such as planar tunnel junctions and superconducting quantum interference devices.

2.1 Introduction

Sr_2RuO_4 was long thought to be a $p-$wave superconductor, but recently revised nuclear magnetic resonance (NMR) measurements find a substantial decrease in the Knight shift across the superconducting transition temperature T_c [27], essentially ruling out all spin-triplet pairing states. While the details of the superconducting state are far from settled [28, 29], it appears that single-crystal Sr_2RuO_4 is not a $p_x + ip_y$ superconductor. It may be possible, however, that multiple superconducting order parameters lie nearby in energy [30, 31], suggesting that the application of the right tuning parameter could push Sr_2RuO_4 into a $p-$wave state. Uniaxial strain along the [100] direction has been shown to strongly enhance T_c [32], and while there is no signature of $p-$wave superconductivity under strain in

single-crystals, these measurements suggest that strain is a good parameter for manipulating the superconducting state of Sr_2RuO_4.

Unlike single-crystal strain experiments, which are necessarily uniaxial or hydrostatic, thin films can be strained biaxially through substrate engineering. For example, using five different substrates, the authors of Ref. [1] showed that the γ Fermi surface sheet of Sr_2RuO_4 (and the closely related compound Ba_2RuO_4) can be driven through the Brillouin zone boundary. These films, however, were not superconducting, and for decades the growth of superconducting thin-film Sr_2RuO_4 has been a major challenge in the oxide thin film community [33]. The difficulty stems from the extreme sensitivity of Sr_2RuO_4 to even minute levels of disorder—single crystals with greater than 1 μOhm-cm residual resistivity do not superconduct [34]. With the advent of Sr_2RuO_4 films that are clean enough to show superconductivity on many different substrates [18, 35, 36], it is worth investigating whether the superconductivity is a product of film quality, substrate strain, or both, how the quasiparticle properties are modified by the substrate, and what types of defects might be limiting the quasiparticle mean free path.

2.2 Experiment

2.2.1 Film synthesis by MBE

A 100 nm thick film of Sr_2RuO_4 was grown via molecular-beam epitaxy on an $(LaAlO_3)_{0.29}$-$(SrAl_{1/2}Ta_{1/2}O_3)_{0.71}$ (LSAT) substrate with the tetragonal c-axis perpendicular to the substrate surface. This substrate imposes a 0.045% tensile strain (a dilation of the tetragonal unit cell) at low temperature. The Sr_2RuO_4 thin film was grown in a Veeco Gen10 molecular-beam epitaxy (MBE) system on a $(LaAlO_3)_{0.29}$-$(SrAl_{1/2}Ta_{1/2}O_3)_{0.71}$ (LSAT) substrate from CrysTec GmbH. The substrate used for the growth was screened to have a miscut of less than

0.05°, which is important to reduce the formation of out-of-phase boundaries [37, 38, 18].The films were grown at a substrate temperate of 810 °C as measured using an optical pyrometer operating at 1550 nm. Elemental strontium (99.99% purity) and elemental ruthenium (99.99% purity) evaporated from a low-temperature effusion cell and a Telemark electron beam evaporator, respectively, were used for growing the Sr_2RuO_4 film. The films were grown with a strontium flux of 2.6×10^{13} atoms·cm^{-2}s^{-1} and a ruthenium flux of 1.8×10^{13} atoms·cm^{-2}s^{-1} in a background of distilled ozone (∼80% O_3 + 20% O_2 made from oxygen gas with 99.994% purity.) The background oxidant pressure during growth was 3×10^{-6} Torr. At the end of the growth the strontium and ruthenium shutters were closed simultaneously, and the sample was cooled down to below 250 °C in a background pressure of distilled ozone of 1×10^{-6} Torr. The growth procedure is described in Refs. [18, 37, 39].

2.2.2 Device fabrication

Devices for measuring electrical resistivity in the *ab*-plane were fabricated using standard photolithography techniques, sputter deposition, and ion milling techniques(see Figure 4.14a). First, the Pt contact geometry was defined using photolithography. Next, 25 nm of platinum, with 5 nm titanium adhesion layer, was sputtered onto the Sr_2RuO_4 film with an AJA sputtering tool, followed by a standard lift-off processes. A second photolithography step was used to define the transport device geometry, followed by ion milling with an AJA ion mill to remove the excess Sr_2RuO_4 film. The temperature dependence of the in-plane resistivity, ρ_{xx}, reveals a high-quality device, with a RRR of 106 and a superconducting T_c of 1.05 K (RRR is defined as $R(298K)/R(T_c)$, with T_c measured at the midpoint of the transition—see Figure 4.14b.)

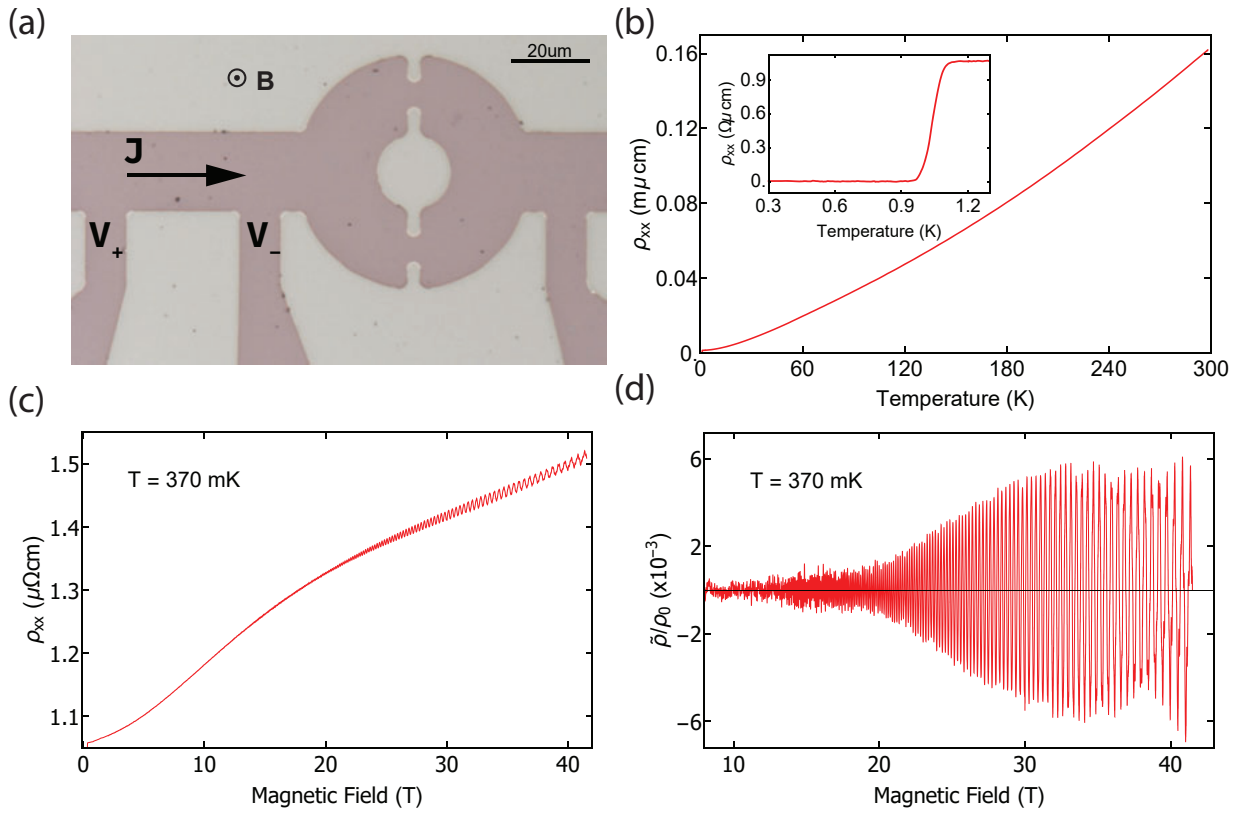

Figure 2.1: **Shubnikov-de Haas oscillations in Sr_2RuO_4 on LSAT**. (a) The Sr_2RuO_4 transport device patterned from a thin film of Sr_2RuO_4 grown on an LSAT substrate. The structure to the right of the voltage contacts was not part of this experiment. (b) Resistivity as a function temperature: The inset shows the superconducting transition with a midpoint of $T = 1.05$ K. (c) Resistivity as a function of magnetic field. (d) The normalized oscillatory component of the resistivity.

2.2.3 Quantum oscillation measurements

Quantum oscillation measurements were performed in the 41 T resistive magnet at the National High Magnetic Field Lab in Tallahassee. The magnetic field was oriented parallel to the crystallographic $c-$axis—perpendicular to the plane of the device. The temperature was controlled at fixed intervals between 370 mK and 2.2 K in a helium-3 cryostat. The sample resistance was measured in a standard 4-point contact geometry using a Stanford Research 860 lock-in amplifier, with a Stanford Research CS 580 Voltage Controlled Current Source and a Stanford Research SR560 low-noise preamplifier. The current through the

sample was $I_{\rm pp} = 150$ μA. The magnetic field was swept at a rate of 0.2 T/min, and the time constant of the lock-in amplifier was set to 1 s. The slow sweep rate ensured that the high-frequency oscillations were not washed out by the time constant of the lock-in amplifier.

Figure 1(c) presents the magnetic field dependence of the resistivity at 370 mK. The total resistivity $\rho(B)$ is composed of two parts: a non-oscillatory background $\rho_0(B)$, which we obtain by fitting a smooth polynomial to the data, and an oscillatory component $\widetilde{\rho}(B)$. The oscillatory fraction of the resistivity, $\widetilde{\rho}/\rho_0$ [40], is given by

$$\frac{\widetilde{\rho}}{\rho_0} = \left(\frac{\rho}{\rho_0} - 1\right) \tag{2.1}$$

and is plotted in Figure 4.14d. Shubnikov–de Haas oscillations are clearly visible above 15 T, with multiple frequencies visible above 35 T (see Figure 2.3a)

2.3 Analysis

We analyze the temperature and field dependence of the Shubnikov-de Haas oscillations to determine the Fermi surface area, the quasiparticle effective mass, and the quasiparticle mean free path, for all three sheets of the Fermi surface.

2.3.1 Extraction of Fermi surface area

We extract the Fermi surface area by analyzing the fraction of the resistivity data using fast Fourier transformation. Additional information about the data processing prior to Fourier transforming is given in the caption to Figure 2.2. Because all components of the oscillatory signal vary much faster than the background resistivity, the amplitudes extracted from the Fourier transforms are independent of the order of polynomial used for the background.

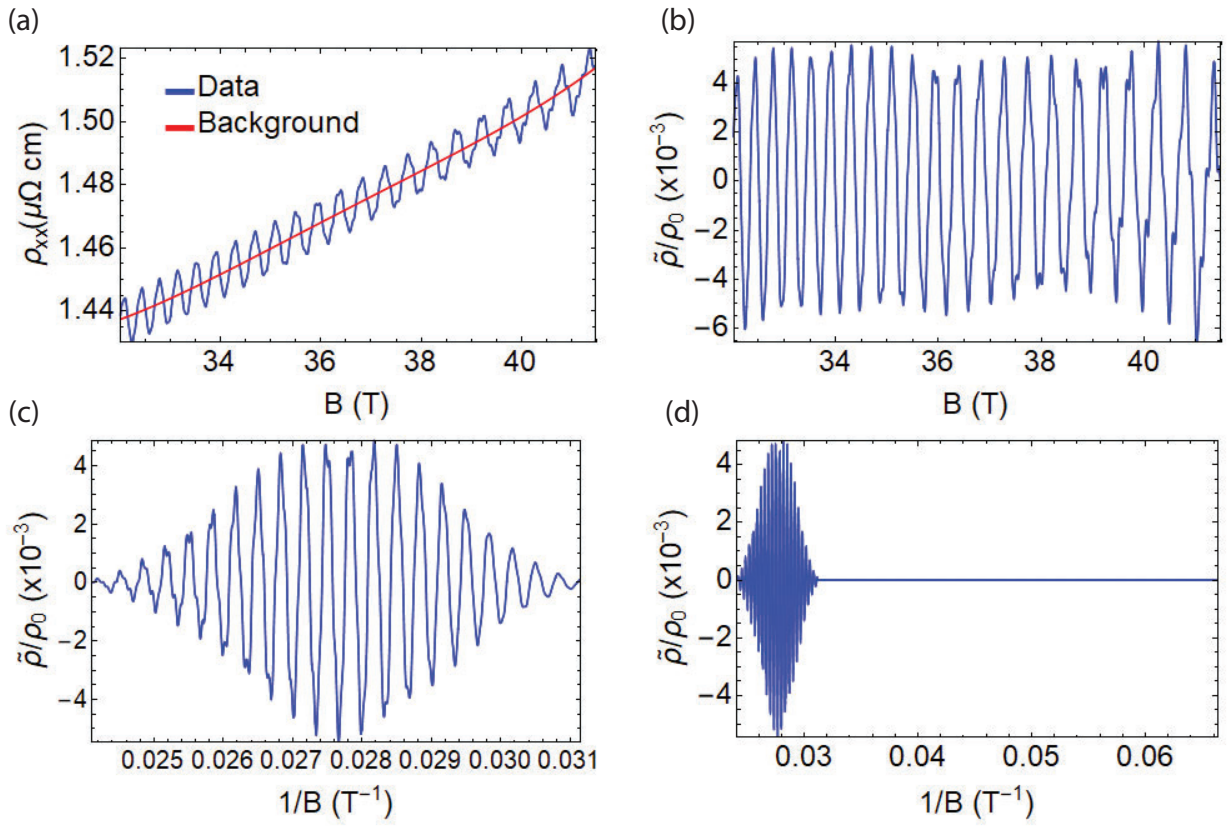

Figure 2.2: **Data processing prior to Fourier transforming.** (a) Resistivity as a function of magnetic field at 370 mK, from 32 T to 41.5 T. (b) The normalized oscillatory component of the resistivity. (c) The normalized resistivity plotted versus inverse field and multiplied by Kaiser-Bessel window with $\alpha = 1.8$. (d) The data from (c) is finally padded with zeroes before Fourier transforming, the result of which is shown in Figure 2.3b.

A Kaiser-Bessel window is used to prevent high-frequency artifacts in the FFT, and zero-padding is used for asthetic purposes to smooth the peaks. The fast Fourier transform (FFT) of $\widetilde{\rho}/\rho_0$, shown in Figure 2.3b, has clear contributions from all three known pieces of Fermi surface, labeled α, β, and γ, in accordance with previous studies [20]. Harmonics from the α pocket are visible up to the fifth order—another indication of high sample quality, as harmonic amplitude is dampened out exponentially with increasing harmonic number.

The Fermi surface area A_k is obtained from the quantum oscillation frequency F through the Onsager relation $A_k = (2\pi e/\hbar)F$. LSAT substrates apply a relatively small amount of tensile strain on the Sr_2RuO_4 films, and thus we expect the Fermi surface area of Sr_2RuO_4

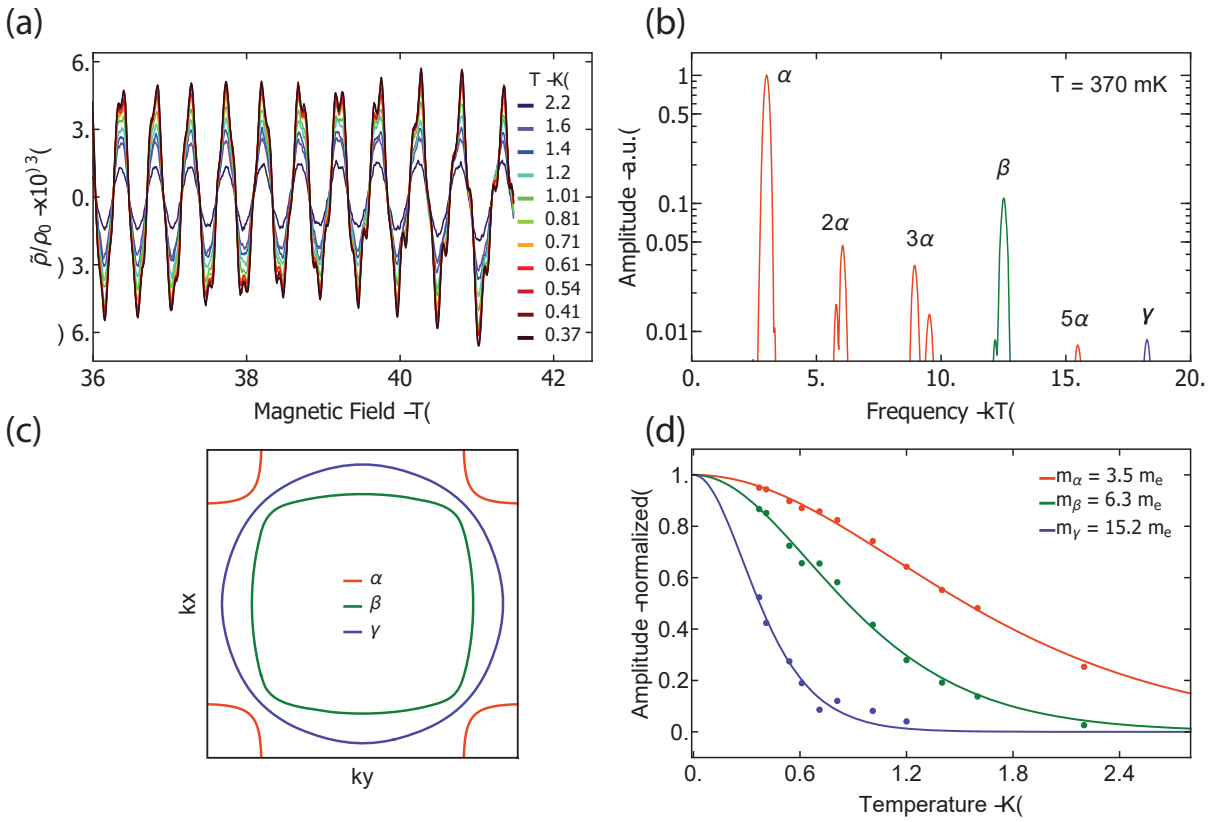

Figure 2.3: **Analysis of the Shubnikov-de Haas oscillations.** (a) Temperature dependence of the Shubnikov-de Hass oscillations in the field range from 36 to 41.5 T. Additional frequency components—beyond the 3 kT frequency of the α pocket—become clearly visible at higher field. (b) Fast Fourier transform (FFT) of the 370 mK data. The primary frequencies corresponding to the α, β, and γ Fermi surfaces (shown in (c)) are indicated, as well as the higher harmonics of the α surface. The 4α harmonic overlaps with the beta frequency, but its contribution is roughly one order of magnitude smaller than that of the β frequency itself owing to the fact that each successive harmonic is damped more strongly than the last. (d) Temperature-dependent oscillation amplitude, with a fit to Equation 2.2 for the α, β, and γ pockets. The analysis is done with data between 32 T and 41.5 T and from 370 mK to 2.2 K for α and β pockets, and between 35 T and 41.5 T and from 370 mK to 1.2 K for the γ pocket.

films to be close to what is measured in single-crystal Sr_2RuO_4. This is what we observe: within our experimental resolution, the three Fermi surfaces of Sr_2RuO_4 grown on LSAT have the same area as those reported for single crystals (a comparison is shown in Table 2.2). This is consistent with the relatively small, 0.045% A_{1g} strain imposed by LSAT to the film at low temperature.

2.3.2 Extraction of the quasiparticle effective mass $m^\star$

The quasiparticle effective mass $m^\star$ is obtained from the temperature dependence of the quantum oscillation amplitude. As the thermal energy (k_BT) becomes comparable to the cyclotron energy ($\hbar\omega_c$, where $\omega_c = \frac{eB}{m^\star}$), the oscillations are damped with the form

$$R_T = \left(2\pi^2 \frac{k_B T}{\hbar\omega_c}\right) / \sinh\left(2\pi^2 \frac{k_B T}{\hbar\omega_c}\right). \tag{2.2}$$

Figure 2(d) shows fits of the FFT amplitude to Equation 2.2. The effective mass for the α, β, and γ sheets are found to be $m^\star_\alpha = 3.5\pm0.1\ m_e$, $m^\star_\beta = 6.3\pm0.2\ m_e$, and $m^\star_\gamma = 15.2\pm1.3\ m_e$, where m_e is the bare electron mass. These masses are consistent with those found in single-crystal Sr_2RuO_4 (see Table 2.2), which is also consistent with the similarity in measured Fermi surface areas. The consistency between these Fermi surface parameters suggests that films of Sr_2RuO_4 grown on LSAT are close electronic analogs of the bulk material.

2.3.3 Extraction of the quasiparticle quantum lifetime τ_q

The remaining quantity to be determined is the quasiparticle quantum lifetime τ_q. As the inverse of the time between scattering events becomes comparable to the cyclotron frequency ω_c (or the Landau level widths becomes comparable to their separation), the oscillations are damped as

$$R_D = e^{-\frac{\pi}{\omega_c \tau_q}}. \tag{2.3}$$

The lifetime can be converted to a mean free path via $\tau_q = l_{free}/v_F$, where the Fermi velocity v_F is determined by the measured Fermi surface area and effective mass.

The quantum lifetime is more challenging to extract than the cyclotron mass and Fermi surface area for two reasons. First, the α pocket dominates the raw oscillatory signal, making it impossible to fit Equation 2.3 directly to the data for the β and γ bands. Second,

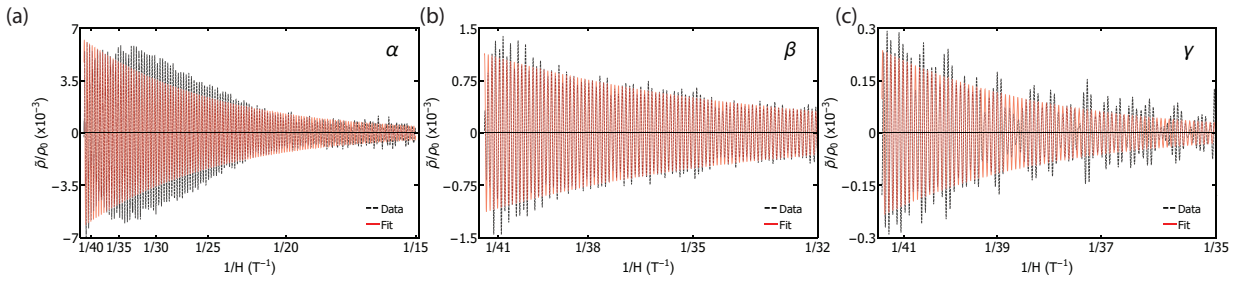

Figure 2.4: **Quantum lifetime extraction method 1.** The dashed black lines are the Fourier filtered data for the α (a), β (b), and γ (c) sheets of Fermi surface. The reds lines are fits to Equation 2.4, which yield quantum scattering times τ_q of 1.11 ps, 0.65 ps, and 0.64 ps, for the α, β, and γ sheets, respectively.

the presence of interlayer coupling leads to a beat-like structure in the data rather than a pure exponential envelope [20]. We solve the first problem by Fourier-filtering the data over frequency ranges that only include one FS component at a time. To fit the α, β, and γ sheets separately, we Fourier transform the $\frac{\widetilde{\rho}}{\rho_0}$ data taken at $T = 370$ mK, as shown in Figure 2.3b, and then band-pass filter the spectrum to include only one frequency component at a time. We then inverse-Fourier transform the spectrum to recover $\left(\frac{\widetilde{\rho}}{\rho_0}\right)_i$, where $i = \alpha, \beta$, and γ. The results are shown in Figure 2.4. Strictly speaking, one should convert from resistivity to conductivity before performing this procedure as conductivities, not resistivity, are additive. However, as $\widetilde{\rho}$ is only a tiny fraction of ρ_0, the end result is equivalent (up to an overall minus sign.) We solve the second by fitting the data over as broad a field-range as possible and by comparing the results of two different analyses to check for consistency.

The first method we use to determine the quantum lifetime is to directly fit the oscillations with Equation 2.4—these plots are shown in Figure 2.4. This has the advantage over the first technique of making use of the full data set, but as Equation 2.4 ignores the interlayer dispersion (which cannot be clearly resolved over this field range), it can become contaminated by the beat structure. With this method the quantum lifetimes we obtained for α, β, and γ sheets are 1.11 ps, 0.65 ps, and 0.64 ps, respectively.

Then, we extract the quantum lifetime with a Dingle plot. The Shubnikov-de Haas

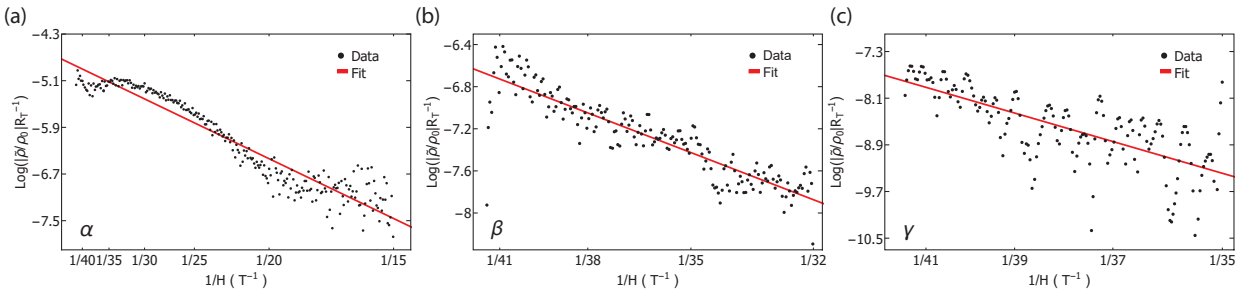

Figure 2.5: **Quantum lifetime extraction method 2.** The black points are the peaks in the absolute value of the oscillatory component for the α (a), β (b), and γ (c) sheets of Fermi surface. The reds lines are fits to a straight line, yielding quantum scattering times of 1.03 ps, 0.67 ps, and 0.77 ps, for the α, β, and γ sheets, respectively.

oscillation amplitude for a quasi-two-dimensional (2D) Fermi surface is given by

$$\frac{\widetilde{\rho}}{\rho_0} \propto R_T R_D \cos\left(\frac{2\pi F}{B}\right), \tag{2.4}$$

where R_T is given by Equation 2.2 and R_D is given by Equation 2.3. We first find the peaks of the oscillations in $|\widetilde{\rho}/\rho_0|$, divide the peak amplitude by R_T, and then plot the absolute value of this quantity on a log scale as a function of $1/B$; these plots are shown in Figure 2.5. With $m^\star$ determined from the temperature dependence, the quantum lifetimes can be immediately obtained from the slope of this plot, and we find lifetimes of 1.03 ps, 0.67 ps and 0.77 ps, for the α, β, and γ sheets, respectively.

The two methods give similar estimates for τ_q. We take the average of the two results and estimate the uncertainty as half of the difference between them. The quantum lifetimes of the α, β, and γ sheets are 1.07±0.04 ps, 0.66±0.01 ps, and 0.71±0.07 ps, respectively. As the γ pocket was only observed above 35 T, there is certainly a larger systematic uncertainty associated with this lifetime than we are able to account for with this method. Converting the three lifetimes to mean free paths yields 108 nm, 75 nm, and 40 nm, for the α, β, and γ Fermi surfaces, respectively. These values can be compared with those obtained from single crystals: the authors of Ref. [4] reported Dingle temperatures that convert to mean free paths of 210 nm, 176 nm, and 130 nm, for the α, β, and γ Fermi surfaces, respectively. While the single-crystal values are somewhat longer than those from our film, the progression

of the longest mean free path on the α pocket to the shortest on the γ pocket is consistent (note that subsequent generations of single-crystal Sr_2RuO_4 have even longer mean free paths [20].)

2.3.4 Extraction of the transport lifetime τ_t

The transport lifetime τ_t—a quantity related to, but distinct from, the quantum lifetime—can be extracted from the absolute value of the resistivity ρ_{xx} now that the Fermi surface areas and effective masses are known. We start with a tight-binding model of Sr_2RuO_4's band structure, adjust the tight-binding parameters so that the Fermi surface areas and effective masses match the values measured for our sample, and then solve the Boltzmann transport equation using Chambers' solution [41].

The tight-binding model

We use a standard three-orbital tight-binding model to describe the band structure of Sr_2RuO_4 [1]. The energy bands are the eigenvalues of the Hamiltonian matrix

$$\boldsymbol{H} = \begin{pmatrix} \epsilon_{xy} & 0 & 0 \\ 0 & \epsilon_{xz} & V \\ 0 & V & \epsilon_{yz} \end{pmatrix}, \tag{2.5}$$

where $\epsilon_{xy} = -\mu_1 - 2t_1(\cos(k_x a) + \cos(k_y a)) - 4t_4 \cos(k_x a)\cos(k_y a)$ is the tight binding model of the ruthenium d_{xy} orbitals, $\epsilon_{\{x,y\}z} = -\mu_2 - 2t_2 cos(k_{\{x,y\}}a) - 2t_3 \cos(k_{\{y,x\}}a)$ are the tight binding models of the ruthenium d_{xz} and d_{yz} orbitals, and $V = 4t_5 \sin(k_x a)\sin(k y_a)$ is the hybridization matrix element between the d_{xz} and d_{yz} orbitals.

We start with tight binding parameters for bulk Sr_2RuO_4, given in [1], and adjust μ_1/t_1 and μ_2/t_2 so that the Fermi surface areas produced by the tight-binding model agree with

	F_α (T)	F_β (T)	F_γ (T)	m_α (m_e)	m_β (m_e)	m_γ (m_e)
ARPES fit	2959	12498	17886	2.0	5.7	11.6
Scaled	2988	12357	18268	3.6	6.4	15.1
This experiment	3079	12510	18259	3.5	6.3	15.2

Table 2.1: Comparison of Fermi surface parameters as given by the tight-binding fit in [1], the values obtained from scaling that tight binding model, and the experimental values from this work.

the areas we measure from the quantum oscillations. We further adjust the bandwidth of each band that results from diagonalizing Equation 2.5 so that the effective masses given by the tight binding model also agree with the experimental results. The effective masses for each of the three Fermi surfaces given by Equation 2.5 are calculated numerically via

$$m_i = \frac{\hbar^2}{2\pi}\left(\frac{\partial A_k}{\partial \epsilon_i}\right), \tag{2.6}$$

where A_k is the Fermi surface area in momentum space [40]. The renormalizations of the bandwidths required to obtain agreement between the tight binding and experimental masses are 0.60, 0.78, and 0.65 for the α, β and γ sheets, respectively. While these scaling factors change the bandwidths from those experimentally determined by ARPES, only the slopes of the bands immediately at the Fermi energy are relevant for quantum oscillations and the electrical resistivity. These renormalizations may account for interaction effects that are not resolvable by ARPES, for example.

Table 2.1 compares the quantum oscillation frequencies and effective masses as given by the tight binding fit of the ARPES spectra on bulk Sr_2RuO_4 from [1], the values obtained by scaling that band structure, and the experimental values we obtain from the quantum oscillations.

Calculation using the Chambers Formula

The Boltzmann transport equation can be solved in the semiclassical limit, and within the relaxation-time approximation, for any component of the conductivity tensor. The approach most suitable for calculating the conductivity for arbitrary band structures was developed by Chambers [41], with the conductivity tensor given as

$$\sigma_{ij} = \frac{e^2}{4\pi^3} \int d^3\boldsymbol{k} \left(-\frac{df_0}{d\epsilon} \right) v_i(\boldsymbol{k})\, v_j(\boldsymbol{k})\, \tau_t, \tag{2.7}$$

where $\int d^3\boldsymbol{k}$ is an integral over the entire Brillouin zone, $\left(-\frac{df_0}{d\epsilon}\right)$ is the derivative with respect to energy of the equilibrium Fermi distribution function, $v_i(\boldsymbol{k})$ is the i^{th} component of the quasiparticle velocity at momentum point $\boldsymbol{k}$, and τ_t is the quasiparticle transport lifetime. The velocity is calculated from a tight binding model of the bandstructure using $\boldsymbol{v} = \frac{1}{\hbar}\vec{\nabla}_{\boldsymbol{k}}\epsilon(\boldsymbol{k})$.

In the limit that the temperature is much smaller than any of the hopping parameters in $\epsilon(\boldsymbol{k})$, the factor $\left(-\frac{df_0}{d\epsilon}\right)$ can be accurately approximated as a delta function at the Fermi energy. This delta function transforms the integral over the Brillouin zone into an integral over the Fermi surface and introduces a factor of $1/|\vec{\nabla}_{\boldsymbol{k}}\epsilon(\boldsymbol{k})|$, which is the density of states. Equation 2.7 is solved numerically by discretizing the Fermi surface and summing $v_i(\boldsymbol{k})\, v_j(\boldsymbol{k})$ for each point, weighted by the local density of states. We use it to calculate σ_{xx} and σ_{xy}, and use these quantities to calculate $\rho_{xx} = \frac{\sigma_{xx}}{\sigma_{xx}\sigma_{yy} - \sigma_{xy}\sigma_{yx}}$.

As there are three transport lifetimes—one for each Fermi surface—but only one value of ρ_{xx} to fit, we make the simplifying assumption that the ratio of τ_t to τ_q is the same for all sheets of Fermi surface. We adjust this ratio until the calculated resistivity matches the measured residual resistivity, $\rho_{\text{xx}}(T_{\text{c}})$=1 $\mu\Omega$·cm. We find that $\tau_t/\tau_q = 1.3 \pm 0.1$. This translates to transport mean free paths of 140 nm, 97 nm, and 52 nm, for the α, β, and γ Fermi surfaces, respectively. Because τ_q is a lower bound on τ_t, the ratio τ_t/τ_q must be at least 1. If we relax the constraint that τ_t/τ_q is the same for all Fermi surfaces, then at most

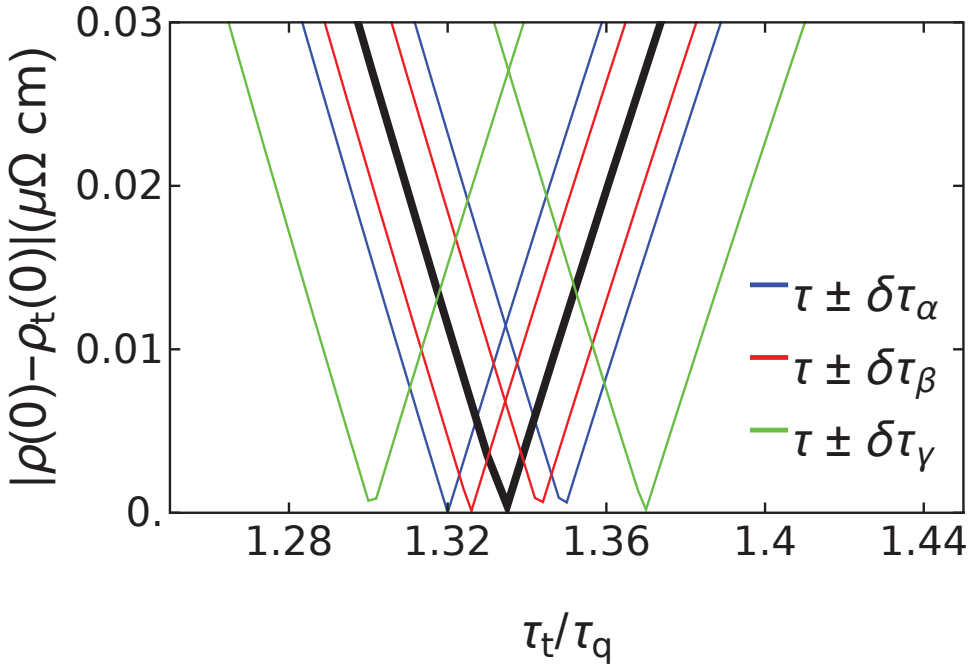

Figure 2.6: **Uncertainty estimation for** τ_t/τ_q The absolute value of the difference between the calculated resistivity and the measured residual resistivity as a function of τ_t/τ_q. The blue, red, and green lines are used to determine the uncertainty from the quantum lifetime of the α, β, and γ pockets, respectively. The black line uses the measured quantum lifetimes shown in Table 2.2.

two Fermi surfaces could have $\tau_t/\tau_q = 1$ and the third would have τ_t/τ_q greater than 1.3 (the exact value depends on which Fermi surface is chosen). Without further microscopic justification for why τ_t/τ_q might be different on different Fermi surfaces, the assumption that this ratio is the same for all Fermi surfaces is the simplest one that we can make.

Method for obtaining the value of τ_t/τ_q and its uncertainty

We start by evaluating the uncertainty in τ_t/τ_q that comes from the uncertainties in τ_q. We use the tight-binding parameters that best match the Fermi surface areas and cyclotron masses we measure (see section 2.3.4). With the adjusted tight-binding parameters and with the measured quantum lifetimes for the three pockets, we solve the Boltzmann equation numerically and obtain the resistivity at zero magnetic field. We then have only one parameter,

Fermi surface	Frequency (T)	Effective mass (m_e)	τ_q (ps) (quantum lifetime)	τ_t (ps) (transport lifetime)
α (film)	3079 ± 99	3.5 ± 0.1	1.07 ± 0.04	1.39 ± 0.12
α (single crystal)	3010 ± 80	3.4 ± 0.1	2.0	
β (film)	12510 ± 108	6.3 ± 0.2	0.66 ± 0.01	0.86 ± 0.07
β (single crystal)	12730 ± 150	6.8 ± 0.2	1.7	
γ (film)	18259 ± 195	15.2 ± 1.3	0.71 ± 0.07	0.92 ± 0.12
γ (single crystal)	18570 ± 70	14.0 ± 2.0	2.4	

Table 2.2: A comparison of the Fermi surface parameters extracted for a Sr_2RuO_4 film grown on LSAT and those obtained from de Haas–van Alphen measurements on single-crystal Sr_2RuO_4 [2, 3] (τ_q for single-crystals comes from Ref. [4].) The transport lifetime τ_t is calculated from the value of $\rho_{xx}(T_c)$ assuming that the ratio τ_t/τ_q is the same for all sheets of Fermi surface. The quantum lifetime is extracted from the data taken at $T = 370$ mK, which has oscillations from all three Fermi surfaces over the broadest field range. The details of the estimation of uncertainties are listed in [1].

τ_t/τ_q, to determine. For fixed values of the three τ_q's, we vary the ratio of τ_t/τ_q to minimize the difference between the calculated resistivity and the measured resistivity. We repeat this procedure at the upper and lower bounds of τ_q for each of the three pockets. This determines the uncertainty in τ_t/τ_q from the uncertainties in the quantum lifetimes of α, β, and γ to be ± 0.02, ± 0.01, and ± 0.04, respectively. Added in quadrature, this gives a total uncertainty in τ_t/τ_q of ± 0.046.

Next there is uncertainty in the experimental value of the residual resistivity. This is due to uncertainty in the contact geometry, the sample dimensions, as well as uncertainties in the measurement procedure.

To reduce the uncertainty of the absolute resistivity (and thus transport mean free path) from contact geometry, we perform finite element simulations of the contact geometry of

[1] The frequencies and their uncertainties for the three pockets in thin film Sr_2RuO_4 are obtained from the Fourier transform shown in Fig. 2b. The frequency for α is taken to be the average of the two peaks at 3α, divided by three, and the uncertainty is taken to be half of their difference, divided by three. This avoids interference effects due to multiple closely-spaced frequencies that arise from inter-layer coupling (such interference is likely shifting the first harmonic peak down in frequency). The frequency and uncertainty in frequency of β and γ pockets are obtained by fitting a lorentzian function to the data near the corresponding FFT peaks. The frequencies and their uncertainties for the three pockets in single crystal Sr_2RuO_4 are taken to be the average and half of their difference between the values reported in two de Haas-van Alphen studies [2, 4]. The same procedure is used to obtain the effective masses and their uncertainties.

our device, shown in Figure 4.14a. Typically, when the width of the voltage contacts is comparable to the distance between the contacts, there is large uncertainty in the conversion from resistance to resistivity. With the help of a finite element simulation, we can determine the correct geometric factor for our sample and thus reduce the uncertainty substantially.

The model we use in the simulation is shown in Figure 2.7. We fix the current density flowing into and out of the sample, normal to the top edge and the bottom edge, and solve for the stationary solution. We obtain the measured resistance using $R = (V_+ - V_-)/(J_0 * \mathrm{W_{sample}} * \mathrm{t})$, where V_+ and V_- are the average electric potential along the edges labeled V_+ and V_- in Figure 2.7a, J_0 is the current density, $\mathrm{W_{sample}}$ is the sample width, and t is the film thickness. As the resistivity of the material, ρ, is fixed in the model, we can also calculate a value for the resistance using $R = \rho * l/\mathrm{A}$, where l is some effective sample length, and $\mathrm{A} = \mathrm{t} * \mathrm{W_{sample}}$ is the cross section area. By varying the effective sample length and comparing the calculated resistance with the resistance measured via V_+ and V_-, we can determine the correct effective sample length.

We set L to 30 μm, $\mathrm{W_{sample}}$ to 20 μm, and T to be 100 nm, which are the dimensions of our device. Figure 2.7b shows how the measured (V/I) and calculated resistances change with contact width W. At our experimental contact width of W = 10 μm, we find that an effective sample length l of $\mathrm{L} + 0.9 * \mathrm{W}$ agrees with the measured resistance to better than 1%.

The uncertainties in the lateral dimensions of the sample come from the resolution of the photolithography process and are $\pm$0.5 um. The thickness of the film is known precisely from the STEM images; the presence of step edges introduces an uncertainty of $\pm$1 nm in the thickness. The total uncertainty in the residual resistivity from sample dimensions is determined to be $\pm$3.7 % ($\pm$ 0.037 $\mu\Omega$.cm). The uncertainty in the output of the current source is $\pm$0.1% and the uncertainty in the lock-in measurement is $\pm$1%. Assuming that all the measurement uncertainties are uncorrelated, we find the total uncertainty in the residual

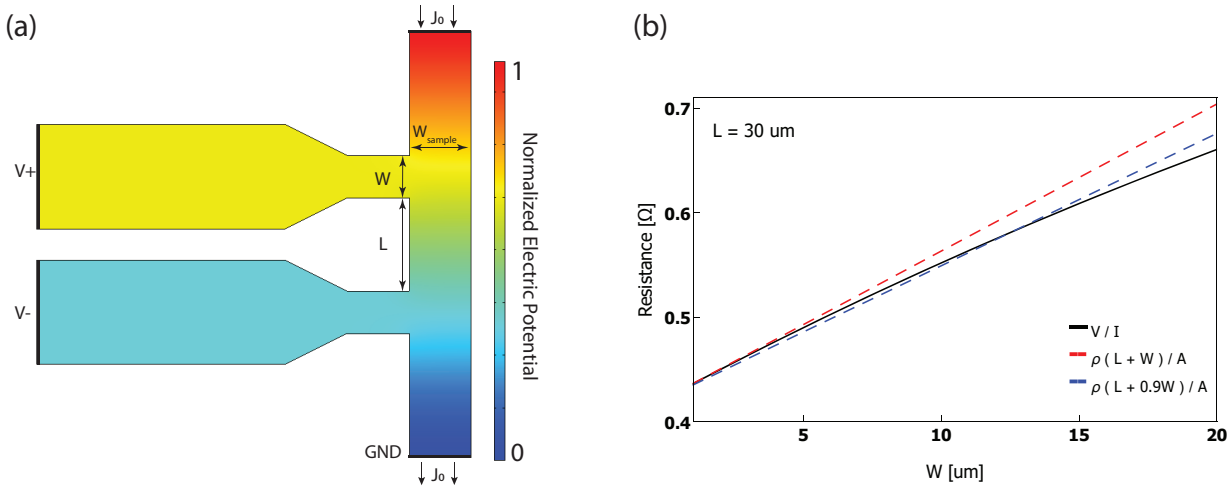

Figure 2.7: **Finite element simulation on the effect of the width of voltage contact.** (a) The model used in the finite element simulation. W_{sample} is set to 20 μm and L is set to 30 μm, which are the dimensions of the device. The color scale represents the normalized electric potential. (b) Resistance versus voltage pad width W, with all other dimensions and the resistivity of the material fixed. The black line represents the measured resistance and the red and blue dashed line represents the calculated resistance with l set to L + W and L + 0.9W, respectively.

resistivity to be ± 3.8 %, or $\pm 0.038 \mu\Omega$.cm. Using the slope of τ_t/τ_q as a function of the residual resistivity (Figure 2.6), this produces an uncertainty in τ_t/τ_q of ± 0.04.

Finally, combining the uncertainties from τ_q with the uncertainty from the residual resistivity, the final value of τ_t/τ_q is 1.34 ± 0.06. We round this value to 1.3 ± 0.1.

2.4 Discussion

The transport lifetimes we measure here approach those of clean-limit, single-crystal Sr_2RuO_4 [34]. They are also comparable to what was reported in some of the earliest quantum oscillation measurements of single-crystal Sr_2RuO_4 [42]. To put our measured mean free path of over 100 nm in context with other oxide thin film superconductors, a useful comparison can be made with $Pr_{2-x}Ce_xCuO_{4\pm\delta}$, whose crystal structure is very similar to that of Sr_2RuO_4. High-field quantum oscillation studies on $Pr_{2-x}Ce_xCuO_{4\pm\delta}$ measured the mean free path to

be only 6 nm [43], highlighting the extremely high quality of our Sr_2RuO_4 films.

Long mean free paths are crucial for observing the intrinsic T_c of Sr_2RuO_4: the authors of Ref. [34] found that 90 nm is the critical transport mean free path for superconductivity in Sr_2RuO_4—any shorter and the material does not superconduct; any longer and the T_c rises rapidly to ≈ 1.5 K. We find mean free paths longer than this length on the α and β bands, which are thought to dominate the superconductivity in Sr_2RuO_4 [44], and which is consistent with a T_c of 1.05 K for single-crystal Sr_2RuO_4 [34].

The difference between the measured quantum and transport lifetimes may offer a clue as to what is the dominate scattering mechanism in these films. The quantum lifetime is the average time a quasiparticle spends in a momentum eigenstate before scattering. The transport lifetime is the average time between scattering events that relax the quasiparticle momentum distribution function. When scattering is isotropic, as it is for point-scatterers, $\tau_q = \tau_t$. For extended defects, the transport lifetime is generally longer than its quantum counterpart: extended defects contribute more forward-scattering events that do not alter the momentum distribution function of the quasiparticles but *do* decohere the quasiparticle wavefunctions. This was studied systematically in AlGaN/GaN heterostructures, where small-angle scattering from dislocations reduces the quantum lifetime by up to a factor of 20 below the transport lifetime [45]. While a ratio of 1.3 ± 0.1 is not nearly as compelling as a ratio of 20, we were nevertheless motivated to study the microscopic nature of the defects in this film.

To investigate the character and density of extended defects in our samples, we performed cross-sectional STEM on lamellas cut from the contact region of the device shown in Figure 4.14a. Figure 2.8 shows where the lamellas were cut for the STEM imaging. Figure 2.9a and b show representative cross sections cut parallel and perpendicular to the direction of the applied current, respectively (more images are shown in Figure 2.10.) Cross-sectional STEM specimens were prepared using the standard focused ion beam (FIB) lift-out process

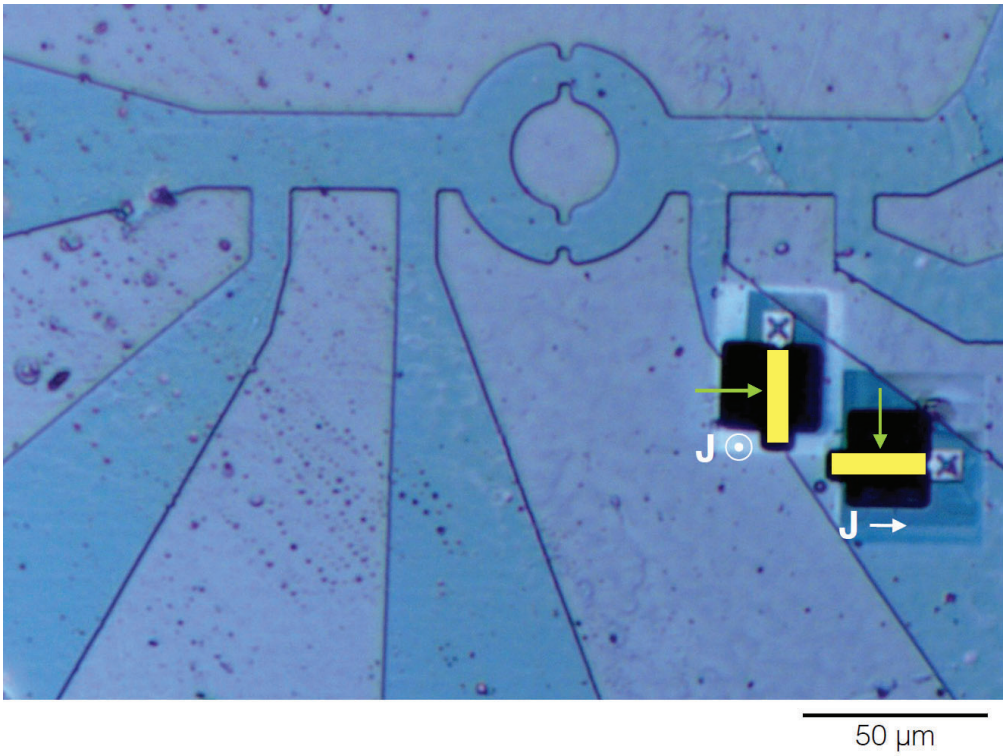

Figure 2.8: **Device and STEM specimen locations.** Optical micrograph showing the location and orientation of the extracted cross sections for STEM experiments. The top-view orientation of the lamella cut from each location is indicated by the thick yellow line. The green arrows indicate the projection axes of STEM imaging for each case.

on Thermo Scientific Helios G4 UX FIB. Medium-angle annular dark-field scanning transmission electron microscopy (MAADF-STEM) images were acquired on an aberration-corrected FEI Titan Themis operating at 300 keV with a probe convergence semi-angle of 30 mrad and inner and outer collection angles of 46 and 230 mrad, respectively.

In the medium angle annular dark field (MAADF) collection geometry used here (40 mrad inner collection angle), extended defects—predominantly out-of-phase boundaries—are visible as regions of lighter contrast (yellow and white arrows). Some defects terminate near the interface (white arrows), while others extend through significant depth of the film (yellow arrows). These extended defects have a density of approximately 1 every 100 to 200 nm. This density is consistent with the quantum mean free path we extract from the quantum oscillations. The longer transport mean free path, as compared to the quantum

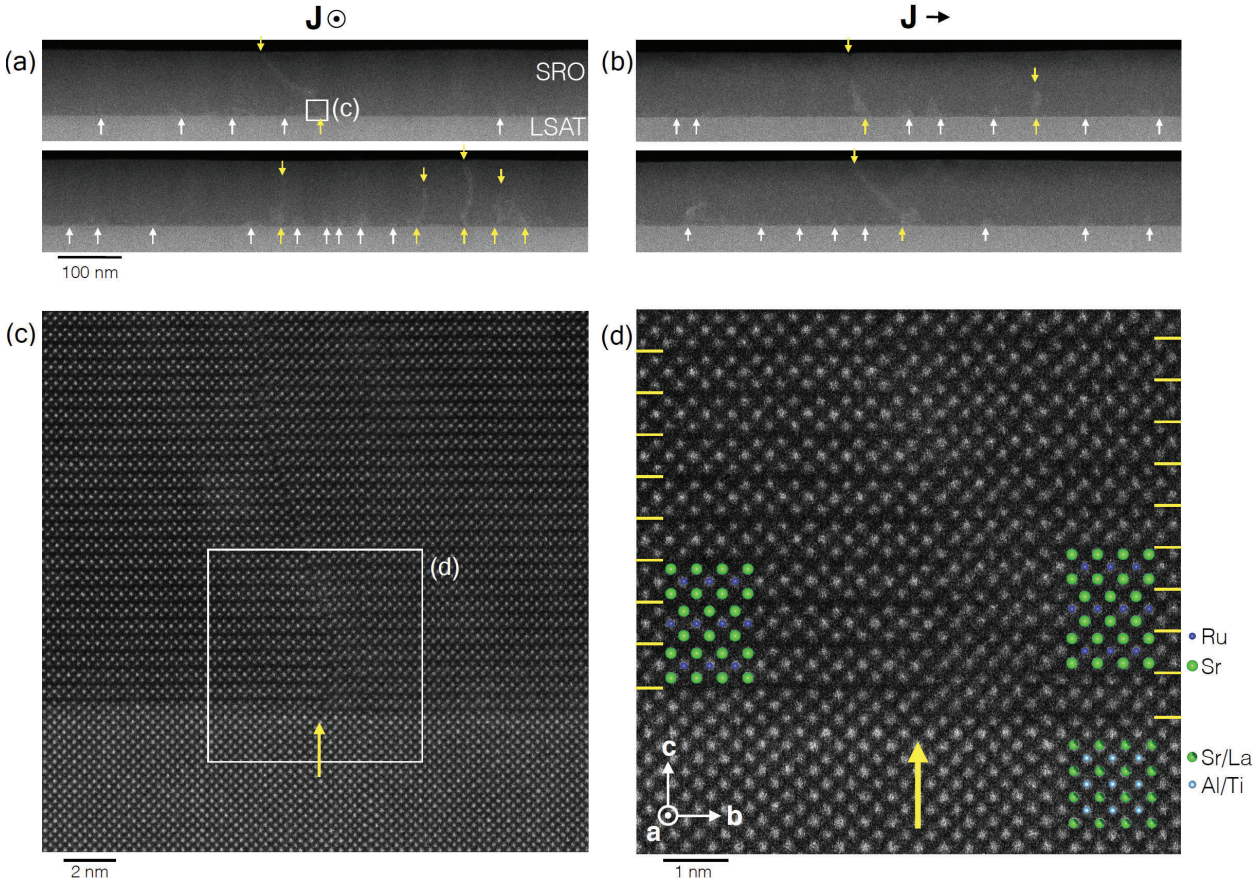

Figure 2.9: **Defect characterization by cross-sectional STEM.** Atomic-resolution medium angle annular dark field scanning transmission electron microscopy (MAADF-STEM) images for cross sections perpendicular (a) and parallel (b) to the current direction in Figure 4.14a. Extended lattice defects, such as out-of-phase boundaries, are indicated with arrows. Many defects terminate near the interface of the film (white arrows), while some are observed to extend through more than half the film thickness (yellow arrows). (c) Nearly all out-of-phase boundaries can be traced to nucleate at step edges (yellow arrow) in the LSAT substrate surface, as seen in this atomic-resolution image of a defect nucleation from the region marked by the white box in (a). (d) High-magnification inset of the area marked by the white box in (c) shows how Sr_2RuO_4 layers growing near a single unit cell LSAT step edge meet at a vertical defect due to the vertical offset of SrO planes on either side of the step edge.

mean free path, is consistent with the predominantly small-angle scattering that results from the large spatial extent of these defects [45]. Atomic-resolution MAADF-STEM images at the interface shown (Figure 2.9c and d) show that step-edges in the LSAT substrate are predominant nucleation sites for these defects. A single unit cell step edge in the LSAT substrate surface appears at the base of a vertically-running fault in the film, visible as

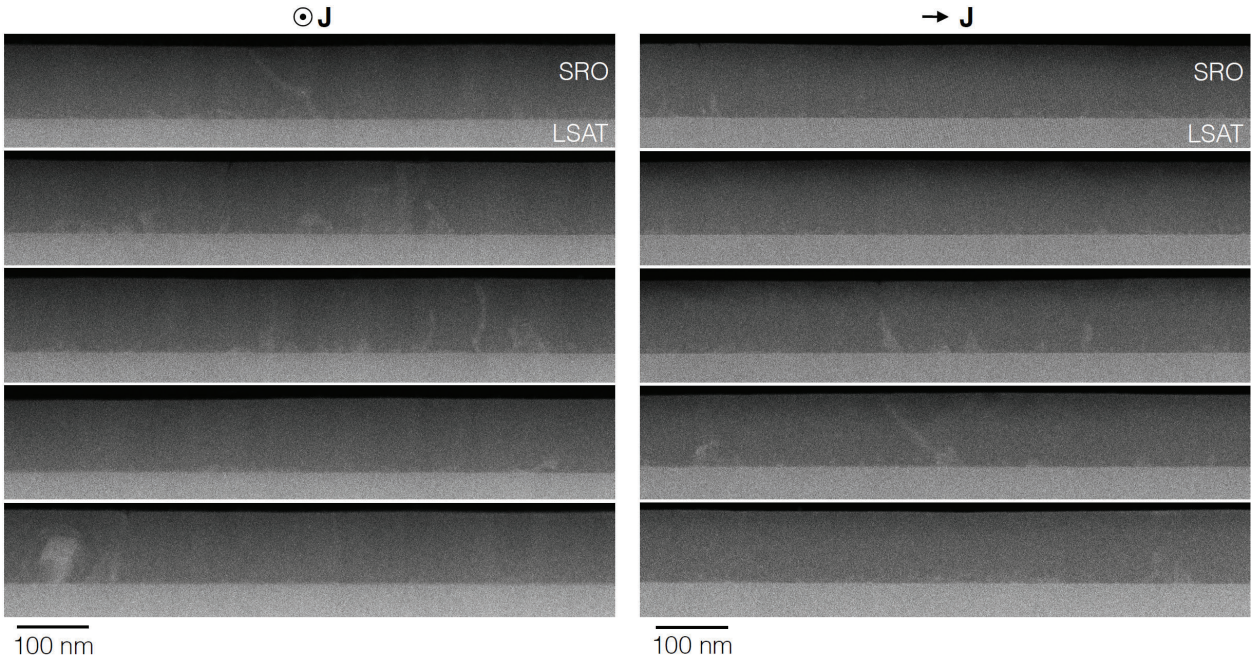

Figure 2.10: **Cross-sectional STEM.** The contribution of small scattering angles in large field-of-view MAADF STEM images of the Sr_2RuO_4 film in each pseudocubic projection highlight the extended lattice defects with brighter contrast. Nearly all of the extended defects appear to nucleate at the interface with the substrate, suggesting that step edges or other aspects of the LSAT surface may play a limiting role in the growth of clean Sr_2RuO_4 films for these devices. Some defect structures extending throughout the entire film all the way to the surface are observed in each projection, with a distribution density on the order one per μm or fewer. No significant difference in defect density is observed between the two projections.

offset SrO rock salt layers on either side (marked by yellow lines). This suggests that future improvements in Sr_2RuO_4 film quality should focus on reducing the density of step edges through substrate surface preparation.

The extreme sensitivity of T_c to disorder in Sr_2RuO_4 raises the question of whether the relatively high T_c observed in thin films can be attributed to film cleanliness or whether the presence of the substrate significantly modifies the electronic structure and thus T_c. The Fermi surface areas and quasiparticle effective masses we measure for Sr_2RuO_4 grown on LSAT are the same as those found in single-crystal Sr_2RuO_4 to within our measurement uncertainty. This suggests that modifications to the electronic structure, such as an enhanced density of states (proportional to $m^\star$ in two-dimensional materials) due to substrate strain

pushing the Fermi surface toward the van Hove point, are not responsible for the relatively high T_c (1.05 K) observed in these films grown on the commercial perovskite substrate that is best lattice matched to Sr_2RuO_4 [46]. It will be interesting to see how the electronic structure, mean free path, and perhaps even superconducting order parameter symmetry are modified when commensurately strained Sr_2RuO_4 films are grown on other substrates, where the T_c can be as high as 1.8 K and strain is undoubtedly playing a larger role [18].

CHAPTER 3

FERMI SURFACE TRANSFORMATION AT THE PSEUDOGAP CRITICAL POINT OF A CUPRATE SUPERCONDUCTOR

This chapter is adapted from a Nature Physics paper, Fermi surface transformation at the pseudogap critical point of a cuprate superconductor, with Gaël Grissonnanche, Anaëlle Legros, Simon Verret, Francis Laliberté, Clément Collignon, Amirreza Ataei, Maxime Dion, Jianshi Zhou, David Graf, M. J. Lawler, Paul A. Goddard, Louis Taillefer, and B. J. Ramshaw [47] and a Nature paper, Linear-in temperature resistivity from an isotropic Planckian scattering rate, with Gaël Grissonnanche, Anaëlle Legros, Simon Verret, Francis Laliberté, Clément Collignon, Jianshi Zhou, David Graf, Paul A. Goddard, Louis Taillefer and B. J. Ramshaw [48].

The nature of the pseudogap phase remains a major puzzle in our understanding of cuprate high-temperature superconductivity. Whether or not this metallic phase is defined by any of the reported broken symmetries, the topology of its Fermi surface remains a fundamental open question. Here we use angle-dependent magnetoresistance (ADMR) to measure the Fermi surface of the cuprate $La_{1.6-x}Nd_{0.4}Sr_xCuO_4$. Outside of the pseudogap phase we can fit the ADMR data and extract a Fermi surface geometry that is in excellent agreement with angle-resolved photoemission data. Within the pseudogap regime the ADMR is qualitatively different, revealing a transformation of the Fermi surface. We can rule out changes in the quasiparticle lifetime as the sole cause of this transformation. We find that our data are most consistent with a pseudogap Fermi surface that consists of small, nodal hole pockets, thereby accounting for the drop in carrier density across the pseudogap transition found in several cuprates.

3.1 Introduction

A long-standing mystery of the high-T_c cuprate superconductors is the 'pseudogap phase' [49]—a correlated electronic state whose key characteristic is a loss of coherent quasiparticles below an onset temperature $T^\star$ and below a critical doping $p^\star$. This loss of quasiparticles is reminiscent of the superconducting gap that opens at the transition temperature T_c (hence the name 'pseudogap'), suggesting that the pseudogap phase and superconductivity are related. Characterizing what remains of the coherent Fermi surface (FS) inside the pseudogap phase is, therefore, a critical step toward understanding how this peculiar metallic state gives rise to, or is compatible with, high-temperature superconductivity.

Heavily overdoped cuprates are good metals with a well-defined FS. $Tl_2Ba_2CuO_{6+\delta}$ (Tl2201) has been measured extensively in this doping regime and three independent experiments agree on the geometry of the FS: angle-dependent magnetoresistance (ADMR) [50],

angle-resolved photoemission spectroscopy (ARPES) [51], and quantum oscillations [52]. Other cuprates, such as $La_{2-x}Sr_xCuO_4$ and $Bi_2Sr_2CaCu_2O_{8+\delta}$, show similar agreement between the measured FS and band structure calculations for $p > p^\star$[53]. As the doping is lowered toward $p^\star$ the Fermi surface measured by ARPES remains well-defined but the electrical resistivity becomes progressively more anomalous, becoming perfectly linear-in-temperature at $p^\star$ [54, 9]. Whether a T-linear scattering rate alone can account for this anomalous resistivity has been the subject of much debate: we have addressed this topic in a recent study [48].

Cuprates enter the pseudogap phase below $p^\star$. While this phase is also metallic, its FS—in the limit $T \to 0$ and in the absence of superconductivity—remains unknown. ARPES measurements performed above T_c and below $T^\star$ find discontinuous segments known as "Fermi arcs" [53], which defy the conventional definition of a closed FS. Quantum oscillations, on the other hand, reveal a small, closed, electron-like FS ("electron pocket") [55]. This pocket, however, appears only in the presence of charge density wave (CDW) order [56], and CDW order is not always observed over the same range of dopings as the pseudogap phase itself. For example, while CDW order extends up to $p^\star$ in $HgBa_2CuO_{4+x}$ [57], it terminates before $p^\star$ at $p \approx 0.16$ in $YBa_2Cu_3O_{6+x}$ [58] and at $p \approx 0.18$ in $La_{1.6-x}Nd_{0.4}Sr_xCuO_4$ [11] (the compound we study here.) Spin density wave (SDW) order has also been found below $p^\star$ in several cuprates [59, 8, 60]. Recent neutron diffraction measurements have even found indications of SDW order at $p = 0.24$, in zero magnetic field and at $T = 13$ K [8] (see Figure 3.2a). While SDW order is known to reconstruct part of the Fermi surface at much lower doping [61], our sample at $p = 0.24$ shows perfectly linear resistivity down to 2 K at $B = 35$ T, without an upturn at $T = 13$ K that would be characteristic of SDW order [62] (see Figure 3.1). This suggests that either there are differences between samples grown by different groups or that a magnetic field suppresses the SDW order at $p = 0.24$.

A crucial question therefore remains: what is the Fermi surface of cuprates immediately

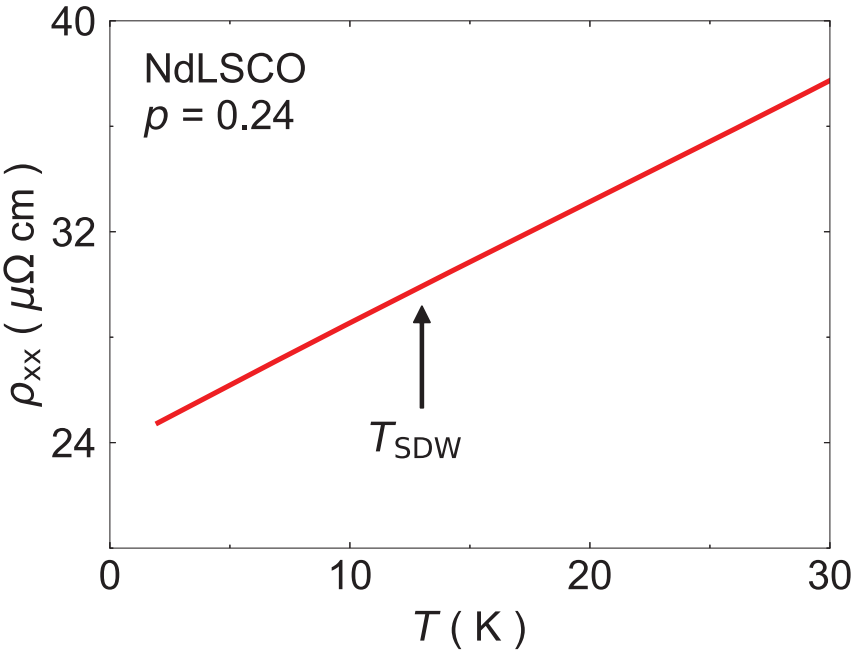

Figure 3.1: In-plane resistivity data at $B = 35$ T as a function of temperature. The resistivity ρ_{xx} (red line) is perfectly linear down to the lowest temperature without any sign of an upturn or even a change in slope at $T_{SDW} = 13 \pm 1$ K (black arrow) reported by [8] at $B = 0$ T. This suggests that either the SDW is not present in our samples or that the SDW vanishes in a magnetic field and thus does interfere with our measurements performed at $B = 45$ T.

below $p^\star$ in the absence of superconductivity or CDW order? There are two possibilities: i) the FS is the same above and below $p^\star$, but the quasiparticles become incoherent below $p^\star$ due to scattering or other correlation effects; ii) the FS below $p^\star$ is different from the FS above $p^\star$. Demonstration of the latter scenario would imply either that translational symmetry is broken (on some appropriate length scale) in the pseudogap phase or that it is a phase with topological order [63].

3.2 Angle-dependent magnetoresistance (ADMR) experiment

To determine whether the FS is transformed across $p^\star$ we measure variations in the c-axis resistivity ρ_{zz} of Nd-LSCO at $p = 0.21$ and $p = 0.24$ as a function of the polar (θ) and

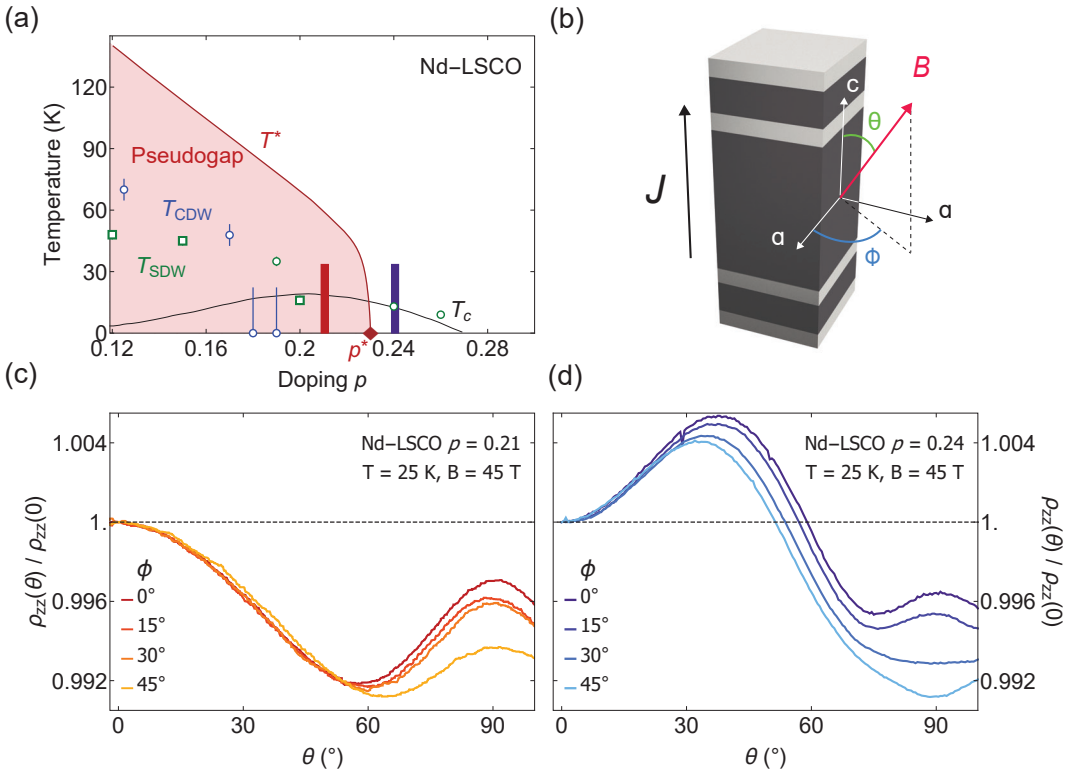

Figure 3.2: (**a**) Temperature-doping phase diagram of the hole-doped cuprate Nd-LSCO in zero magnetic field. The pseudogap phase is highlighted in red (the onset temperature $T^\star$ is taken from resistivity [9, 10] and ARPES [5] measurements). The critical doping where the pseudogap phase ends is $p^\star = 0.23$ (red diamond [10]). The superconducting dome is marked by a solid black line and can be entirely suppressed with $\boldsymbol{B} \parallel c \geq 20$ T. The onset of short-range charge density wave order, as detected by resonant X-ray scattering [11], is indicated by the blue circles. The onset of spin density wave order, as detected by neutron scattering, is indicated with green circles ([8]) and green squares ([12]). The red and blue bars correspond to the dopings and temperature ranges measured in this study. (**b**) Geometry of the ADMR measurements. The sample is represented in gray with silver contacts. The black arrow identifies the direction of the electric current, $\boldsymbol{J}$, along the c-axis. The angles ϕ and θ indicate the direction of the magnetic field $\boldsymbol{B}$ with respect to the crystallographic a- and c-axes. (**c**) The angle-dependent c-axis resistivity $\rho_{zz}(\theta)$ of Nd-LSCO at $p = 0.21$ ($< p^*$). All data are taken at $T = 25$ K and $B = 45$ T as a function of θ for $\phi = 0°, 15°, 30°$, and $45°$, and normalized by the $\theta = 0$ value $\rho_{zz}(0)$. (**d**) Data taken under the same conditions as panel (c), but for Nd-LSCO at $p = 0.24$ ($> p^*$). Note that certain features change significantly across $p^\star$, including the peak near $\theta = 40°$ and the ϕ-dependence near $\theta = 90°$.

azimuthal (ϕ) angles between the sample and an external magnetic field $\boldsymbol{B}$ (see Figure 3.2b, c, d)—a technique known as angle-dependent magnetoresistance (ADMR). These variations

are determined by the three-dimensional geometry of the Fermi surface and the momentum-dependence of the scattering rate.

3.2.1 Transport calculations in a magnetic field

The basic premise of ADMR is that the velocities of charge-carrying quasiparticles are modified by the Lorentz force in a magnetic field. The approach most suitable for calculating angle-dependent magnetoresistance was formulated by Chambers[41]. It provides an intuitive prescription for calculating the full conductivity tensor σ_{ij} in a magnetic field $\boldsymbol{B}$, starting from a tight-binding model of the electronic band structure $\epsilon(\boldsymbol{k})$. Chambers' solution is

$$\sigma_{ij} = \frac{e^2}{4\pi^3}\int d^3\boldsymbol{k}\left(-\frac{df_0}{d\epsilon}\right) v_i[\boldsymbol{k}(t=0)]\int_{-\infty}^{0} v_j[\boldsymbol{k}(t)]\, e^{t/\tau}dt, \tag{3.1}$$

where $\int d^3\boldsymbol{k}$ is an integral over the entire Brillouin zone, $\left(-\frac{df_0}{d\epsilon}\right)$ is the derivative with respect to energy of the equilibrium Fermi distribution function, v_i is the i^{th} component of the quasiparticle velocity, and $\int_{-\infty}^{0} dt$ is an integral over the lifetime, τ, of a quasiparticle. The Fermi velocity is calculated from the tight binding model as $\boldsymbol{v}_{\text{F}} = \frac{1}{\hbar}\vec{\nabla}_{\boldsymbol{k}}\epsilon(\boldsymbol{k})$. The magnetic field, including its orientation with respect to the crystal axes, enters through the Lorentz force, which acts to evolve the momentum $\boldsymbol{k}$ of the quasiparticle through $\hbar\frac{\mathrm{d}\boldsymbol{k}}{\mathrm{d}t} = e\boldsymbol{v}\times\boldsymbol{B}$. Because the magnetic field is included explicitly in this manner, Chambers' solution has the advantage of being exact to all orders in magnetic field.

The conductivity of a general electronic dispersion $\epsilon(\boldsymbol{k})$ can be calculated using Equation 3.1 [64]. The factor $\left(-\frac{df_0}{d\epsilon}\right)$ is approximated as a delta function at the Fermi energy in the limit that the temperature T is much smaller than any of the hopping parameters in $\epsilon(\boldsymbol{k})$, as is the case for our experiments. This delta function transforms the integral over the Brillouin zone into an integral over the Fermi surface, and introduces a factor of $1/|\vec{\nabla}_{\boldsymbol{k}}\epsilon(\boldsymbol{k})|$, which is the density of states. To perform the integrals in Equation 3.1 numerically, the Fermi surface is discretized, usually into 10 to 15 layers along k_z, with 60 to 100 points per

k_z layer, and each point is evolved in time using the Lorentz force equation. This moves the quasiparticles along cyclotron orbits around the Fermi surface, and their velocity is recorded at each position and integrated over time. The weighting factor $e^{t/\tau}$ accounts for the scattering of the quasiparticles as they traverse the orbit. In general, τ is taken to be a function of momentum, $\tau(\boldsymbol{k})$, and then the factor $e^{t/\tau}$ is replaced by $e^{\int_t^0 dt'/\tau(\boldsymbol{k}(t'))}$. Equation 3.1 can be used to calculate any component of the semiclassical conductivity tensor. We use it to calculate ρ_{zz} in Figure 3.2, 3.4, 3.6 and 3.9. Note that, because of the highly 2D nature of the Fermi surface of Nd-LSCO, we neglect the off-diagonal components of the conductivity tensor and use

$$\rho_{zz} \approx 1/\sigma_{zz}. \tag{3.2}$$

For a quasi-two dimensional Fermi surface with simple, sinusoidal warping, ρ_{zz} can be calculated analytically from Equation 3.1 and Equation 3.2 in the limit where τ is long [65]. The exact calculation contains special "Yamaji" angles where all cyclotron orbits have the same cross-sectional area perpendicular to the magnetic field and where the v_z component of the Fermi velocity averages to zero around each orbit. This cancellation of v_z results in maxima in the c-axis resistivity at these angles. The Yamaji angles are determined by the geometry of the FS, and therefore by measuring the angular positions of the resistivity maxima one can construct the FS geometry. For more complex FS geometries, Equation 3.1 and Equation 3.2 must be calculated numerically but the intuition still holds—at certain angles the resistivity is maximized because v_z is more effectively averaged toward zero (see subsection 3.3.1 for more information).

To reconstruct the FS geometry from the ADMR data we start with a tight-binding model $\epsilon(\boldsymbol{k})$ that respects the geometry of the transfer integrals of the material, define the Fermi velocity through $\boldsymbol{v} = \frac{1}{\hbar}\boldsymbol{\nabla}_{\mathbf{k}}\epsilon$, and then tune the tight-binding parameters until the calculated ρ_{zz} matches the measured data. In addition to the FS geometry, ADMR is sensitive to the momentum dependence of the quasiparticle scattering. This is captured

in Equation 3.1 by introducing $\tau(\boldsymbol{k})$. We separate the scattering rate into isotropic and anisotropic components, $1/\tau(\boldsymbol{k}) = 1/\tau_{\rm iso} + 1/\tau_{\rm aniso}(\boldsymbol{k})$. These two components can have distinct temperature dependences as demonstrated in Tl-2201 [66]. The approach of using Equation 3.1 and Equation 3.2 to determine Fermi surfaces has been particularly successful in 2D metals such as organic conductors [67] and Sr_2RuO_4 [20]. In cuprates, ADMR has been measured in the overdoped regime ($p > p^\star$) [50, 48], in the underdoped regime with CDW order ($p \approx 0.1 \ll p^\star$)[13], and in electron-doped materials [68], but never in the pseudogap phase in the absence of CDW order.

3.2.2 Samples and transport measurements

To investigate the possibility of Fermi surface reconstruction below $p^\star$, we turn to the cuprate $La_{1.6-x}Nd_{0.4}Sr_xCuO_4$ (Nd-LSCO). The critical doping $p^\star = 0.23$ that marks the onset of the pseudogap phase in Nd-LSCO has been well-characterized by transport [9, 10], specific heat [69] and ARPES [5]. At $p = 0.20$, a gap opens along the "anti-nodal" directions of the Brillouin zone ($\phi = 0°$, $90°$, $180°$, and $270°$) upon cooling below $T^\star = 75$ K, followed by an upturn in the resistivity; at $p = 0.24$, ARPES detects no anti-nodal gap and the resistivity remains perfectly linear down to the lowest measured temperature. Note that the highest doping where X-ray scattering detects CDW order in Nd-LSCO is $p = 0.17$ [11]. As with other cuprates [70, 71], the onset of CDW order in Nd-LSCO coincides with a downturn of the Hall coefficient toward negative values [72]. At $p = 0.20$ and above, the Hall coefficient remains positive at all temperatures and magnetic fields [10]. This suggests that the quasiparticles responsible for transport (and hence ADMR) do not feel the influence of any remnant CDW order at the dopings where we perform our measurements, in agreement with the absence of any CDW modulations detected by X-ray diffraction and the Seebeck coefficient at $p = 0.18$ and above [73, 11].

Single crystals of $La_{2-y-x}Nd_ySr_xCuO_4$ (Nd-LSCO) were grown at the University of Texas at Austin using the travelling-float-zone technique, with a Nd content $y = 0.4$ and nominal Sr concentrations $x = 0.20$, 0.21 and 0.25. The hole concentration p is given by $p = x$, with an error bar ± 0.003, except for the $x = 0.25$ sample, for which the doping is $p = 0.24 \pm 0.005$ (for more details, see ref. [10]). The value of T_c, defined as the point of zero resistance, is: $T_c = 15.5$, 15 and 11 K for samples with $p = 0.20$, 0.21 and 0.24, respectively. The pseudogap critical point in Nd-LSCO is at $p^* = 0.23$ (ref. [10]).

Resistivity measurements were performed in the 45 T hybrid magnet at the National High Magnetic Field Lab in Tallahassee, USA. The sample resistance was measured with a standard 4-point contact geometry using a Stanford Research 830 Lock-In Amplifier. The samples were driven with $I_{RMS} = 1$ mA from a Keithley 6221 Current Source. Temperature was stabilized to within ± 1 mK around the target temperature at each angle. Uncertainty of the absolute temperature due to thermometer magnetoresistance is negligible at $T = 25$ K. The thermometer was mounted at a fixed point on the probe near the sample but not on the rotating platform. Thus, the magnetoresistance of the thermometer did not change as the sample was rotated.

At $p = 0.21$ and 0.24 the upper critical fields of Nd-LSCO are, respectively, 15 T and 10 T for $\boldsymbol{B} \parallel c$ [69]. By applying a magnetic field of $B = 45$ T at both $T = 25$ K both samples remain in the normal state while rotating the field from $\boldsymbol{B} \parallel c$ to $\boldsymbol{B} \parallel a$.

The polar angle θ between the crystalline c-axis and the magnetic field was changed continuously *in situ* from $\approx -15^\circ$ to $\approx 110^\circ$ using a single-axis rotator. A voltage proportional to the angle was recorded with each angle sweep. The angle θ was calibrated by finding symmetric points in the resistivity and scaling the measured voltage such that the symmetric points lie at $\theta = 0^\circ$ and 90° (see Figure 3.3). This procedure resulted in an uncertainty in θ of $\pm 0.5^\circ$. The azimuthal angle ϕ was changed by placing the sample on top of G-10 wedges machined at different angles: 15°, 30° and 45°. An illustration of the sample mounted

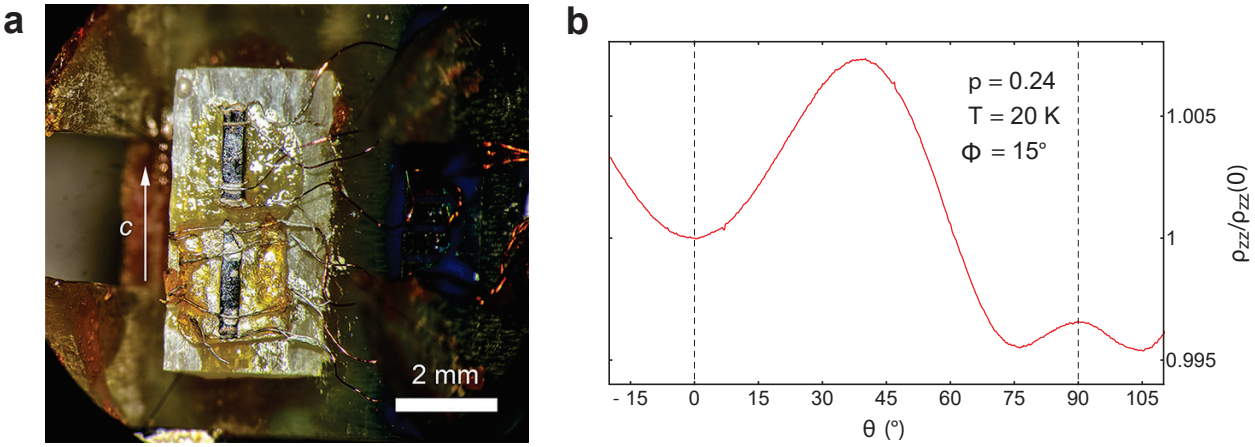

Figure 3.3: (**a**) An illustration of the sample mounting. The two samples here are mounted on a G-10 wedge to provide a ϕ angle of 30°. Additional wedges provided angles of $\phi = 15°$ and 45°; (**b**) ADMR as a function of θ angle from $-15°$ to 110° and $\phi = 0$ at $T = 20$ K for Nd-LSCO $p = 0.24$, showing the symmetry of the data about these two angles.

on the rotator stage, with a G-10 wedge to set the azimuthal angle to be 30°, is shown in Extended Data Figure 6. The samples and wedges were aligned under a microscope by eye to an accuracy in ϕ of $\pm 2°$.

3.3 ADMR of Nd-LSCO with a doping $\mathbf{p = 0.24 > p^*}$

Figure 3.2d shows the ADMR of Nd-LSCO at $p = 0.24$, at $T = 25$ K and $B = 45$ T. We fit the data using a three dimensional tight binding model of the Fermi surface that accounts for the body-centred tetragonal crystal structure of Nd-LSCO [6],

$$\begin{aligned}\epsilon(k_x, k_y, k_z) = &- \mu - 2t[\cos(k_x a) + \cos(k_y a)] \\ &- 4t' \cos(k_x a)\cos(k_y a) - 2t''[\cos(2k_x a) + \cos(2k_y a)] \\ &- 2t_z \cos(k_x a/2)\cos(k_y a/2)\cos(k_z c/2)[\cos(k_x a) - \cos(k_y a)]^2,\end{aligned} \tag{3.3}$$

where μ is the chemical potential, t, t', and t'' are the first, second, and third nearest neighbour hopping parameters, t_z is the inter-layer hopping parameter, $a = 3.75$ Å is the in-plane lattice constant of Nd-LSCO, and $c/2 = 6.6$ Å is the CuO_2 layer spacing. The

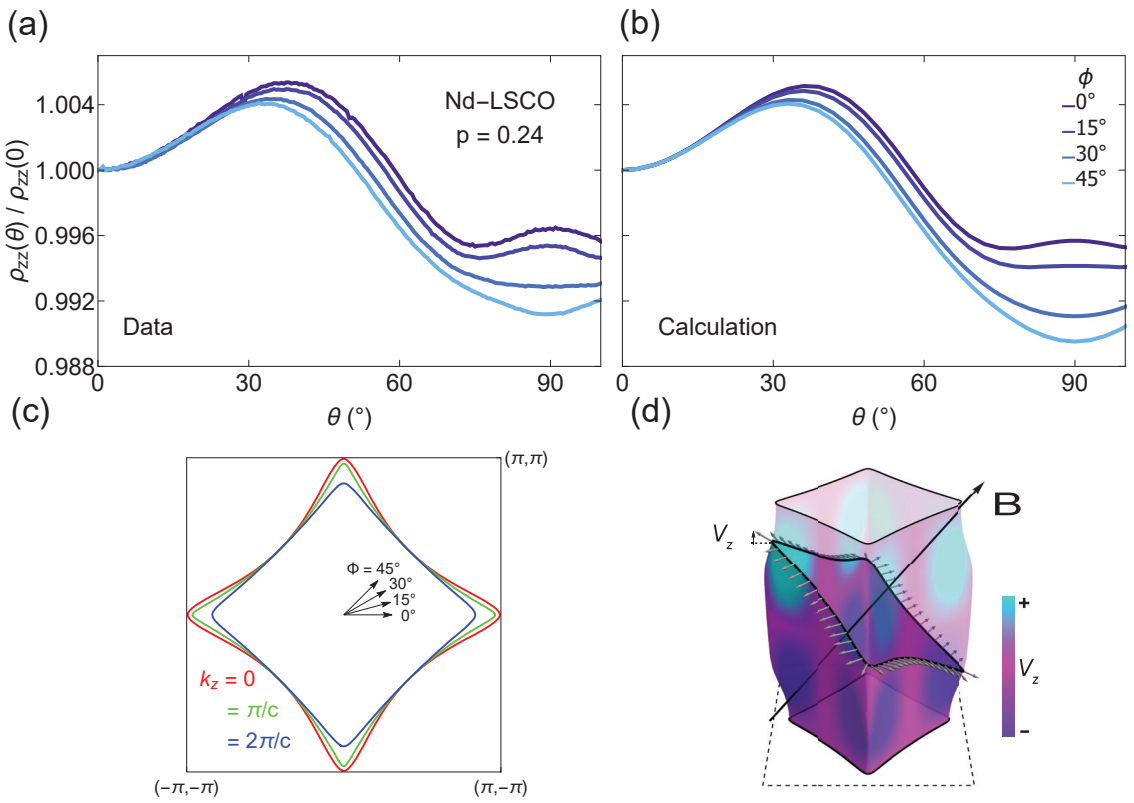

Figure 3.4: (**a**) The ADMR of Nd-LSCO at $p = 0.24$ as a function of θ at $T = 25$ K and $B = 45$ T. (**b**) Simulations obtained from the Chambers formula using the tight-binding parameters from Extended Data Table 1 and the scattering rate model from Equation 3.4. (**c**) The Fermi surface of Nd-LSCO $p = 0.24$ obtained from the ADMR calculations, with cuts shown at $k_z = 0$, π/c, and $2\pi/c$, where c is the height of the body-centered-tetragonal unit cell (and $c/2$ is the distance between copper oxide layers). (**c**) The full 3D Fermi surface. The colouring corresponds to the v_z component of the Fermi velocity, with positive v_z in light blue, negative v_z in purple, and $v_z = 0$ in magenta. A single cyclotron orbit, perpendicular to the magnetic field, is drawn in black, with the Fermi velocity at different points around the orbit indicated with grey arrows. The strong variation in v_z around the cyclotron orbit is what leads to ADMR.

inter-layer hopping has the form factor $\cos(k_x a/2)\cos(k_y a/2)[\cos(k_x a) - \cos(k_y a)]^2$, which accounts for the offset copper oxide planes between layers of the body-centered tetragonal structure [74].

We have used a minimal, phenomenological, anisotropic scattering rate model to fit the

ADMR data of Nd-LSCO $p = 0.24$, which we refer to as the "cosine" model:

$$1/\tau(T, \phi) = 1/\tau_{\text{iso}}(T) + 1/\tau_{\text{aniso}}(T)|\cos(2\phi)|^{\nu}, \tag{3.4}$$

where $1/\tau_{\text{iso}}$ is the amplitude of the isotropic scattering rate, $1/\tau_{\text{aniso}}$ is the amplitude of the ϕ-dependent scattering rate, and ν is an integer. With as few parameters as possible, this model captures the trend of the anti-nodal regions of the Fermi surface to have shorter quasiparticle lifetimes in the cuprates [75, 76], particularly close the van Hove singularity. This model should be seen as the simplest phenomenological model able to capture the correct shape of the real scattering rate, with the least number of free parameters.

We then perform a global optimization over the tight binding and scattering rate parameters using a genetic algorithm (see subsection 3.3.2 for the detail of genetic algorithm), placing loose bounds on the parameters around values determined by previous ARPES measurements [5, 6]. The fit results for the tight-binding and scattering rate parameters are presented in Table 3.1. Although the genetic algorithm was allowed to search over a wide range of parameters, we found that the optimal solution converged towards t', t'' and t_z values extremely close to the ARPES values, with a 7% deviation at most for t_z. Only μ, and therefore the doping p, is substantially different from the ARPES value. The higher doping found by ARPES may be due to the difficulty in accounting for the k_z dispersion, or may be due to different doping at the surface. Nevertheless, the shape of the Fermi surface found by fitting the ADMR data (see Figure 3.4b, c) is electron like and qualitatively identical to the one measured by ARPES [5], and the doping we find ($p = 0.248$) is very close to the nominal one $p = 0.24 \pm 0.005$ [9]. This demonstrates that the Fermi surface is correctly mapped out by our analysis of the ADMR data. In the figures and the analysis presented in this manuscript, we use the tight-binding values from Table 3.1, and for simplicity we refer to them as the "tight-binding values from ARPES ", as they only differ by the chemical potential value..

The right panel of Figure 3.4b shows the results for the ADMR of this optimization:

key features reproduced by the fit include the position of the maximum near $\theta = 40°$, the onset of ϕ-dependence beyond $\theta = 40°$, and the ϕ-dependent peak/dip near $\theta = 90°$. The peak in ρ_{zz} near $\theta = 40°$, which is captured well by the fit, can also be checked against the intuitive picture of ADMR described earlier: the position of this peak should be related to the length of the Fermi wavevector, k_{F}. For a Fermi surface with the simplest sinusoidal dispersion along k_z, an analytic calculation of Equation 3.2 shows that the ADMR changes with angle as $\rho_{zz} \propto 1/\left(J_0\left(ck_F \tan\theta\right)\right)^2$, where c is the inter-layer lattice constant, k_{F} is the Fermi wavevector, and J_0 is the 0^{th} Bessel function of the first kind. While the analytic expression for ρ_{zz} is not exact for the particular form of interlayer hopping found in Nd-LSCO, in session 3.3.1 we show that the maxima in the resistivity coincide with the angles where v_z is best averaged to zero. Our analysis including the proper interlayer hopping shows that the peak in ρ_{zz} near $\theta = 40°$ suggests that $k_F \approx 7$ nm^{-1} along the zone diagonal, which is very close to the FS shown in Figure 3.4c. This suggests that the ADMR at $p = 0.24$ exhibits features consistent with a large, unreconstructed Fermi surface, as also observed by ARPES.

In addition to the Fermi surface geometry, ADMR is sensitive to the momentum-dependent quasiparticle scattering rate. We find that the $p = 0.24$ data is best described by a highly anisotropic scattering rate that is largest near the anti-nodal regions of the Brillouin zone and smallest near the nodal regions. More details of the scattering rate model and its temperature dependence can be found in [48].

3.3.1 Yamaji angle analogy

An intuitive picture for interpreting the structure of ADMR is that minima in the conductivity (maxima in the resistivity) occur at angles where a component of the Fermi velocity averages toward zero for most of the cyclotron orbits. In a quasi-2D material with a simple

	t (meV)	t'	t''	t_z	μ	p	$1/\tau_{\rm iso}$ (ps^{-1})	$1/\tau_{\rm aniso}$ (ps^{-1})	ν
ADMR	160 ± 30	$-0.1364t$	$0.0682t$	$0.0651t$	$-0.8243t$	0.248	12.595 ± 0.002	63.823 ± 0.26	12 ± 1
ARPES	190	-0.136t	0.068t	0.07t		0.28			

Table 3.1: **Tight-binding parameters from the fit to the ADMR data at $p = 0.24$.** Best fit tight-binding values for the Nd-LSCO $p = 0.24$ ADMR data (using the cosine scattering rate model of Equation 3.4). The results are extremely close to ARPES tight-binding values reported in [5] and [6], reproduced here on the second line. Error bars on the AMDR-derived hopping parameters and chemical potential are all ± 0.0005, and were obtained following the procedure described in subsection 3.3.2. The error bar on the value of t_z measured by ARPES is $\pm 0.02t$ (J. Chang and M. Horio, private communication.)

sinusoidal dispersion along the k_z direction and $\omega_c\tau \gg 1$, the ADMR has peaks at θ values corresponding to zeros of $J_0(ck_F \tan\theta)$, where $J_0(x)$ is the $0^{\rm th}$ order Bessel function of the first kind, c is the interlayer lattice constant, and k_F is the average Fermi wavevector [65]. These special angles are referred to as Yamaji angles—at these angles all Fermi surface cross-sectional areas are equal and the c-axis Fermi velocity (v_z) averages to zero for all cyclotron orbits [77].

For Nd-LSCO at $p = 0.24$, the Fermi surface along the k_z direction is more complicated than a simple sinusoidal warping and the material is also far from the $\omega_c\tau \gg 1$ limit. Similar intuition to the simple Yamaji angle scenario, however, still holds at low θ. While there are no longer angles where v_z averages to precisely to zero for all cyclotron orbits there are still angles where the orbital average of v_z is minimal. At these same angles where the orbitally-averaged v_z is minimal the cyclotron orbits all have similar areas. This means that the rate of change of area as one moves along k_z is a minimum at certain angles, and these angles correspond to maxima in the resistivity.

As shown in Figure 3.5, the variation in the cyclotron orbit area drops to a minimum at around 32° for $\phi = 0°$. This is near the angle where we find a peak in the ADMR for $p = 0.24$, indicating that this angle is indeed one where v_z is averaged close to zero most effectively. In addition, as ϕ is rotated toward 45°, the minimum in rate of change of the area moves to lower θ, tracking the behaviour of the peak in the ADMR (the lifetime τ has

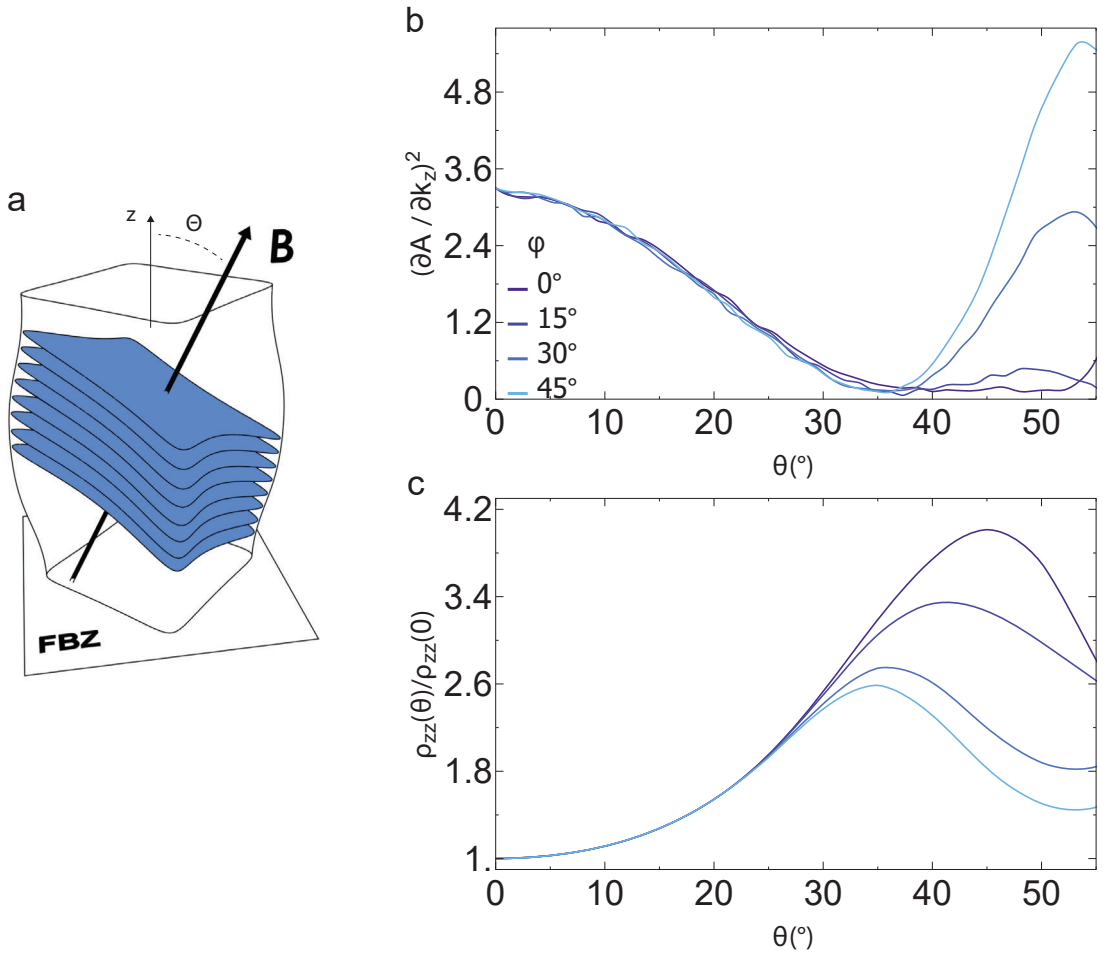

Figure 3.5: (**a**) The Fermi surface of Nd-LSCO $p = 0.24$ in the first Brillouin zone. The black arrow represents the direction of the magnetic field $\boldsymbol{B}$. Each blue surface represent the area enclosed by a cyclotron orbit for this particular direction of $\boldsymbol{B}$ (here just a few orbits are shown as examples). (**b**) The square of the rate-of-change of Fermi surface area as a function of k_z: when this quantity is zero it means that all orbits have the same area. (**c**) ADMR calculated for the FS shown in (a) with $\omega_c\tau$ chosen to be long enough to emphasize the peaks in the resistivity where there are minima in panel (b).

been increased for the calculated ADMR in Figure 3.5c to highlight the peak.) Thus, while the interlayer warping of Nd-LSCO is not a simple sinusoid, and $\omega_c\tau \ll 1$, the Yamaji-angle picture still provides the correct intuition for interpreting the ADMR.

3.3.2 Genetic algorithm

Computing the conductivity as described above involves free parameters (e.g. t', t'', t_z, μ, τ_{iso}, τ_{aniso}, ν) which can be written as a vector $\boldsymbol{x}$. The optimal $\boldsymbol{x}$, which we refer to as $\boldsymbol{x}^*$, minimizes the chi-square (χ^2) statistic between the resistivity from the model $\rho_{zz}^{model}(\boldsymbol{x}, \theta, \phi)$ and the measured resistivity $\rho_{zz}^{\text{data}}(\theta, \phi)$ at all magnetic field orientations (θ, ϕ):

$$\chi^2(\boldsymbol{x}) = \sum_{(\theta,\phi)} \left(\rho_{zz}^{model}(\boldsymbol{x}, \theta, \phi) - \rho_{zz}^{\text{data}}(\theta, \phi)\right)^2, \tag{3.5}$$

We thus seek $\boldsymbol{x}^*$ such that:

$$\boldsymbol{x}^* = \arg\min_{\boldsymbol{x}} \chi^2(\boldsymbol{x}). \tag{3.6}$$

Using the Chambers formula to fit the ADMR measurements can be tricky for standard optimization algorithms such as gradient based methods. They are either slow to converge, highly sensitive to the initial conditions, or most annoyingly they tend to get stuck in local minima of the $\chi(\boldsymbol{x})$ landscape. That is the reason why we turned to a genetic algorithm (or "differential evolution") as a global optimization method which can avoid these issues. The genetic algorithm has become a standard fitting routine in science, it is carefully detailed in the supplementary information of [13]. For this study we used the differential evolution algorithm from the Python package *lmfit* [78] and our own C++ implementation(see Appendix B for the C++ code). We back checked the efficiency of the genetic algorithm with two other global optimizers, such as AMPGO (Adaptive Memory Programming for Global Optimization) and SHGO (Simplicial Homology Global Optimization) also made available in *lmfit* [78]. The three optimizers all converged to the same results, confirming the robustness of our fit procedure.

We calculate the χ^2 values of each member of the population after each generation of optimization. The distribution of all these χ^2 values follows a Gaussian-like distribution.

The genetic algorithm stops when the standard deviation of this distribution has reached less than 1% of the mean value of the distribution.

3.4 ADMR of Nd-LSCO with a doping $p = 0.21 < p^*$

We now turn to Nd-LSCO $p = 0.21$, below $p^\star$ and inside the pseudogap phase, where ARPES finds discontinuous segments of FS known as 'arcs' [53]. Upon comparison of Figure 3.2c and Figure 3.2d, it is immediately apparent that the structure of the ADMR changes qualitatively upon entering the pseudogap phase. In particular, the resistivity peak near $\theta = 40^\circ$ has disappeared at $p = 0.21$. The qualitative differences in the data arise either from a change in the FS geometry, or from a large increase in the scattering rate for the anti-nodal quasiparticles (e.g. the generation of Fermi arcs).

We test several different scenarios to understand the change in the ADMR across $p^\star$. These scenarios can be divided into two classes: those that change only the quasiparticle scattering rate, and those that reconstruct the Fermi surface.

3.4.1 Scattering rate model

First, we use the same FS model and scattering rate that fit the ADMR at $p = 0.24$ and simply adjust the chemical potential to decrease the hole concentration to $p = 0.21$. The simulated data for this model are shown in Figure 3.6a. Instead of describing the data for $p = 0.21$, however, this simulation appears close to that for $p = 0.24$. This is to be expected: only the FS near the anti-nodal region changes appreciably upon lowering the doping, and the ADMR is less sensitive to this region due to its high scattering rate. Therefore, something beyond a simple change in the chemical potential must occur when crossing $p^\star$.

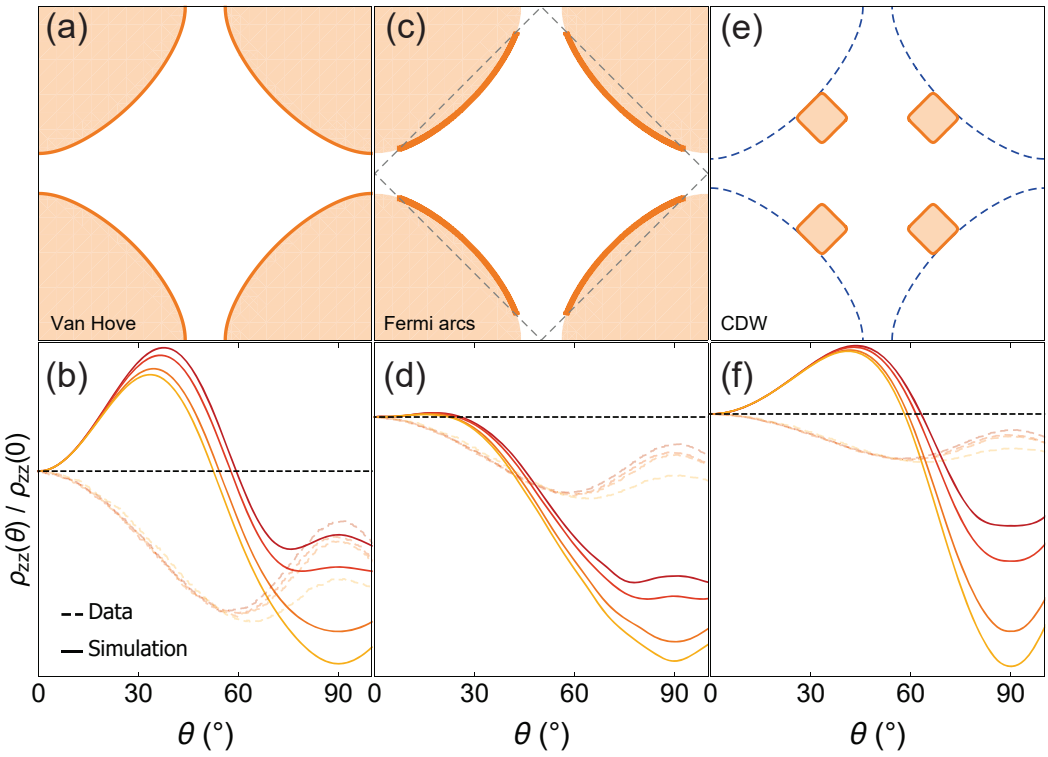

Figure 3.6: The top three panels (**a, c** and **e**) show the Fermi surface for three different scenarios and the bottom three panels (**b, d** and **f**) show the resulting ADMR simulations. (**b**) ADMR calculated using the same parameters as in Figure 3.4a (including the scattering rate) but with the chemical potential shifted past the van Hove singularity to $p = 0.21$. The ADMR for this model is largely unchanged from the fit at $p = 0.24$. (**c**) Schematic of Fermi arcs, whereby the FS terminates at the antiferromagnetic zone boundary (grey dashed line) due to incoherence of the quasiparticles past that point. This is modelled as a scattering rate that increases considerably upon crossing the zone boundary. This model, shown in (**d**), fails to fit the data, particularly near $\theta = 90°$. (**e**) Electron pockets obtained from period-3 CDW order are shown in orange, along with the original FS shown as a blue dashed line. The calculations of the ADMR for these electron pockets are shown in (**f**) but do not reproduce the data. Similar nodal electron pockets are able to account for the ADMR in $YBa_2Cu_3O_{6+x}$ at $p = 0.11$ [13], where CDW order is present.

Next we test three other scattering rate models (on the large, unreconstructed FS): the same model used at $p = 0.24$ but now with the scattering rate parameters allowed to vary (Figure 3.7c); isotropic scattering around the entire FS (Figure 3.7b); and a model of 'Fermi arcs' where the quasiparticle lifetime diminishes rapidly past the antiferromagnetic zone boundary on the FS in Figure 3.6c. Even after performing fits using the genetic al-

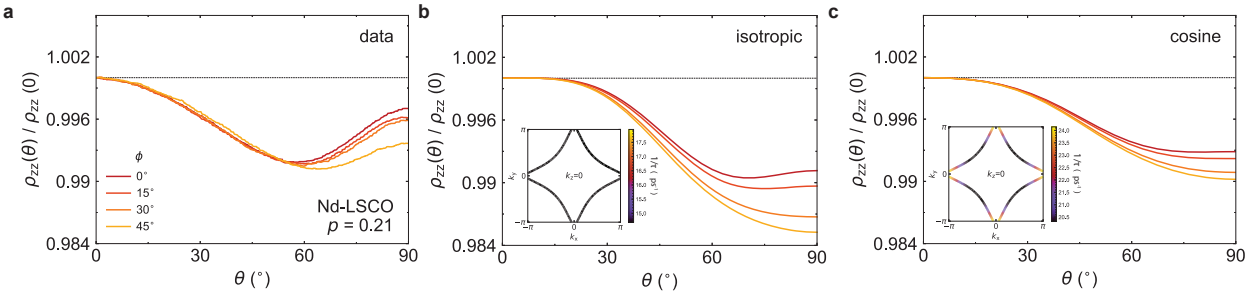

Figure 3.7: (**a**) ADMR data on Nd-LSCO $p = 0.21$ at $T = 25$ K and $B = 45$ T; (**b**, **c**) The best fits for the ADMR data in (a) using the band structure ARPES values for Nd-LSCO $p = 0.24$ with the chemical potential shifted across the van Hove point (at $p \approx 0.23$) to $p = 0.21$, where the Fermi surface is hole-like. Insets represent the scattering rate distribution values over the hole-like Fermi surface at $p = 0.21$. In (b), the scattering is isotropic over the Fermi surface; in (c) we use the cosine scattering rate model (this figure differs from Figure 3.6b because there we only shift the chemical potential, while here we show the best-fit using this model.)

gorithm, allowing for a broad range of band-structure and scattering-rate parameters, none of these scattering rate models on the large unreconstructed hole-like FS is able to reproduce the ADMR at $p = 0.21$. Note that the average strength of the scattering does not seem to change much as the system crosses $p^\star$, since the magnitude of the ADMR, which is essentially governed by the magnitude of $1/\tau$, is roughly the same at $p = 0.21$ and at $p = 0.24$ (Figure 3.2).The inability of any of these scattering rate models to fit the ADMR at $p = 0.21$ suggests that the FS must be reconstructed into a new, geometrically distinct, FS in the pseudogap phase.

3.4.2 CDW Fermi surface reconstruction

The first reconstruction we consider is a small electron pocket at nodal positions in the Brillouin zone, as in Figure 3.6e. This FS is the result of a bi-axial charge density wave, as found in several underdoped cuprates [79, 80], and is likely the origin of the small electron pocket found in $YBa_2Cu_3O_{6+x}$ and $HgBa_2CuO_{4+x}$ [55]. This Fermi surface accounts well

for the ADMR of $YBa_2Cu_3O_{6.6}$ at $p = 0.11$, where there is CDW order [13]. A bi-axial charge density wave (CDW) with a period near to 3 lattice spacings is thought to underlie the reconstructed pocket seen in quantum oscillation experiments [81, 13]. We simulate such a reconstruction by starting with the ARPES tight binding values for Nd-LSCO at $p = 0.24$ and perform a period-three, bi-axial wavevector reconstruction of the Fermi surface. As with the (π,π) reconstruction, we perform a 2D reconstruction and maintain the same interlayer coupling terms used in the unreconstructed case. This Fermi surface reconstruction produces multiple pockets and open sheets, similar to what was shown in [82]. We calculate the ADMR for only the diamond-shaped Fermi surface because this is the only surface that has been reported by quantum oscillations in underdoped cuprates [55, 83], and because it is the only Fermi surface needed to model the ADMR in $YBa_2Cu_3O_{6.6}$ [13]. The inclusion of any other Fermi surfaces would lead to a value of the normal-state specific heat that is larger than what is measured [84].

The Hamiltonian used for finding the in-plane Fermi surface can be written as follows [85],

$$H = \sum_{\boldsymbol{k}} [\epsilon_0(\boldsymbol{k}) c^\dagger_{\boldsymbol{k}} c_{\boldsymbol{k}} - \sum_{\boldsymbol{Q}} \Delta_{\boldsymbol{Q}}(\boldsymbol{k} + \boldsymbol{Q}/2) c^\dagger_{\boldsymbol{k}+\boldsymbol{Q}} c_{\boldsymbol{k}}], \tag{3.7}$$

where the sum over $\boldsymbol{k}$ extends over the entire Brillouin zone of the square lattice, Δ_{Q} is the gap of the CDW and $\boldsymbol{Q}$ the wave vectors of the charge ordering. For a bidirectional charge density wave with a period of three lattice spacings, the sum over $\boldsymbol{Q}$ extends over the 4 values $(\pm\frac{2\pi}{3}, 0)$ and $(0, \pm\frac{2\pi}{3})$. The in-plane electronic dispersion is the same as the in-plane dispersion ϵ_0 described in Equation 3.9. The Fermi surface is found by selecting the eigenvalue of the resulting 9×9 matrix that corresponds to the diamond-shaped Fermi surface showed in Figure 3.6e.

We calculate the ADMR using the Chambers formula for this model. The result is shown in Figure 3.8 for a number of different CDW strengths and a $d-$wave form factor. The simulated ADMR is somewhat reminiscent of the $p = 0.24$ data, except that the peak that

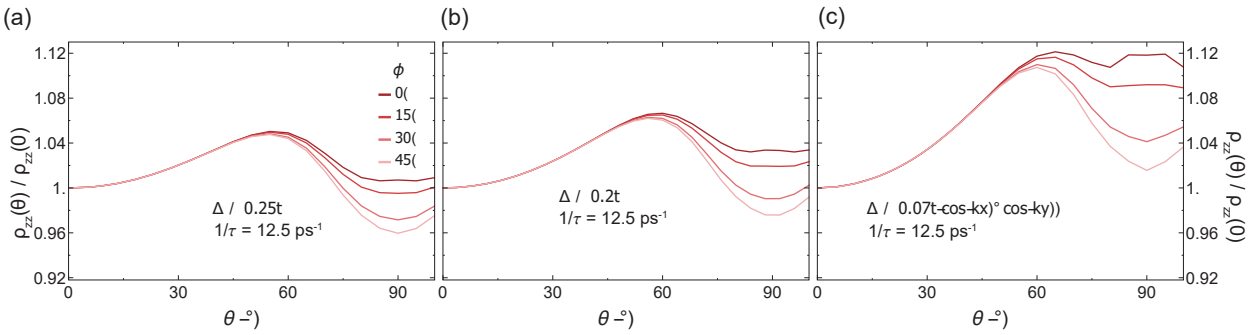

Figure 3.8: Calculation of ADMR for a period three CDW Fermi surface reconstruction with $1\tau = 12.5$ ps^{-1}. (**a**) Calculation using a gap, $\Delta = 0.25t$. (**b**) Calculation using a gap, $\Delta = 0.2t$. (**c**) Calculation using a gap with a d-wave form factor, $\Delta = 0.07t(cos(kx) - cos(ky))$.

was found at around $\theta = 30°$ for $p = 0.24$ has been pushed out to $\theta = 60°$. This qualitative similarities arise because both the unreconstructed Fermi surface and the small reconstructed diamond are similar in shape. The features are pushed to higher θ for the reconstructed case because k_F is smaller. This suggests that the FS transformation at $p = 0.21$ is not due to the same CDW order that produces the nodal electron pocket found in other underdoped cuprates. This is consistent with the Hall and Seebeck coefficients, which remain positive at all temperatures and magnetic fields in Nd-LSCO at $p = 0.21$ [10, 86], whereas negative (or negative-trending) Hall and Seebeck coefficients are a ubiquitous signature of charge order in the cuprates, observed in four distinct families of cuprates [70, 71, 87], including Nd-LSCO at $p = 0.12$ [72]. It is also consistent with recent X-ray scattering experiments, which find no charge order at dopings greater than $x = 0.17$ in Nd-LSCO [11].

3.4.3 (π,π) Fermi surface reconstruction

Next, we consider small hole pockets centred around the nodal directions of the Fermi surface, as shown in (Figure 3.9). Such nodal hole pockets arise in various theoretical scenarios [88, 89, 90, 91, 63] and the Fermi arcs seen by ARPES could correspond to the front side

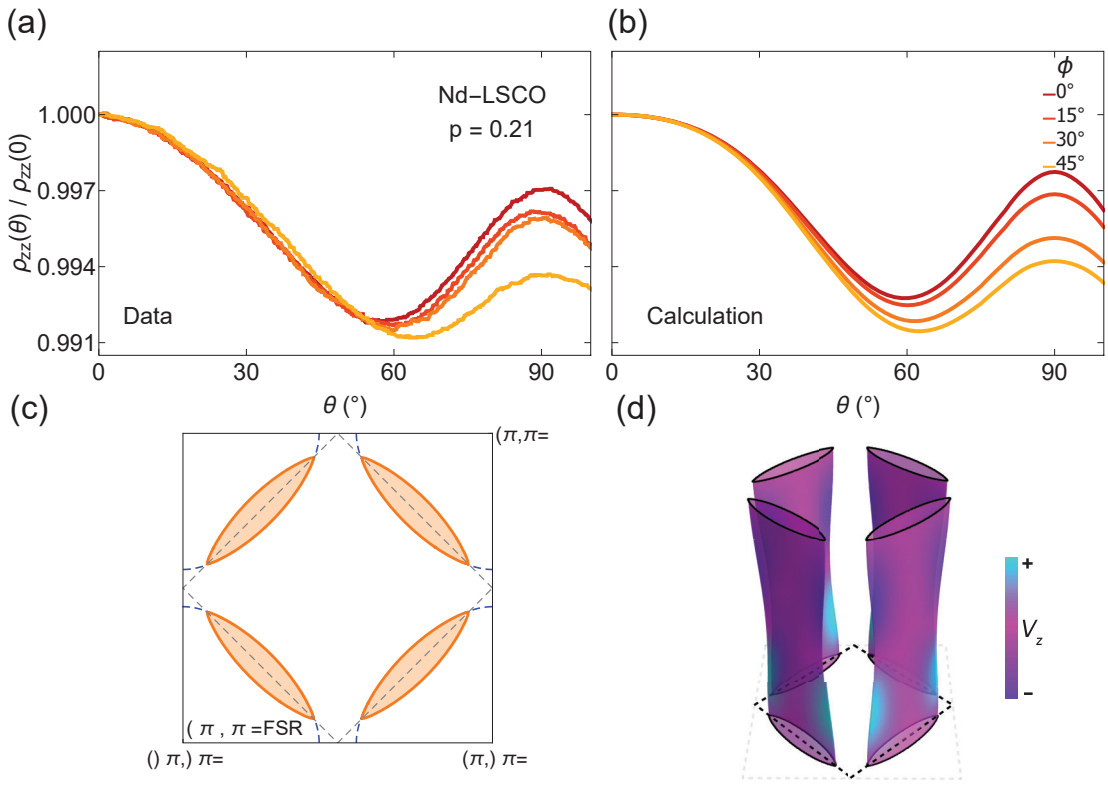

Figure 3.9: (**a**) Measured ADMR of Nd-LSCO at $p = 0.21$ as a function of θ at $T = 25$ K and $B = 45$ T. (**b**) Calculated ADMR for the FS shown in (c) with an isotropic scattering rate. (**c**) FS consisting of four nodal hole pockets. These pockets are implemented via a model of antiferromagnetic order with a wavevector of $Q = (\pi, \pi)$ and a gap of 55 K, with the electron pockets removed to produce agreement with the measured Hall coefficient. (**d**) The full 3D Fermi surface at $p = 0.21$ after reconstruction.

of such pockets. In practice, we simulate such a reconstruction by starting with the tight binding model at ADMR values for Nd-LSCO $p = 0.24$ found in Table 3.1 and performing a two-dimensional (π, π) reconstruction, maintaining the same interlayer coupling terms used in the unreconstructed case. The tight binding model is then

$$\begin{aligned}\epsilon_{(\pi,\pi)}(k_x, k_y, k_z) = &- \mu + \tfrac{1}{2}\left[\epsilon_0(k_x, k_y, k_z) + \epsilon_0(k_x + \pi/a, k_y + \pi/a, k_z))\right] \\ &- \tfrac{1}{2}\sqrt{4\Delta^2 + \left[\epsilon_0(k_x, k_y, k_z) - \epsilon_0(k_x + \pi/a, k_y + \pi/a, k_z)\right]^2} \\ &- 2t_z \cos(k_z c/2)\cos(k_x a/2)\cos(k_y a/2)[\cos(k_x a - \cos(k_y a))]^2,\end{aligned} \tag{3.8}$$

T (K)	μ	$1/\tau_{\rm iso}$ (ps^{-1})	Δ (K)
25	$-0.495t \pm 0.01$	22.88 ± 0.30	55 ± 11

Table 3.2: **Results of the fit of the Nd-LSCO $p = 0.21$ data with (π,π) reconstruction.** Fit parameter values for Nd-LSCO $p = 0.21$ plotted in Figure 3.9f. The band structure parameters were kept fixed at ARPES values [5]. Error bars were obtained following the procedure described in the subsection 3.3.2.

where the unreconstructed ϵ_0 is given by

$$\begin{aligned}\epsilon_0(k_x, k_y, k_z) = &-2t[\cos(k_x a) + \cos(k_y a)] - 4t' \cos(k_x a)\cos(k_y a) \\ &- 2t''[\cos(2k_x a) + \cos(2k_y a)],\end{aligned} \tag{3.9}$$

Δ is the gap size, t, t', t'' represent the first, second, and third nearest neighbor hopping parameters, μ is the chemical potential, and t_z is the interlayer hopping parameter.

Note that the above equations consist of a 2D antiferromagnetic model with added inter-plane hopping instead of a fully three-dimensional antiferromagnetic model. The reason for this is Nd-LSCO's tetragonal crystal structure, for which the full 3D reconstruction would induce C_4 rotation symmetry breaking (coming from the $[\cos(k_x a/2)\cos(k_x a/2)]$ term in the inter-plane hopping). By performing the 2D reconstruction alone, rotational symmetry in the copper-oxide planes is preserved. Moreover, such a reconstruction is likely to be more consistent with the short-length spin correlations that are incoherent between planes. Note also that short range antiferromagnetic correlations could induce a reconstruction as long as the thermal de Broglie wavelength of the electron (of order a few nanometers at 6 K given the effective mass at $p = 0.21$ [69]) is shorter than the AF correlation length [92].

The ADMR was simulated using Equation 3.8 using a procedure similar to that described above for $p = 0.24$. It was found that an isotropic scattering rate allows to best-fit the data. Thus the scattering rate, the gap magnitude and the chemical potential were the only three parameters allowed to vary using the genetic algorithm. The best fit is presented in Figure 3.9b, and the fit values can be found in Table 3.2. This Fermi surface reproduces all critical features of the data at $p = 0.21$: the resistivity initially decreases with increasing θ;

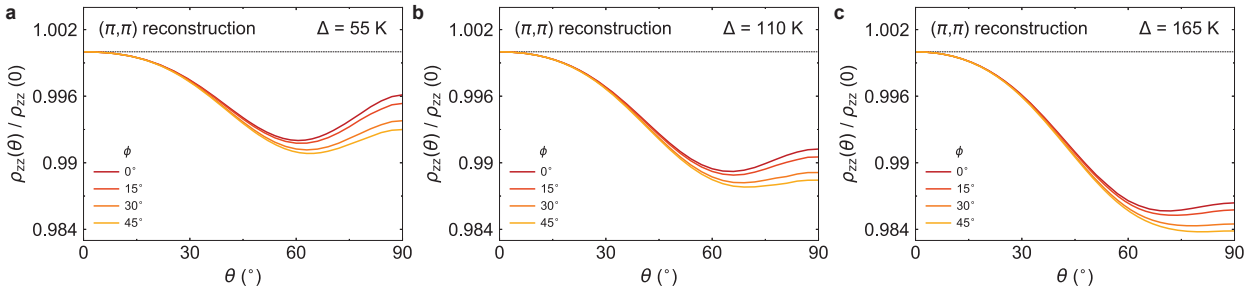

Figure 3.10: ADMR dependence on the gap amplitude with ($\boldsymbol{\pi}$,$\boldsymbol{\pi}$) reconstruction. ADMR calculations with a (π,π) reconstructed Fermi surface for different gap amplitudes at fixed isotropic scattering rate value $1/\tau = 22.88$ ps^{-1}. (**a**) Calculation using a gap, $\Delta = 55$ K. (**b**) Calculation using a gap, $\Delta = 110$ K. (**c**) Calculation using a gap, $\Delta = 165$ K. Note that this within $\approx 40\%$ of the nodal scattering rate at $p = 0.24$, consistent with a nodal hole pockets reconstructed from a the larger Fermi surface.

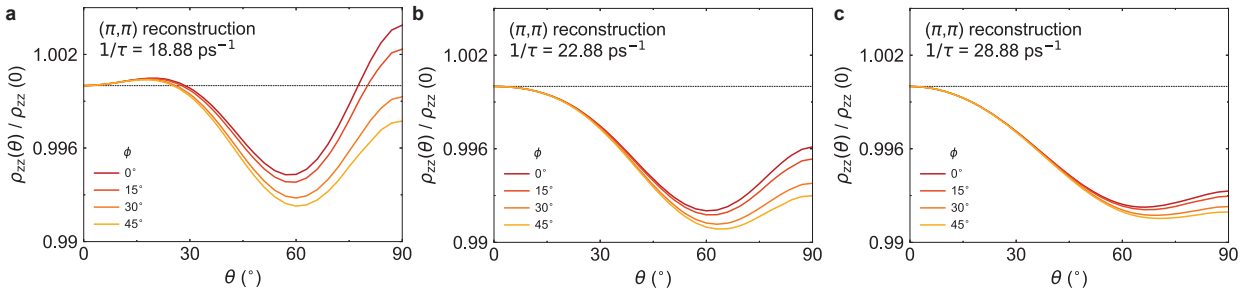

Figure 3.11: ADMR dependence on the scattering rate amplitude with ($\boldsymbol{\pi}$,$\boldsymbol{\pi}$) reconstruction. ADMR calculations with a (π,π) reconstructed Fermi surface for different isotropic scattering rate amplitudes at fixed gap value at $\Delta = 55$ K. (**a**) Calculation using a scattering rate, $1/\tau = 18.88$ ps^{-1}. (**b**) Calculation using a scattering rate, $1/\tau = 22.88$ ps^{-1}. (**c**) Calculation using a scattering rate, $1/\tau = 28.88$ ps^{-1}.

there is a minimum near $\theta = 60°$; and the peak at 90° is strongest along $\phi = 0°$ and weakest along $\phi = 45°$.

To understand the influence of the different parameters on the fit, we show in Figure 3.10 how the ADMR varies with increasing gap size. While the magnitude of the overall drop at $\theta = 90°$ increases with increasing Δ, the variation is rather slow and no strong qualitative change in the simulations are observed. We show the same but as a function of the scattering rate amplitude in Figure 3.11.

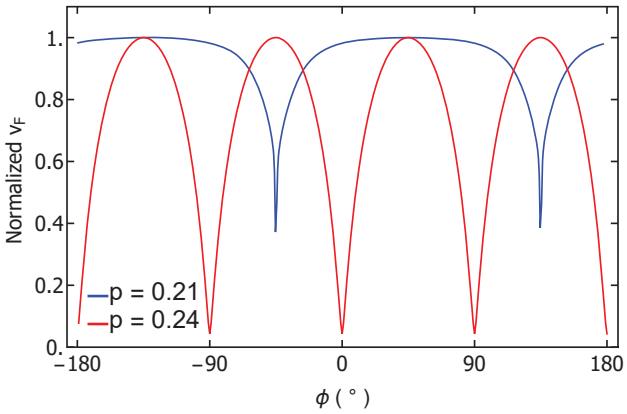

Figure 3.12: Variation in the Fermi velocity around the Fermi surface above and below $p^\star$. The red curve plots the magnitude of the Fermi velocity around the Fermi surface at $p = 0.24$, as shown in Figure 3.4. The blue curve plots the same quantity for a single nodal hole pocket, as shown in Figure 3.9 (the reduction in symmetry is because each nodal hole pocket is 2-fold symmetric). The total anisotropy in v_F around the Fermi surface is a factor of 25 at $p = 0.24$, but just larger than a factor of 2 at $p = 0.21$.

We find that a momentum-independent scattering rate is required to reproduce the data. The reduction in scattering rate anisotropy when moving from the unreconstructed FS at $p = 0.24$ to the nodal hole pockets at $p = 0.21$ may be due to the large reduction in the anisotropy of the density of states. Figure 3.12 plots the magnitude of the Fermi velocity—inversely proportional to the density of states—for both the unreconstructed Fermi surface and the nodal hole pockets. v_F varies by a factor of 25 for the unreconstructed FS, which is likely the origin of the anisotropic elastic scattering rate. At $p = 0.21$, however, v_F varies by just over a factor of two—a huge reduction in anisotropy. This may explain why the scattering rate we find on the nodal hole pockets is roughly isotropic (note that scattering rate is not exactly proportional to the density of states, as it depends on the form of the scattering matrix elements.)

While the relative change in resistivity is reproduced by the model, the absolute value is not reproduced: the absolute resistivity at $\theta = 0°$ is $\rho_{zz} = 35.80$ mΩ cm, whereas the fit produces $\rho_{zz} = 12.93$ mΩ cm. The difference between model and data may be due

to incoherent contributions to the transport, which are not captured by the Boltzmann equation.

The key structures present in the reconstructed hole pockets, which are not present in the model of the arcs, are the sharp corners where the front and backsides of the hole pockets are connected: it is these corners that produce qualitatively different ADMR than is produced by the model of arcs. The gap magnitude (the strength of the potential associated with the FS reconstruction) that best reproduces the data is 5 meV, or $\approx$ 55 K—this gap sets the 'sharpness' of the corners on the hole pockets. Note that this gap is insufficient to remove the anti-nodal electron pockets that also result from a $Q = (\pi, \pi)$ reconstruction. Although a fit can still be obtained with the electron pockets included (as their inclusion only adds more free parameters to the model), we exclude them from the model based on the calculated Hall coefficient. Figure 3.13 compares the data taken at 30 K on Nd-LSCO at $p = 0.21$ (from [10]) with the Hall coefficient calculated from several models. Nodal hole pockets on their own produce the best agreement with the data.

Thus, the change in ADMR moving from $p = 0.24$ to $p = 0.21$ has two sources: a transformation to a Fermi surface consisting of four nodal hole pockets, and a reduction in scattering rate anisotropy.

3.4.4 YRZ Fermi surface reconstruction

There are alternative routes to producing nodal hole pockets similar to what is produced by a ($\boldsymbol{\pi}$,$\boldsymbol{\pi}$) reconstruction. One example is the Yang, Rice, and Zhang (YRZ) ansatz [90], which has been shown to reproduce the decrease in the Hall coefficient below $p^\star$ [91].

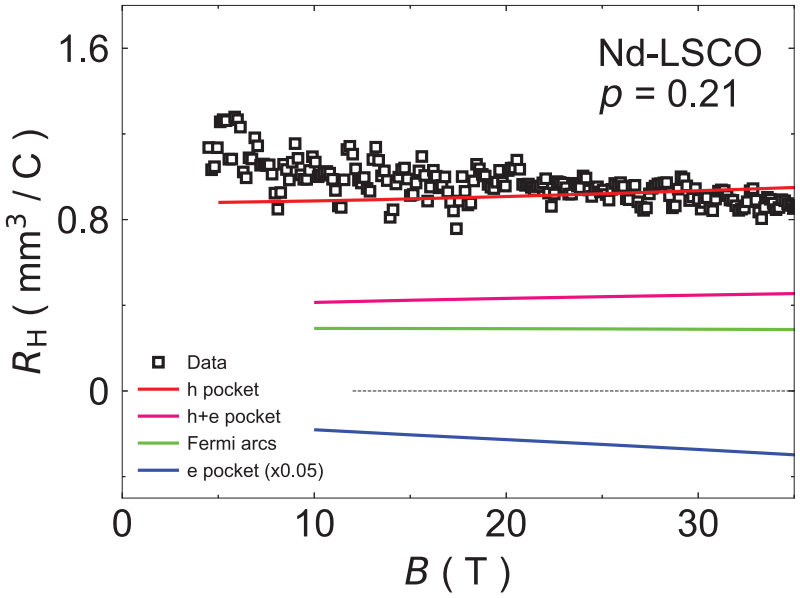

Figure 3.13: The Hall effect in Nd-LSCO at $p = 0.21$. The data is taken at 30 K and is reproduced from [10]. "h pocket" is from the fit to the data shown in Figure 4 of the main text; "h+e pocket" is from a fit that includes both the hole and electron pockets after ($\boldsymbol{\pi}$,$\boldsymbol{\pi}$) reconstruction; "Fermi arcs" is from the fit in Figure 3c and d of the main text; "e pocket" is from just the electron pocket produced by ($\boldsymbol{\pi}$,$\boldsymbol{\pi}$) reconstruction, scaled down by a factor of 20 for clarity.

The tight binding model for the YRZ ansatz is

$$\begin{aligned}\epsilon_{\mathrm{YRZ}}(k_x,k_y,k_z) =& \frac{1}{2}\left(\xi_k+\xi_k^0\right)-\sqrt{\left(\frac{\xi_k+\xi_k^0}{2}\right)+E_g^2(k_x,k_y,k_z)} \\ &-2t_z\cos\left(\frac{k_zc}{2}\right)\cos\left(\frac{k_xa}{2}\right)\cos\left(\frac{k_ya}{2}\right)\left[\cos(k_xa)-\cos(k_ya)\right]^2,\end{aligned} \tag{3.10}$$

where ξ_k, ξ_k^0, and E_g are given by

$$\begin{aligned}\xi_k =& -2t\left[\cos(k_xa)+\cos(k_ya)\right]-4t'\cos(k_xa)\cos(k_ya) \\ &-4t''\left[\cos(2k_xa)+\cos(2k_ya)\right]-\mu\end{aligned} \tag{3.11}$$

$$\xi_k^0 = -2t\left[\cos(2k_xa)+\cos(2k_ya)\right] \tag{3.12}$$

$$E_g = \Delta/2\left[\cos(2k_xa)-\cos(2k_ya)\right]. \tag{3.13}$$

As was the case with the ($\boldsymbol{\pi}$,$\boldsymbol{\pi}$) reconstruction, we select only the nodal hole pockets

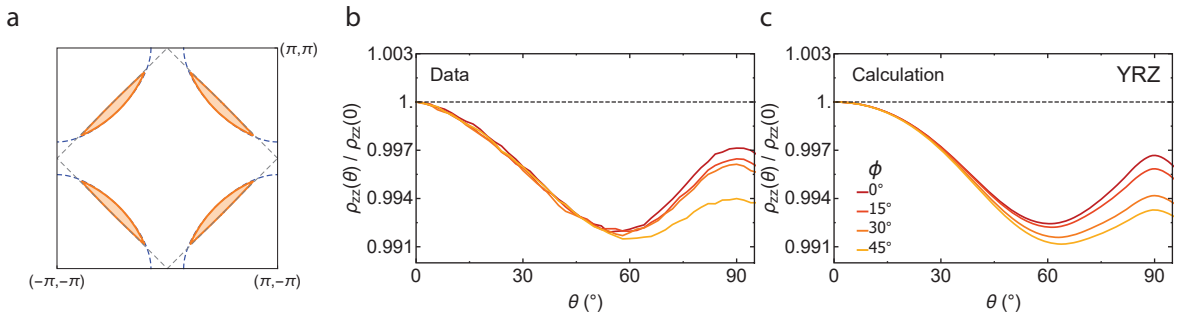

Figure 3.14: (**a**) The nodal hole pockets produced by the YRZ reconstruction. (**b**) The ADMR data for $p = 0.21$, reproduced from Figure 1c in the main text. (**c**) Best-fit of the ADMR using the YRZ model and a constant scattering rate.

because of their consistency with the measured Hall effect, and introduce the interlayer coupling after in-plane reconstruction. The resulting nodal hole pockets are shown in Figure 3.14a, and the best fit is shown in Figure 3.14c. The best fit parameters are an isotropic scattering rate of $1/\tau = 26$ ps^{-1}, $\mu = -0.492t$, $t_z = 0.278t$, and $\Delta = 0.013t$, with the rest of the tight binding parameters taken from Table 3.1. In Figure 3.14 we show that the nodal hole pockets from the YRZ ansatz also fit the ADMR data at $p = 0.21$.

3.5 Discussion

Our main finding is a qualitative change in the ADMR that indicates a transformation of the FS at $p^\star$. For $p > p^\star$, excellent agreement is found between the FS measured by ADMR and the one measured by ARPES, both giving the same large, diamond-like Fermi surface [48]. For $p < p^\star$, however, the ADMR is strikingly different. This difference is not due to a simple lowering of the chemical potential through the van Hove point, nor is it solely due to a change in the scattering rate across $p^\star$: it must therefore be due to a change in the geometry of the FS. The data below $p^\star$ are best described by a FS composed of nodal hole pockets. These nodal hole pockets can result from a $Q = (\pi, \pi)$ reconstruction. Such a

reconstruction is consistent with the transition from a carrier density $n = 1 + p$ at $p > p^\star$ to a density of $n = p$ at $p < p^\star$, as revealed by the Hall coefficient [93, 10] (see Figure 3.13 for a comparison of the measured and calculated Hall coefficients). Similar nodal hole pockets were recently detected by both quantum oscillations and ARPES in the 5-layer cuprate $Ba_2Ca_4Cu_5O_{10}(F,O)_2$ at a doping where long-range AFM order is known to exist [61]; the question is whether a similar reconstruction takes place in Nd-LSCO at $p = 0.21$, given that the spin density wave correlations at this doping are short-ranged and quasistatic [59, 8].

Many proposals that break translational symmetry in the same way as long-range AFM—with a wavevector of $Q = (\pi, \pi)$—have been put forward, including d-density wave order [89], staggered loop-current order [94], and of course local-moment antiferromagnetism or spin-density-wave order [95, 91]. There are also proposals that produce nodal hole pockets without breaking translational symmetry, including the Yang-Zhang-Rice (YRZ) ansatz [90], staggered fluxes [88], and topological order [63]. In Figure 3.14 we show that the nodal hole pockets from the YRZ ansatz also fit the ADMR data at $p = 0.21$. This suggests that the nodal hole pockets themselves, rather than the particular details of any one model, are what is important to describe the Fermi surface transformation across $p^\star$.

Even if no static, long-range order is present in Nd-LSCO at $p = 0.21$, scattering at the AFM wavevector is known to be important to many models of the pseudogap [96, 97, 98], and it may be enough for an order parameter to appear static on time scales of order of the quasiparticle lifetime (≈ 0.1 ps) and over length scales of order of the cyclotron radius (≈ 20 nm at $B = 45$ T) [99]. We note that there is evidence for fluctuating, short-range spin density wave correlations in Nd-LSCO near $p^\star$ [59, 8], and short range magnetic order has been found to onset below $p^\star$ in the related compound $La_{2-x}Sr_xCuO_4$ [60]. It may be that some form of this spin density wave reconstructs the Fermi surface at $p = 0.21$. Note, however that a reduction in the Hall coefficient within the pseudogap phase is universal in the cuprates [100, 10, 101, 102], and that our model of FS transformation produces the

correct Hall coefficient (both above and below $p^\star$), which strongly suggests that the model we propose here for the FS below $p^\star$ itself is universal, whereas the tendency toward spin density wave order varies substantially between different cuprates.

Three families of unconventional superconductors—iron pnictides, organics, and heavy-fermions—share a common phase diagram in which long-range magnetic order is suppressed as a function of doping or pressure. At the critical point, where long-range order is suppressed, the superconducting T_c is typically maximal, the resistivity is most "anomalous" (typically linear in temperature), and the quasiparticle mass is enhanced [103, 104, 56]. Long-range magnetic order reconstructs the Fermi surface in all three classes of materials [105, 103, 106] and thus the onset of Fermi surface transformation, near-optimal T_c, T-linear resistivity, and enhanced quasiparticle interactions are tied together across dozens of superconducting materials, each with entirely different microscopic constituents. The phase diagram of the high-T_c cuprates is superficially similar, with T-linear resistivity, near-optimal T_c, and enhanced effective mass all occurring at a critical doping where the pseudogap phase appears. What was missing until now was direct experimental evidence of the accompanying FS transformation.

CHAPTER 4

QUANTUM TRANSPORT IN 2D MATERIALS USING SURFACE ACOUSTIC WAVE (SAW) RESONATORS

This chapter is adapted from a paper, quantum transport in graphene Using surface acoustic wave resonators, submitted to Nano Letters and posted on Arxiv with Yang Xu, Kaifei Kang, Benyamin Davaji, Kenji Watanabe, Takashi Taniguchi, Amit Lal, Kin Fai Mak, Jie Shan, and B. J. Ramshaw.

Surface acoustic waves (SAWs) provide a contactless method for measuring the wavevector-dependent conductivity. This technique has been used to discover emergent lengthscales in the fractional quantum Hall regime of traditional, semiconductor-based heterostructures. SAWs would appear to be an ideal match for 2D heterostructures but the right combination of substrate and experimental geometry to allow access to the quantum transport regime has not yet been found. Here, we demonstrated that SAW resonant cavities fabricated on $LiNbO_3$ substrates can be used to access the quantum Hall regime of high-mobility, hexagonal boron nitride (hBN) encapsulated graphene heterostructures. Our work establishes SAW resonant cavities as a viable platform for performing contactless conductivity measurements in the quantum transport regime of 2D heterostructures.

4.1 Introduction

Spectroscopic probes of frequency-dependent conductivity are ubiquitous in condensed matter, but analogous techniques for measuring the momentum-dependent conductivity are relatively scarce. The fundamental problem is that photons have wavelengths of millimeters or longer at the energy scales relevant to emergent phenomena in quantum materials—typically a few meV. The length scales of these phenomena, however, such as correlation lengths and periodicities, are typically nanometers to microns.

One solution is to replace light with sound, which has wavelengths 10^5 times shorter than light at comparable frequencies. Sound waves traveling across the surface—surface acoustic waves (SAWs)—of a piezoelectric material create an oscillating electric field at the wavelength of the sound: tens-of-microns to tens-of-nanometers at MHz to GHz frequencies. This oscillating electric field interacts with a conducting material placed in proximity to the SAW, and by measuring the resultant changes in sound velocity and attenuation, one can measure the material's conductance. This technique has several attractive features: it is

contactless, bulk, measures at finite wavelength, and is compatible with low temperatures and high magnetic fields.

SAWs have been used to great effect in GaAs/AlGaAs heterostructures, where the naturally-piezoelectric GaAs substrate generates SAWs that interact with the 2D electron gas. SAWs were used to show that current-induced modification of the bubble and stripe phases is a local phenomenon [107], to measure the periodicity and energy-momentum dispersion of the stripe phase at filling factor 9/2 [108], and to measure the Fermi surface in the composite Fermi liquid at filling factor 1/2 [23].

SAWs would appear to be an ideal technique for two-dimensional (2D) heterostructures, where it can be difficult to make electrical contact and where there are emergent and engineered length scales such as charge density wavelengths [109] and Moire periodicities [110], as well as various theoretical predictions for wavelength-dependent phenomena to be probed with SAWs [24, 25]. While there has been some work incorporating 2D heterostructures and SAWs [111, 112], the quantum transport regime has not been reached.

There are two main challenges: finding a suitable substrate and increasing signal size. First, traditional heterostructure substrates such as silicon are not piezoelectric. Thus a piezoelectric substrate compatible with high-mobility device fabrication and electrostatic gating must be identified. Second, even relatively large 2D heterostructures are two to four orders of magnitude smaller than the 2DEGs used in the aforementioned studies on GaAs/AlGaAs. As the SAW signal is directly proportional to the sample area, standard SAW delay-lines are not sensitive enough for quantum transport experiments on 2D heterostructures.

In this chapter, we focus on the development of SAW resonant cavities on $LiNbO_3$ substrates for contactless conductivity measurements in the quantum transport regime of 2D heterostructures. We first introduce the basic property of SAWs and their interaction with a

2D conducting sample placed near the substrate surface. Then, we compare the two ways of performing SAW measurement, using SAW delay lines and SAW resonators, and show that the resonant cavity geometry increases signal-to-noise ratio by three orders of magnitude over the traditional delay-line geometry. This is followed by a thorough discussion on the design and fabrication of SAW resonators and how we use the finite element method to understand the SAW signal and guide our design of the devices. Finally, we demonstrate that the substrate is compatible with high-mobility device fabrication and electrostatic gating by a detailed analysis of the quantum oscillations in the SAW cavity frequency in the quantum Hall regime of graphene.

4.2 Surface acoustic waves on piezoelectric heterostructures

In this section, we talk about the basic properties of SAW in piezoelectric substrates and their interaction with a 2D conducting sample placed near the substrate surface. The information provided here is based on the reference [113].

Surface acoustic waves are elastic modes that propagates along the surface of elastic medium, which decay exponentially with depth into the material. Thus, the energy flow is concentrated within a distance of the order of a wavelength λ beneath the surface. There are several types of surface acoustic waves, and the Rayleigh wave is the main focus here. Rayleign wave consists of both longitudinal and transverse motion and there is a phase difference between these two component motions, which means that the particle displacement at and beneath the surface is elliptic, leading to an elliptical polarization of the wave. An illustration of particle displacement for Rayleigh wave is shown in Figure 4.1. There would also be a travelling wave of electric potential accompanying the displacement field, and it is not just confined to the piezoelectric surface, but extended above it by a distance on the order of one acoustic wavelength.

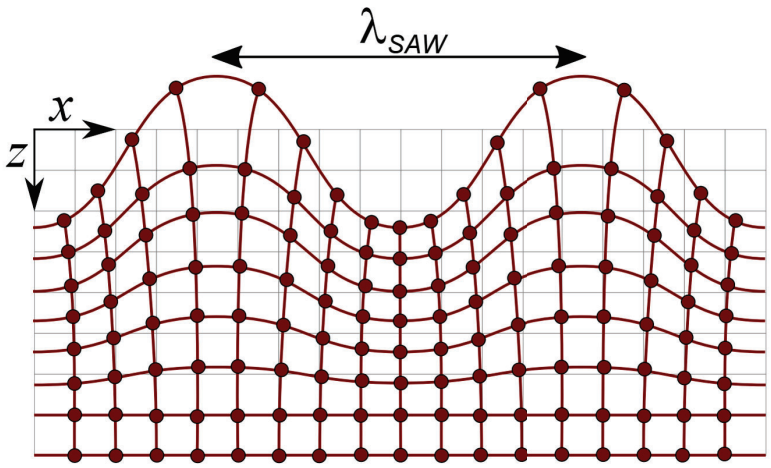

Figure 4.1: An illustration of a Rayleigh wave propagating in the $\hat{x}$ direction. The image is reproduced from [7].

It was shown in the 1960s that, when a piezoelectric material is coupled to a thin layer of conducting material, the SAW velocity shift Δv and the attenuation coefficient Γ satisfy the relation,

$$\frac{\Delta v}{v} - \frac{i\Gamma}{q} = \frac{K_{eff}^2}{2} \frac{1}{1 + i\sigma_{xx}(q,\omega)/\sigma_m} \tag{4.1}$$

where $\sigma_{xx}(q,\omega)$ is the longitudinal sheet conductivity of the nearby material at wave vector q and frequency $\omega = vq$ and K_{eff}^2 is a substrate-specific coupling coefficient. σ_m is the characteristic sheet conductivity of the SAW given by $\sigma_m = v_s(\epsilon + \epsilon_0)$, where ϵ is the permittivity of the piezoelectric substrate and ϵ is the permittivity of the material occupying the space about one SAW wavelength above the substrate surface.

To understand Equation 4.1, we start with the elastic wave equation for the acoustic displacement field in 2D.

$$\begin{aligned} \frac{\partial S}{\partial x} &= \frac{\partial^2 u}{\partial x^2} \\ \frac{\partial T}{\partial x} &= \rho \frac{\partial^2 u}{\partial t^2} \end{aligned} \tag{4.2}$$

where ρ is the mass density, S is the strain and T is the stress. For simplicity, we only consider a one-dimensional model, and the result is only applicable for longitudinal bulk waves. Although these simplifications do not apply to SAW due to the difference in the

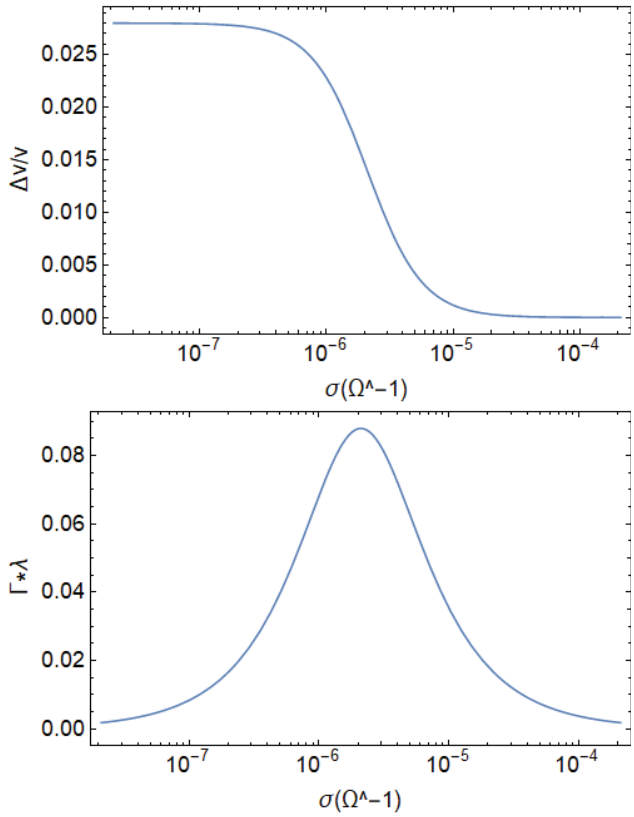

Figure 4.2: Upper: shift in SAW velocity as a function of the conductivity of the thin conducting layer on the top of the SAW device. Lower: SAW attenuation as a function of the conductivity of the thin conducting layer on the top of the SAW device. The two curves are calculated using Equation 4.10 and Equation 4.11, with K^2_{eff} of $LiNbO_3$ to be 5.3% Table 4.1 and $\sigma_m = v(\epsilon_1 + \epsilon_2)$ to be $2.1 * 10^{-6}\Omega^{-1}$, where ϵ_1 is the dielectric constant of $LiNbO_3$ and ϵ_2 is the dielectric constant of vacuum.

boundary condition, it is still a good approximation for understanding the SAW [114]. In a piezoelectric material, the solution of the elastic equation must also satisfy the following relations.

$$\begin{aligned} T &= cS - eE \\ D &= eS + \epsilon E \end{aligned} \tag{4.3}$$

Here c is the stiffness constant, e is the piezoelectric constant and ϵ is the electric permittivity of the material. We can rearrange the equations and obtain a wave equation by eliminating E in Equation 4.3,

$$\rho \frac{\partial^2 u}{\partial t^2} = c(1 + \frac{e^2}{c\epsilon}) \frac{\partial^2 u}{\partial x^2} - \frac{e}{\epsilon} \frac{\partial D}{\partial x}. \tag{4.4}$$

We can discuss two limits based on Equation 4.4 to gain some intuition on how the conductivity affects the sound velocity in a piezoelectric material.

The first limit is when the conductivity of the material approaches infinity. In this limit, the material can be considered a metal with an dielectric constant, ϵ, approaching infinity with the electric field completely screened. The Equation 4.3 would be reduced back to Hooke's law in terms of stress and strain. The sound velocity in this limit would be $v = \sqrt{c/\rho}$.

The second limit is when the conductivity of the material approaches zero (piezoelectric insulator). As there are no charges building up to screen out the electric field, the 1D Poisson's equation requires $\partial D/\partial x = 0$ and Equation 4.4 become

$$\rho \frac{\partial^2 u}{\partial t^2} = c(1 + \frac{e^2}{c\epsilon}) \frac{\partial^2 u}{\partial x^2}. \tag{4.5}$$

The solution to the equation is a plane wave with an increased elastic constant $c' = c(1 + e^2/c\epsilon)$ and the sound velocity is $v' = \sqrt{c'/\rho}$. This increase in elastic constant is called piezoelectric stiffening, and the electromechanical coupling coefficient K^2 is defined in this limit as,

$$K^2 = \frac{e^2}{c\epsilon} \approx \frac{2(v' - v)}{v}. \tag{4.6}$$

K^2_{eff} in Equation 4.1 differs slightly from K^2 obtained from Equation 4.6, since Equation 4.6 is derived for bulk wave, and the boundary condition at the crystal surface needs to be taken into consideration for SAW.

In the intermediate regime, where the conductive electron partially screens the SAW electric field in the bulk piezoelectric material, this partially screening capability depends on the conductivity of the material. When SAWs propagate, the accompanied longitudinal electric field can couple to the mobile carriers in the materials, inducing current and resulting in Ohmic loss. Since the energy is transferred from the SAW, the SAW amplitude would be attenuated. At the same time, the sound velocity changes because of the piezoelectric

stiffening effect. In the case of low conductivity, it takes some time, τ, for the electrons in the material to reach equilibrium when an external electric field is applied. For convenience, the conductivity relaxation frequency, $\omega_r = \sigma/(\epsilon_1 + \epsilon_2)$, which relates to the time τ via $\tau = 2\pi/\omega_r$ is introduced. Here, ϵ_1 and ϵ_2 are the electric constants of the piezoelectric substrate and the half-space above it and σ is the conductivity of the piezoelectric material, respectively. When the SAW frequency is much lower than this relaxation frequency, the electrons in the substrate are able to redistribute fast enough to screen the electric field, and the material behaves similarly to the piezoelectric material in the first limit. When the SAW is much higher than this relaxation frequency, the electrons fail to follow the oscillating electric field, leaving the electric field unscreened, and the material behaves similar to the piezoelectric material in the second limit. When the two frequencies are similar, $\omega_r \approx \omega$, maximum attenuation occurs. This frequency dependence of sound attenuation and change of SAW velocity for a homogeneous piezoelectric material are [115]

$$\Gamma = \frac{\omega}{v}\frac{K_{eff}^2}{2}\frac{\omega_r/\omega}{1+(\omega_r/\omega)^2} \tag{4.7}$$

and

$$\frac{\Delta v}{v} = \frac{K_{eff}^2}{2}\frac{1}{1+(\omega_r/\omega)^2}. \tag{4.8}$$

However, instead of a homogeneous piezoelectric conductor, We are interested in the case where a thin sheet of conducting material is placed on the surface of a piezoelectric insulator, with a conductivity, σ, where the thickness of the conducting material, d, is much smaller than the wavelength of the SAW, λ. In this case, although Equation 4.7 and Equation 4.8 are still applicable, some modifications need to be made because now the longitudinal electric field of the SAW can only be screened by the conducting material at the surface, instead of being screened by the bulk of the piezoelectric material. Because SAWs concentrate near the surface and exponentially decay depth into the bulk, the induced current is carried near the surface of the piezoelectric material with a depth of around a wavelength. In the surface conducting sheet case, the induced current is only carried inside the conducting sheet. Thus,

the surface conducting sheet case can be understood as equivalent to a bulk case with effective conductivity scaled by some factor of $k * d$ [116], where $k = 2\pi/\lambda$ is the wave vector of the SAW and d is the thickness of the conducting material. Hence, the conductivity relaxation frequency now becomes

$$\omega_r = \frac{\sigma dk}{\epsilon_1 + \epsilon_2} = \frac{\sigma_{xx} k}{\epsilon_1 + \epsilon_2}, \tag{4.9}$$

where $\sigma_{xx} = \sigma d$ is the longitudinal sheet conductivity. With this modification of ω_r, now Equation 4.7 and Equation 4.8 become

$$\Gamma = k \frac{K_{eff}^2}{2} \frac{\sigma_{xx}/\sigma_m}{1 + (\sigma_{xx}/\sigma_m)^2} \tag{4.10}$$

and

$$\frac{\Delta v}{v} = \frac{K_{eff}^2}{2} \frac{1}{1 + (\sigma_{xx}/\sigma_m)^2}, \tag{4.11}$$

where $\sigma_m = v(\epsilon_1 + \epsilon_2)$, which is equivalent to Equation 4.1.

4.3 Experimental setup and measurement technique

In this section, first, we compare the two ways of performing SAW measurement, using SAW delay lines and resonant cavities, and show that by replacing the traditional delay line geometry with the resonant cavity geometry, the signal-to-noise ratio can be increased by two orders of magnitude. Then, we present several useful techniques for the characterization and measurement of the SAW resonant cavities.

4.3.1 Experimental setup: delay lines and resonant cavities

In a piezoelectric material, surface acoustic waves can be electrically generated and converted back to an electrical signal using interdigital transducers (IDT) Figure 4.3. The transducers consist of a sequence of metal electrodes, usually aluminum or gold, alternately connected

Material	**Crystal cut**	**SAW direction**	$K^2_{eff}(\%)$	$v_{SAW}(m/s)$
h-SiC	$< 0001 >$	$1\bar{1}00$	0.0111	6832
h-ZnO	$< 0001 >$	$1\bar{1}00$	1.12	2691
$LiNbO_3$	$128° - Y$	X	5.3	3992

Table 4.1: K^2_{eff} and SAW propagation velocity, v_{SAW}, of some commonly used piezoelectric materials.[7]

to two bus bars. The periodicity of the metal electrodes determines the wavelength of the SAW generated by the IDT. The electrode width is usually a quarter of the center-frequency wavelength, and the minimum possible width, determined by the fabrication technique, limits the obtainable frequency [117]. The frequency of the SAW can be determined by $f = v_{SAW}/\lambda_{SAW}$.

A typical surface-acoustic wave device, a SAW delay line, is shown in Figure 4.3. When a voltage is applied between the two sets of metal strips in IDT1, a periodic and oscillating electric field is generated, and due to the piezoelectric effect, elastic stress is set up. At the output, IDT2 acts reciprocally, converting incident elastic waves back to electrical signals. The energy conversion efficiency mainly depends on the electromechanical coupling coefficient of the piezoelectric material, K^2_{eff}. We are interested in using SAW to measure the conductivity change of the sample placed near the surface of the piezoelectric substrate, and from Equation 4.1, the SAW velocity and attenuation change as a function of the sample conductivity is directly proportional to K^2_{eff}. The ideal piezoelectric substrate for our measurement needs to have a high K^2_{eff}. Table 4.1 summarizes the value of K^2_{eff} and v_{SAW} of the commonly used piezoelectric material. Among the commonly used piezoelectric material listed, as $LiNbO_3$ has the highest K^2_{eff}, we choose it as our piezoelectric substrate material.

There are two predominant methods for generating SAWs: delay lines and resonant cavities. Most SAW experiments on GaAs/AlGaAs heterostructures use the delay-line geometry, where a pulse of sound generated by one interdigital transducer (IDT) and captured by another. Resonant cavities use the same pair of IDTs but build up a standing wave between

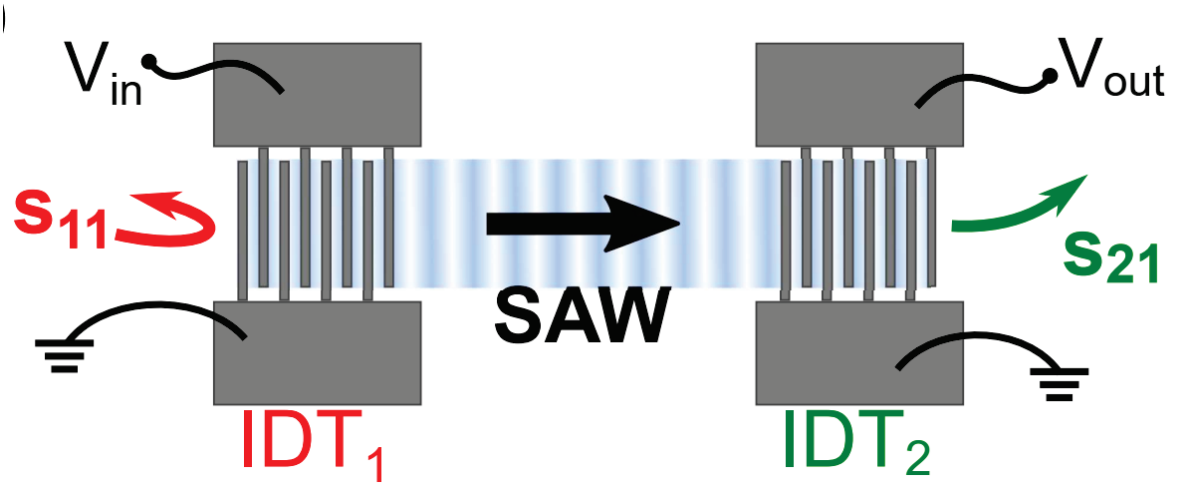

Figure 4.3: A schematic of SAW delay line, consists of two interdigital transducers(IDTs) patterned on a piezoelectric substrate.This figure is reproduced from [7].

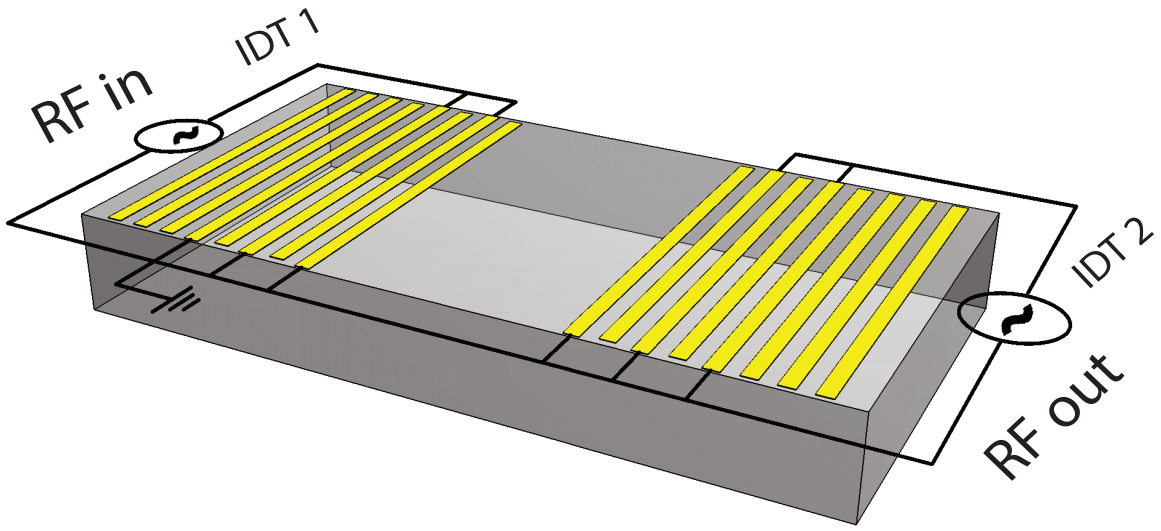

Figure 4.4: A schematic of a SAW resonator, consisting of two IDTs for launching and detecting the SAW and two sets of reflectors for traping the acoustic energy inside the cavity.

them aided by reflectors that constrain the acoustic energy inside the cavity (see Figure 4.4). The signal is then effectively amplified by the quality factor (Q) of the cavity, which is higher than 10^3 in the cavities we use. This suggests that the resonant cavity geometry may produce significantly better signal to noise than the delay line geometry for small samples. This argument in favour of cavities can be quantified by examining how the phase changes for sound traveling across a delay line and for sound in the resonant cavity.

SAW delay lines

For a delay line [118], changes in sound velocity ($\delta v/v$) translate to changes in the phase ($\delta\phi/360°$) of the SAW as

$$\frac{\delta\phi}{360°} = \frac{A_s}{\lambda \cdot W}\frac{\delta v}{v}, \tag{4.12}$$

where $A_s = L_s \cdot W$ is the 'active' area in the delay line where the velocity change occurs (e.g. the area of the 2DEG), L_s is the length of the active area, W is the width of the delay line (perpendicular to the direction of propagation), and λ is the wavelength of the SAW.

SAW resonant cavities

Unlike the delay-line geometry, the relation between the amount of phase shift measured near its resonant frequency, the shift in resonant frequency, $\delta f_0/f_0$, and the change in sound velocity $\delta v/v$ is not immediately apparent for a resonant cavity. When the shift in resonant frequency is large compared to the width of the resonance, it can be accurately tracked using the phase-locked loop technique.

However, when the shift in resonant frequency is small, by measuring phase shift and amplitude at a fixed frequency near its resonant frequency with a lockin amplifier, we can take advantage of a longer averaging time and achieve a better signal-to-noise ratio. This amplitude and phase change as the cavity properties change (e.g. as a function of magnetic field or gate voltage). These changes can be converted to changes in the cavity linewidth Γ and resonant frequency f_0 by considering the cavity as a driven harmonic oscillator.

The amplitude A and phase ϕ as a function of drive frequency f across a resonance have a Lorentzian lineshape (Figure 4.5),

$$A(f) = \frac{A_0 f_0/\Gamma}{\sqrt{(f_0^2 - f^2)^2 + (\Gamma f)^2}} \tag{4.13}$$

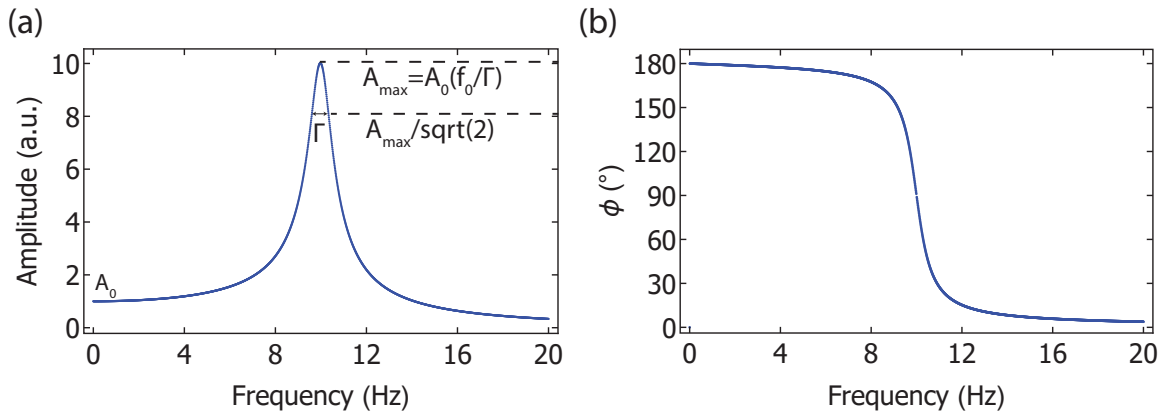

Figure 4.5: (a) Amplitude A as a function of frequency f across a resonance, given by Equation 4.13. (b) Phase ϕ as a function of frequency f across a resonance, given by Equation 4.14.

and

$$\phi = arctan(\frac{\Gamma f}{f^2 - f_0^2}). \tag{4.14}$$

The shifts in resonator frequency we observe in our experiments as a function of magnetic field are all small compared to the resonance frequency itself (of order 1 part in 10^5). In this limit (i.e. to first order in drive frequency f), when the resonator is driven near resonance, the amplitude is independent of drive frequency and the phase changes linearly with drive frequency. The amplitude is given by

$$A \propto \frac{f_0}{\Gamma} \tag{4.15}$$

and the phase (in radians) is given by

$$\phi \approx \frac{\pi}{2} - \frac{f^2 - f_0^2}{f\Gamma}. \tag{4.16}$$

These expressions can be used to derive the changes in amplitude and phase when the cavity frequency and linewidth shift:

$$\frac{\delta A}{A} = \frac{\delta f_0}{f_0} - \frac{\delta \Gamma}{\Gamma} \tag{4.17}$$

and

$$\delta\phi \approx \frac{(f_0 + \delta f_0)^2 - f_0^2}{f_0\Gamma} \approx \frac{2\delta f_0}{\Gamma} = 2Q\frac{\delta f_0}{f_0}, \tag{4.18}$$

where $Q = f_0/\Gamma$ is the quality factor of the cavity and $\delta\phi$ is given in radian. Equation 4.17 and Equation 4.18 can then be used to convert the measured amplitude and phase changes into changes in the cavity resonance frequency and linewidth. Assuming the cavity has a fixed length and the sample covers the entire cavity area, in a 1D case, $\delta f_0/f_0$ would equal $\delta v/v$. In reality, as the sample area is small compared to the cavity area, we need to scale Equation 4.18 to calculate the measured phase shift by A_s/A_c. Now, we have derived that for a resonant cavity with quality factor Q near its resonant frequency, the phase shift is given by

$$\frac{\delta\phi}{360^\circ} = \frac{Q}{\pi}\frac{A_s}{A_c}\frac{\delta v}{v}, \tag{4.19}$$

where ϕ is now in degrees and A_s and A_c are the sample and cavity areas, respectively.

In the limit that the shift in resonant frequency is small, to compare the measured phase shift in both the delay line and resonant cavity, it is convenient to define the 'gain' G as the cavity phase shift divided by the delay line phase shift. We obtain

$$G = \frac{Q}{\pi}\frac{\lambda}{L}, \tag{4.20}$$

where L is the length of the cavity or delay line. Equation 4.20 suggests that, for a given $\delta v/v$ intrinsic to the sample, large phase shifts can be achieved with high quality factor cavities that have a small number of wavelengths between the IDTs. We use $\lambda = 20$ μm SAW cavities with an IDT separation of 100 μm—these lengthscales are easily achieved with standard photolithography and leave enough space to fabricate a heterostructure in the center of the cavity. These cavities regular achieve Qs between 1000 and 5000, producing a gain of up to 2000, i.e. the phase shift of the SAW if same device was operated in delay-line mode would be 300 time smaller than in cavity mode.

4.3.2 Measurement techniques

There are several ways to characterize and measure the two-port SAW resonators. Here, we briefly discuss some of the measurement setups we used, including laser Doppler vibrometry measurements, pulsed echo measurement, and phase measurements with a lock-in amplifier at a fixed frequency. Here, we will not describe the actual setup of all the techniques. Instead, we will introduce what they measure and how they are useful in the characterization and the measurement.

Laser Doppler vibrometry

The laser doppler vibrometer is an instrument that uses the Doppler effect to measure vibrations. The basic idea is that when the laser light hits a moving surface, the frequency of the reflected light changes. This frequency shift, δf, is proportional to the out-of-plane velocity of the moving object, v, and can be described by $\delta f = 2 * v/\lambda$, where λ is the wavelength of the laser light. This frequency shift is then accurately measured with a laser interferometer and then converted back to the velocity of the moving object. The out-of-plane component of the displacement can also be measured with the LDV by measuring the intensity change of the reflected light [119]. The vibration mode shape can be visualized by repeating the measurement at various points across the vibrating surface and performing interpolation. Thus, the laser doppler vibrometry measurements are particularly useful in the analysis of the mode shape of the SAW resonator. The laser doppler vibrometer used for calibrating our devices is a Polytec UHF-120 ultra high frequency vibrometer.

In our SAW experiment, knowing the mode shape of the SAW resonator is highly beneficial in three ways. First, other unwanted acoustic waves are launched together with the Rayleigh waves when driving and detecting the sound wave with the IDT, including other types of SAWs and bulk waves. These acoustic waves could also give rise to a resonant

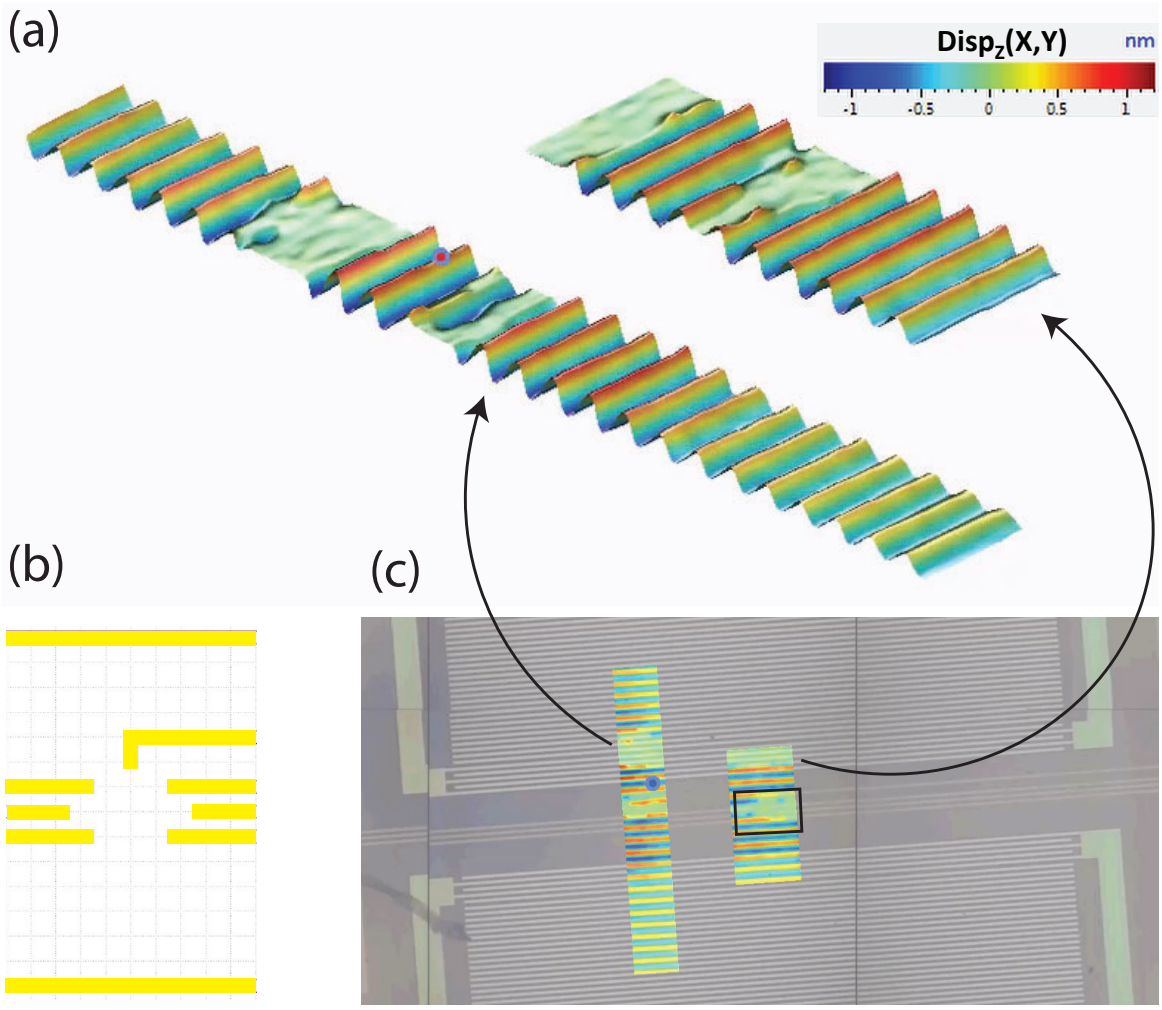

Figure 4.6: (a) The mode shape of a SAW resonator measured with the laser Doppler vibrometer at around 187.5 MHz with a drive voltage of 5 V. This SAW resonator has a similar frequency response shown in Figure 4.13a. The mode shapes are reconstructed from measurements of a 2D array of spatial points, with the spacing between each point being around 2 μm. (b) The design of the contact electrodes. It is a zoomed-in view of the area inside the black box in (c). (c) An optical image of the cavity. The corresponding position of the mode shape shown in (a) is indicated by the arrows.

peak in the frequency response, leading to a confusing signal. Visualizing the mode shape helps confirm that the resonance in the frequency response is indeed Rayleigh waves which interact with the sample following the theory described in section 4.2. Second, in some of our designs of the SAW resonators, complicated contact electrodes need to be placed in the middle of the cavity to perform transport measurements on the 2D heterostructure samples

simultaneously. Near the sample area, these contact electrodes can not be approximated by an object with translational symmetry along the direction parallel to the substrate surface and perpendicular to the SAW propagation direction and thus can not be modeled using just the 2D COMSOL model described in section 4.5. LDV measurement helps in understanding how these contact electrodes perturb the cavity. Third, in our measurement, the sample size is comparable to the wavelength of the SAW. As only the longitudinal components of the piezo-electric field interact with the conducting electrons in the sample, and the longitudinal components only dominate near the node in a standing wave pattern, knowing the mode shape at the sample area is essential to quantifying the effective area of the measurement.

Figure 4.6 shows an example of the laser Doppler vibrometry measurement on one of our SAW resonators. The frequency response of this SAW resonator is similar to the one shown in Figure 4.13a. The laser Doppler vibrometry measurement is performed at around 187.5 MHz near the peak of the first resonant mode. The mode shape confirms that at this frequency, the resonance comes from the eigenmode of the Rayleigh wave, and as expected, near the center of the cavity, the SAW oscillation is disturbed by the contact electrodes, leading to a reduction in the standing wave amplitude. This result shows we should avoid placing our sample near those regions for a better signal.

Lock-in amplifier

section 4.3.1 shows that the phase measured at a fixed frequency near the resonant frequency can be directly converted back to the shift in sound velocity via Equation 4.19. Phase measurement at a fixed frequency can be easily achieved with a commercial lock-in amplifier if the lock-in amplifier can operate up to the operation frequency of the SAW resonator. In our measurement, the SAW resonator operates at around 195 MHz, and we can directly use the Zurich Instrument UHF lock-in amplifier, which can operate up to 600 MHz, for the measurement.

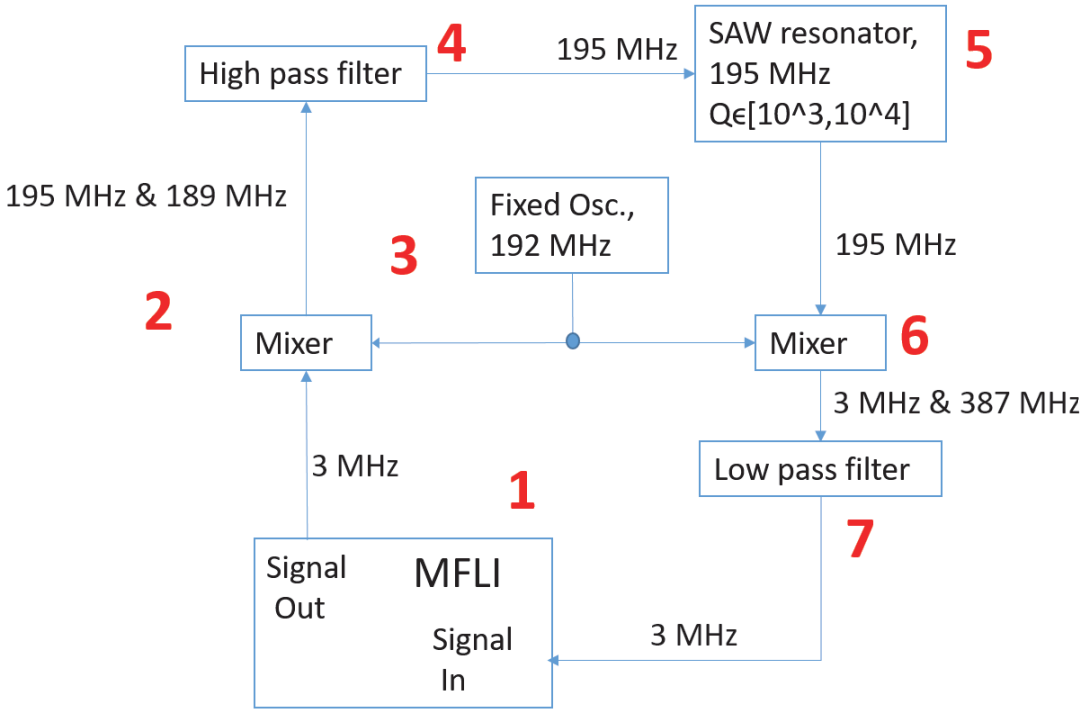

Figure 4.7: The MFLI outputs a signal at around 3 MHz(1) and mixed up with part of output from the external frequency source at 196 MHz (2), with the low frequency component filtered (4). The 195 MHz component is used to drive the SAW resonator and the output from the SAW resonator is then mixed down with part of the output from the external frequency source at 196 MHz (6), with the high frequency component filtered (7). Finally, the 3 MHz component is measured by the MFLI.

For SAW resonators with shorter wavelengths and higher operational frequency beyond 600 MHz, the measurement can no longer be done simply using the UHF lock-in amplifier. Before purchasing the Zurich Instrument UHF lock-in amplifier, we only have the Zurich Instrument MFLI lock-in amplifier, which can only operate up to 5 MHz and can not be directly used. To perform the phase measurement at 195 MHz, we use an external frequency source and two stages of frequency mixing. The detail of the circuit is shown in Figure 4.7. A similar circuit can be built based on this circuit to measure the SAW resonator that operates at a higher frequency beyond 600 MHz.

4.4 Two-port SAW resonator design and fabrication

The type of SAW resonance cavities we use in this study is a two-port Fabry-Perot SAW resonator. It consists of two IDTs for excitation and detection of the SAW and two Bragg mirrors that sit behind the IDTs. A schematic of the basic two-port SAW resonator is shown in Figure 4.4.

4.4.1 Two-port SAW resonator design

In this subsection, we talk about some basic ideas in the design of high-quality SAW resonator. The information provided here is based on reference[120].

The Bragg mirror is made up of periodically distributed reflectors because, unlike bulk waves, which can be effectively reflected from polished surfaces, it has been shown that SAWs can not be efficiently reflected from a single surface [121]. There are several ways to make effective reflectors, including bare metal stripes, shorted metal stripes, dielectric material stripes, and grooves. For the simplicity of fabrication, we use gold metal strips as our reflectors. Similar to the transmission line model for microwave modeling, part of the SAW energy reflects at acoustic impedance discontinuities. The reflected wave from increasing or decreasing impedance steps has a different phase shift by 180 °. Thus if the distance between the increasing and the decreasing impedance steps is a quarter of a wavelength ($1/4\lambda$), the reflected waves will be in phase and add up constructively, so usually, in the design of the Bragg mirrors, the width of the reflector strips and their spacing is a quarter of a wavelength. The acoustic impedance is given by

$$Z_{ac} = (\rho v)^{1/2} \tag{4.21}$$

where Z_{ac} is the acoustic impedance and ρ is the density of the material and v is the surface wave velocity.

To achieve highly effective reflectors, we want to maximize the impedance mismatch ΔZ near the edge of the reflectors. In the case of deposited metal as reflectors, there are mainly three sources of impedance mismatch. The first is the mass loading effect, which change the Z_{ac} by changing the density near the surface of the material and could be maximized using thick films of high-density metal like gold. Having the mass loading effect dominate has the advantage of better control over the acoustic impedance ΔZ, as the thickness of the film can be easily controlled, and the density of the metal is usually well-known. For simplicity and performance, in our first design of the SAW resonant cavity, we used 300 nm of gold, where the thickness is limited by the fabrication, as our reflector material.

The second effect is the electric field shorting effect under the strip. The third effect is the electric field shorting effect between the strips, where the reflective properties are affected by shorting the strips together or connecting external impedance between strips. Naively, these effects can be understood using Equation 4.11 and Equation 4.21. From section 4.2, we have derived that placing a conducting material near the surface of the piezoelectric substrate, the partial screening of the conducting electron leads to a shift in SAW velocity, which is directly proportional to the coupling constant K^2_{eff} of the substrate. Thus, near the metal reflectors' edge, the SAW velocity mismatch also contributes to the impedance mismatch ΔZ, and the effect is most pronounced in substrates with a high K^2_{eff} like $LiNbO_3$. However, in the actual devices, the acoustic impedance discontinuity also depends on how the metal strips are connected. For example, the unconnected metal strips can also regenerate acoustic waves, as the voltage picked up by the adjacent strips have opposite voltages. However, when the metal strips are shorted together, this regeneration effect is reduced. Moreover, because the reflection spreads over several wavelengths, the ways the metal strips are connected modify the boundary condition of the reflection. In our second design of SAW resonance cavities, to reduce the fabrication step, we use 50 nm of gold for both the reflectors and the contact electrodes and short the gold reflector to compensate for the reduced mass loading effect.

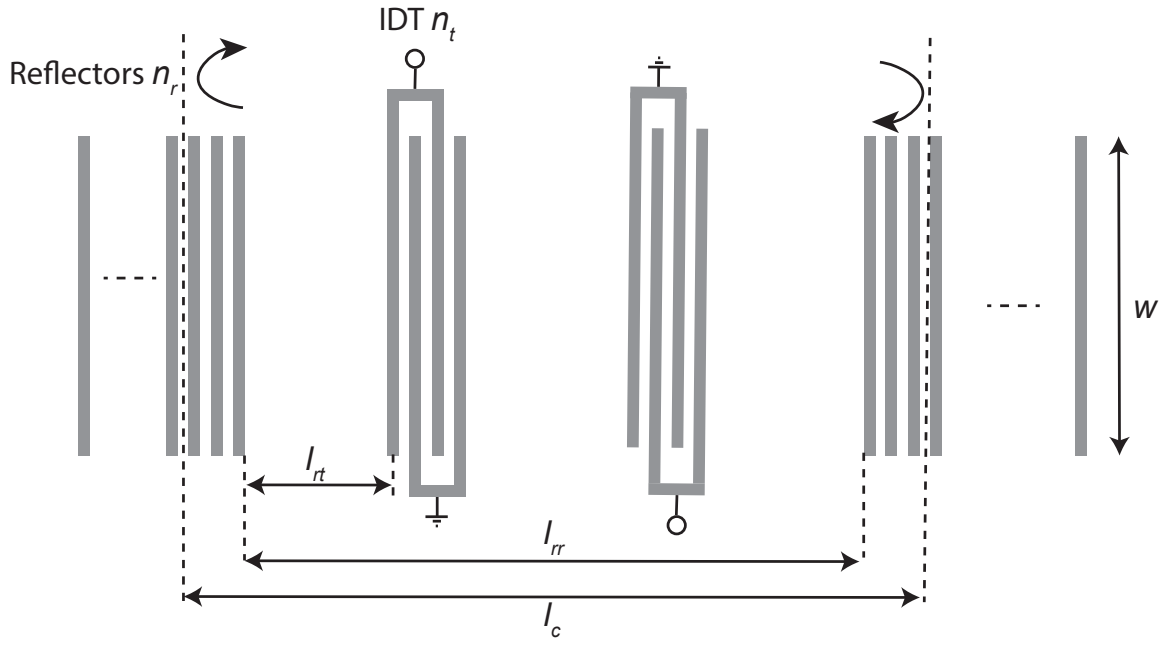

Figure 4.8: (a) A typical design of a two-port SAW resonator with the critical parameters in the design labelled. l_{rr} is the length between the front of the two Bragg mirrors, l_c is the effective cavity length, l_{rt} is the distance between the front of the Bragg mirror and the center of the last metal finger of the IDT, W is the width of the cavity, n_r is the number of reflectors in each Bragg mirror, and n_t is the number of metal fingers in each IDT.

Some of the most important parameters in the design are shown in Figure 4.8. The first parameter we considered in our design is l_{rt}, the distance between the IDT and the reflectors. It is an essential parameter because when two IDTs are placed between the Bragg mirrors, they introduce additional reflections, which may cause distortions in the resonator frequency response, depending on l_{rt}. When the IDT is placed at a maximum of the standing wave pattern, achieving maximum coupling, the IDT's reflection will be 90 degrees out of phase with respect to the component reflected by the reflectors, distorting the frequency response of the resonator. When the IDT is placed at about $\lambda/8$ off a standing wave maximum, although the coupling between the SAW and the IDT is not maximized, the IDTs can be viewed as part of the reflectors, thus not distorting the signal. Another import parameter we considered is l_{rr}, the distance between the two Bragg mirrors. The frequency response of the two IDTs without the Bragg mirrors can be viewed as a bandpass filter. Ideally, we

want to have the resonant frequency determined by the reflectors to coincide with the center of the pass band by fine-tuning l_{rr}.

Strategies to find the optimized l_{rr} and l_{rt} for two-port SAW resonators has been discussed before [120]. However, in our experiment, we introduce extra metal stripes at the center of the cavity as contact electrodes, and the simple strategies may not work. To find the optimum l_{rr} and l_{rt} for the design, we use a full resonator model in COMSOL to study the frequency response of resonators with different combinations of l_{rr} and l_{rt} (details in Appendix B). We select the combinations that show resonance with a high Q and then design and fabricate the resonators with those parameters.

4.4.2 SAW resonator fabrication

We fabricated our surface acoustic wave (SAW) cavities on 128° Y-Cut, SAW-grade, black $LiNbO_3$ wafers from Precision Micro-Optics Inc. The resonator used for Device 1 (D1, Figure 2a in the main text) was fabricated in two steps. First, the electrical contacts for the gate electrodes were patterned with standard photolithography. A 15 nm titanium adhesion layer and a 15 nm gold layer were then deposited with a CVC E-gun evaporator SC4500 followed by a liftoff process. Second, the IDTs and reflectors are made with a similar process but with thicker gold—300 nm—to provide strong confinement of the SAWs [120].

Device 2 (D2) was fabricated in a single step using 50 nm thick gold reflectors and electrodes. The electrodes were electrically shorted together to provide stronger confinement with the thinner gold.

4.5 Finite element method (FEM) simulations using COMSOL

To improve the design of two-port SAW resonators to achieve better quality factors and to understand the effect of a conducting gate in 2D heterostructures in SAW measurement, we perform finite element simulations using COMSOL. The FEM simulations are performed using the Structural Mechanics Module of COMSOL Multiphysics. Full 3D modeling of the SAW resonator is prohibitively time consuming because of the combination of the relatively large lengthscale of the cavity and reflectors with the relatively short lengthscale of the SAW itself. Fortunately, the resonator itself is largely 1D, with a second dimension required to describe the SAW. Assuming translational symmetry along the third direction allows for fast simulations without compromising much in terms of accuracy.

We have developed two models, a unite cell model and a full resonator model, and constantly cross-checking between models to ensure simulation accuracy.

4.5.1 Unit cell model

We start with the simplest model to understand the propagation of SAWs in the substrate material $LiNbO_3$. The elastic properties of $LiNbO_3$ are highly anisotropic; thus, to obtain accurate simulation results, the first step is to have the correct orientation of the material setup. The first model we test is a 2D unit cell model with just the substrate material. To simulate our substrate material, 128° Y-cut $LiNbO_3$ with SAW propagate along the x-axis, we use the material properties of $LiNbO_3$ in the COMSOL material library and rotate the material around the x-axis by 2.23 rad so that the x-axis of the model align with the x-axis of the crystal and the y-axis of the model is 128° with respect to the y-axis of the crystal. We study the eigenfrequency of the model shown in Figure 4.9a, with λ to be 20 μm. The fundamental SAW mode is shown in Figure 4.9b. From the mode shape, it can be seen that

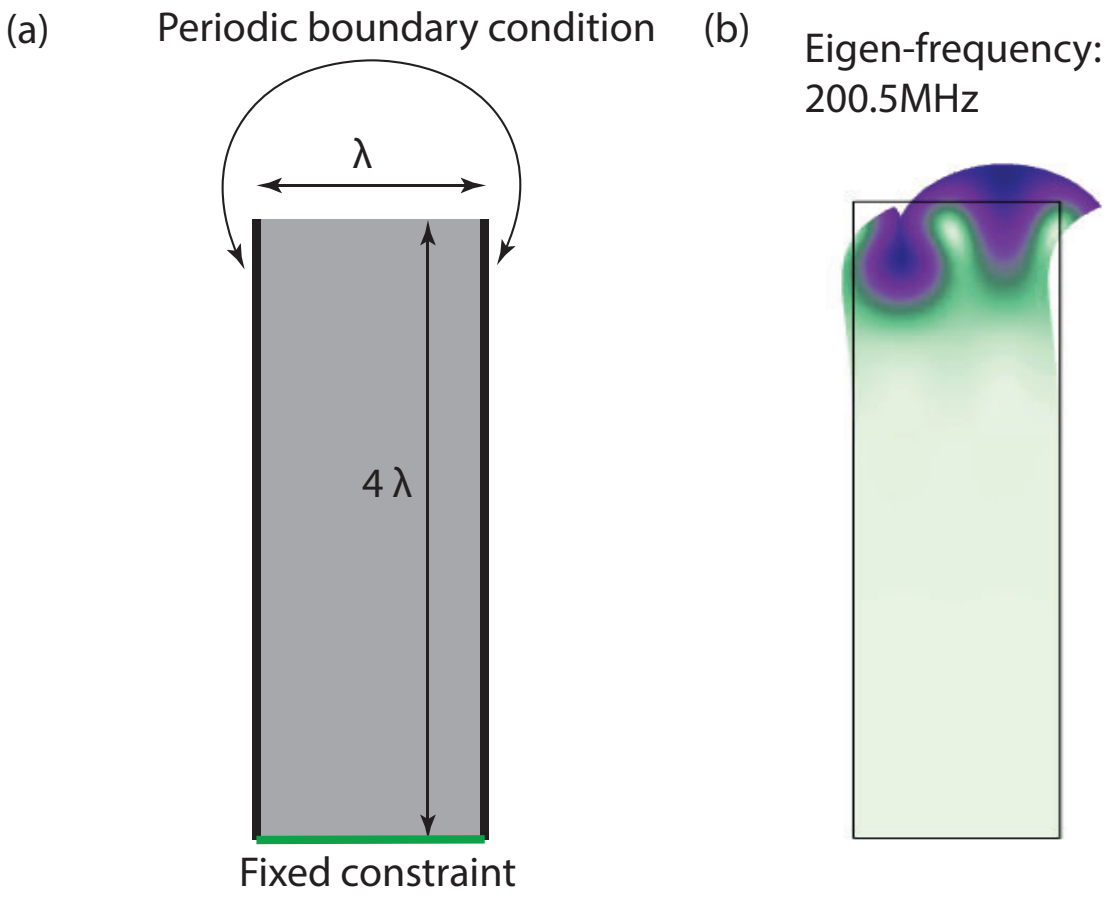

Figure 4.9: (a)The unit cell model used for understanding the SAW properties of the 128° Y-cut $LiNbO_3$ substrate. The model boundaries with different constrained in the eigenfrequency study are marked in different colors. Periodic boundary conditions are imposed on the two boundaries marked in black, a fixed constraint is imposed on the boundary mark in green, and a free boundary condition is set on the top surface of the model. (b) The mode shape of the SAW eigenmode. The eigenfrequency is 200.5 MHz. The color represents the displacement.

the wavelength of the SAW equals λ, and the sound velocity can be calculated using $v = \lambda f$, where f is the eigenfrequency of the SAW mode. In our COMSOL unit cell model, $\lambda = 20$ μm and the eigenfrequency of the SAW mode, $f = 200.5$ MHz. The calculated SAW velocity is 4010 m/s, which agrees with the reported SAW velocity of 128° Y-cut $LiNbO_3$ with SAW propagates along the x-axis is around 4000 m/s.

The next step is to understand the interaction between a conducting material placed near the surface of the substrate and the SAW. To study this interaction, we modify our

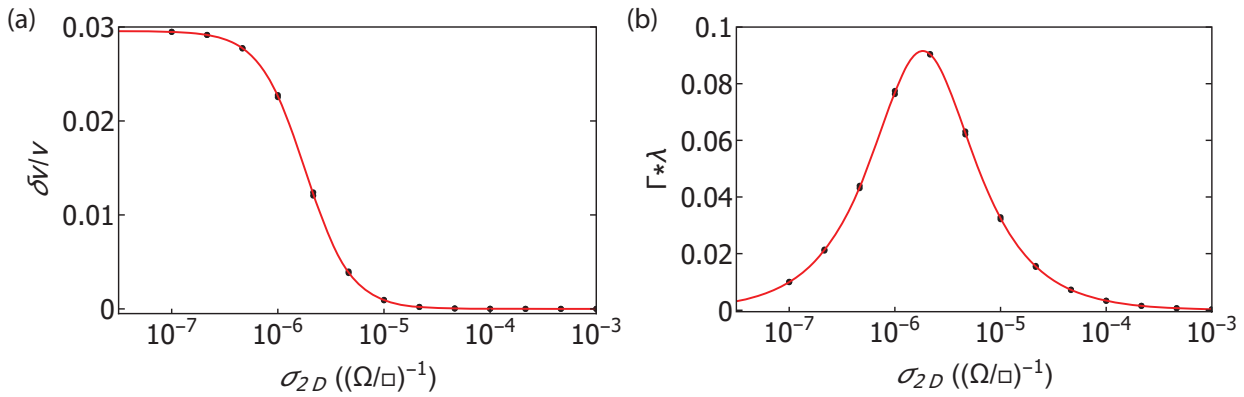

Figure 4.10: The black dots are the simulation result converted from the eigenfrequency and the red lines are fit with Equation 4.11 and Equation 4.10. (a) $\delta v/v$ as a function of the sheet conductivity of the conducting sample. From the fit, K^2_{eff} equals 0.059 and σ_m equals $1.81 \times 10^{-6}\Omega^{-1}$. (b) $\Gamma\lambda$ as a function of the sheet conductivity of the conducting sample.From the fit, K^2_{eff} equals 0.058 and σ_m equals $1.83 * 10^{-6}\Omega^{-1}$.

model by placing a conducting material on top of the substrate. In the simulation, we set the conducting material to be a linear elastic material and model the conductivity by introducing an imaginary component, $-i\sigma/(2\pi f_0 \epsilon_0)$, to the relative permittivity of the material, where σ is the conductivity of the material, f_0 is the frequency of interest and ϵ_0 is the vacuum electric permittivity. After introducing the conducting material into the model, the result returns an eigenfrequency with an imaginary component. The imaginary component of the eigenfrequency indicates dissipation. We repeat the eigenfrequency study with different conductivity of the material and observe that both the real and imaginary parts of the eigenfrequency of the SAW mode shift as a function of the conductivity. The relative shift of the real and imaginary part of the eigenfrequency can be converted back to the shift in SAW velocity and attenuation via $\delta v/v = \delta f_r/f_r$ and $\Gamma k = f_i/f_r$, where f_r is the real part of the eigenfrequency and f_i is the imaginary part of the eigenfrequency. The result is shown in Figure 4.10 and we fit the $\delta v/v$ and Γk with Equation 4.11 and Equation 4.10 with K^2_{eff} and σ_m as fit parameters. We obtain K^2_{eff} to be 0.058 and σ_m to be around $1.8 \times 10^{-6}\Omega^{-1}$, which agree well with the calculation shown in Table 4.1 and Figure 4.2.

The two simple unit cell models both agree well with the reported value for the substrate

and the analytical expression (Table 4.1 and Figure 4.2), and we are confident about the setup of our unit cell model. Our final goal of the unit cell model is to simulate the effect of a conducting gate when the sample is a 2D heterostructure. The challenge of this model is that the boundary condition for this case is complicated. Neither any analytical solution nor quantitative experimental study on this problem is available. Therefore, it is essential to check the model setup with the previous two simple models. Because graphite is the most commonly used gate material in high-quality 2D heterostructures, we use graphite as our gate material in the simulation. To perform the simulation, we replace the simple conductive material in the last model with the actual experimental device, including hBN, sample, and graphite gate (Figure 4.11a). Because of this model's huge disparity in length scales, simulating an atomically-thin 2D sample is unfeasible. However, on the length scale of the electric fields produced by the SAW (i.e., 20 μm), it is sufficient to set the sample to a manageable thickness (5 nm) and to fix the total conductance to the correct, experimentally determined value later.

We set the conductivity of the graphite top gate to 3×10^7 S/m [122], vary the conductance of the 2D sample, and repeat the eigenfrequency study. The result is shown in Figure 4.11. We can still fit the $\delta v/v$ and Γ from the simulation with Equation 4.11 and Equation 4.10. The effective K^2_{eff} obtained from this model is about six times smaller than the K^2_{eff} from the previous model without the gate. This reduction in K^2_{eff} means that with the same change in sample conductivity, the measured signal $\delta v/v$ is largely reduced if a highly conductive gate material is used. This reduction in SAW signal in gated heterostructures has been shown qualitatively in the SAW experiment on GaAs/AlGaAs 2DEGs system in the quantum hall regime [113]. Our simulation provides a quantitative way to perform the conversion between the change in measured SAW velocity $\delta v/v$ and attenuation Γ and the change in sample conductivity.

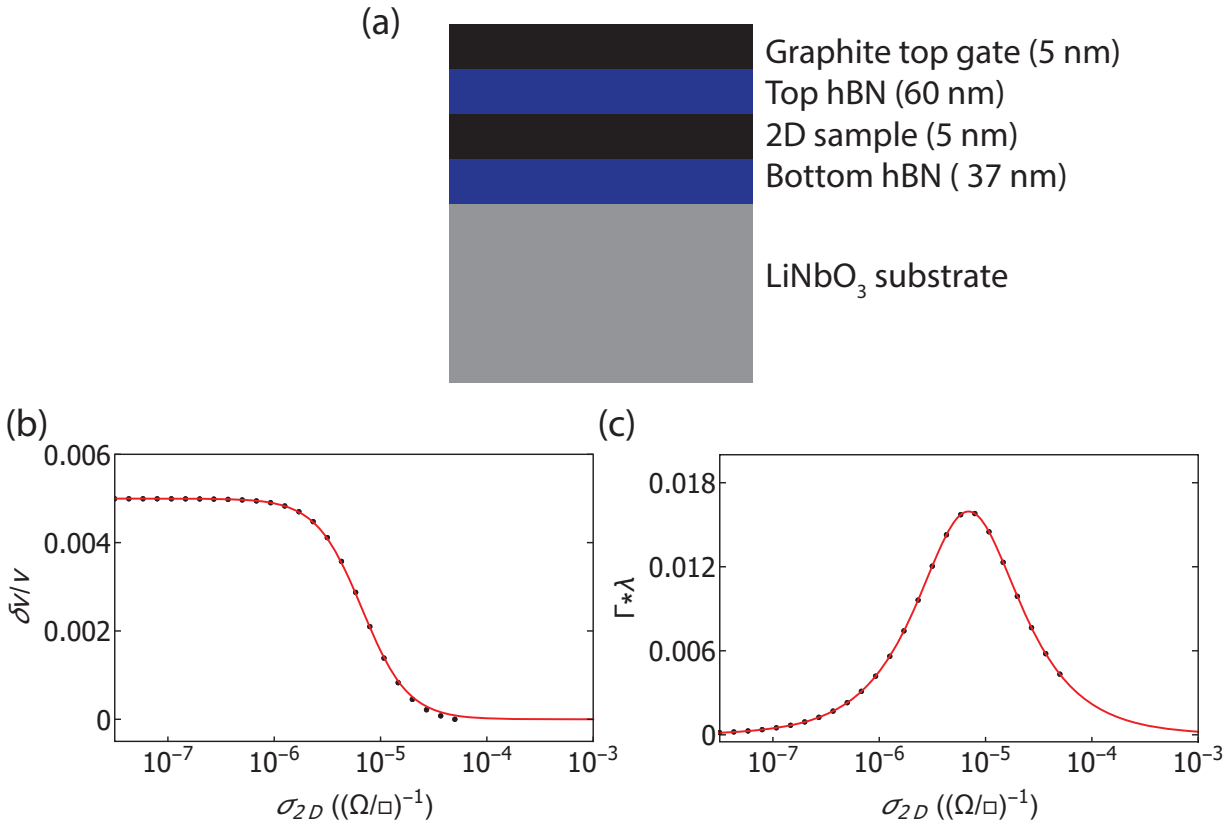

Figure 4.11: (a) An illustration of the actual device structures used in the COMSOL simulation. (b-c)The black dots are the simulation result converted from the eigenfrequency and the red lines are fit with Equation 4.11 and Equation 4.10. (b) $\delta v/v$ as a function of the sheet conductivity of the conducting sample. From the fit, K^2_{eff} equals 0.01 and σ_m equals $6.7 \times 10^{-6}\Omega^{-1}$. (c) $\Gamma\lambda$ as a function of the sheet conductivity of the conducting sample.From the fit, K^2_{eff} equals 0.01 and σ_m equals $6.9 \times 10^{-6}\Omega^{-1}$.

4.5.2 Full resonator model

With the unit cell model, we can perform the conversion between the SAW velocity $\delta v/v$ and attenuation Γ and the change in sample conductivity. However, we also want to directly convert the measured phase shift to the change in sample conductivity. We can achieve this with a full resonator model. Moreover, Equation 4.19 shows that the phase signal in the measurement is proportional to the quality factor of the resonant cavities. In the design of the two-port SAW resonators, there are several critical parameters that have a substantial impact on the quality factor of the device. To fabricate and test all the combinations of these

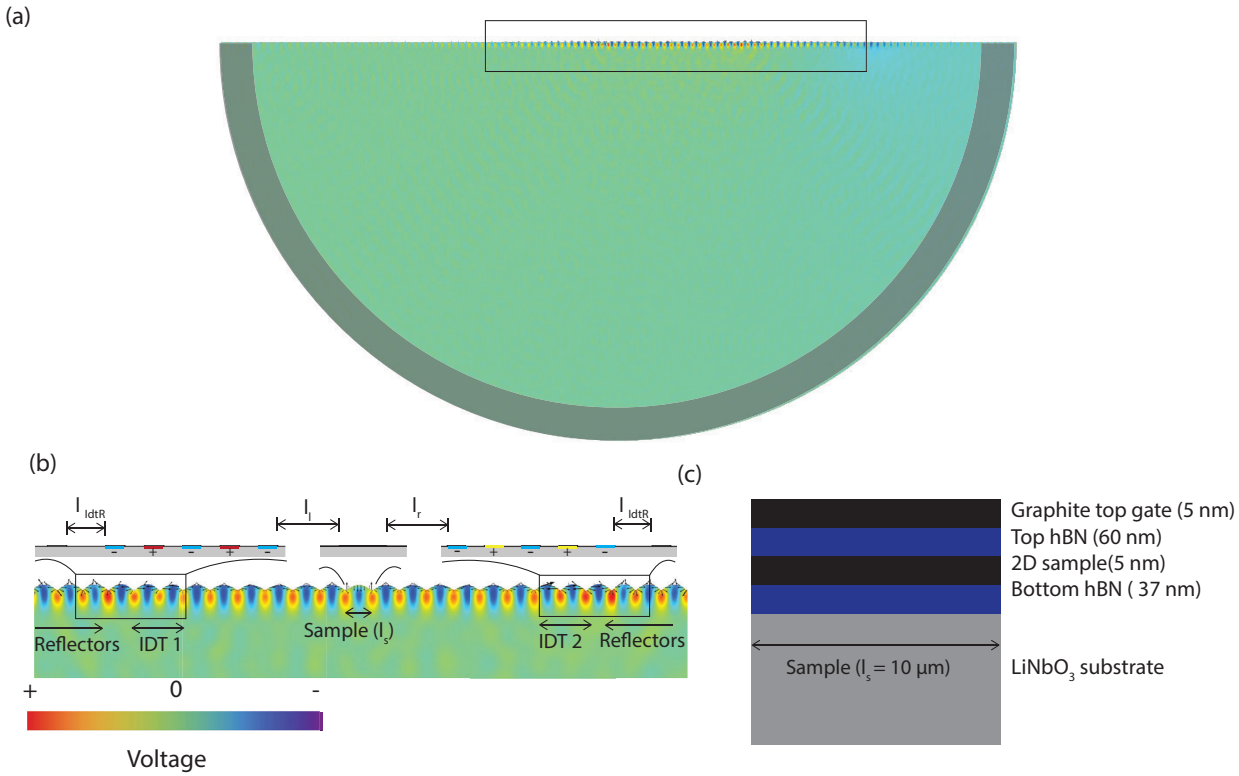

Figure 4.12: (a) The full model used for the SAW resonator simulation, with the perfectly matched layer shown in grey. The simulation is performed in the frequency domain with a one-volt drive. IDT1 is used as the drive IDT, and IDT2 is used as the receive IDT. IDT1 is positioned at the center of the semi-circle. (b) The zoom-in view of the area enclosed by the black box in (a). The IDT electrodes are marked with colored lines. The electrodes marked in blue are grounded, a floating potential boundary condition is imposed on those marked in yellow, and a one-volt drive boundary condition is imposed on those marked in red. (c) An illustration of the actual device structures used in the COMSOL simulation.

parameters is time and money-consuming. We can pre-screen most of these combinations of the parameters with accurate COMSOL modeling of the full resonator and only focus on the promising ones in the fabrication to achieve resonator devices with a high-quality factor.

The model we used for simulation of the full resonator device is shown in Figure 4.12. To keep the model small while avoiding reflections from the boundaries, we use a semicircular geometry with the drive IDTs placed at the center and a perfectly matched, low-reflectivity boundary at the edge of the semicircle. The IDTs and the metallic strips are made up of 300 nm of gold and have a width of $1/4\lambda$. The substrate used in the simulation is 128° Y-cut

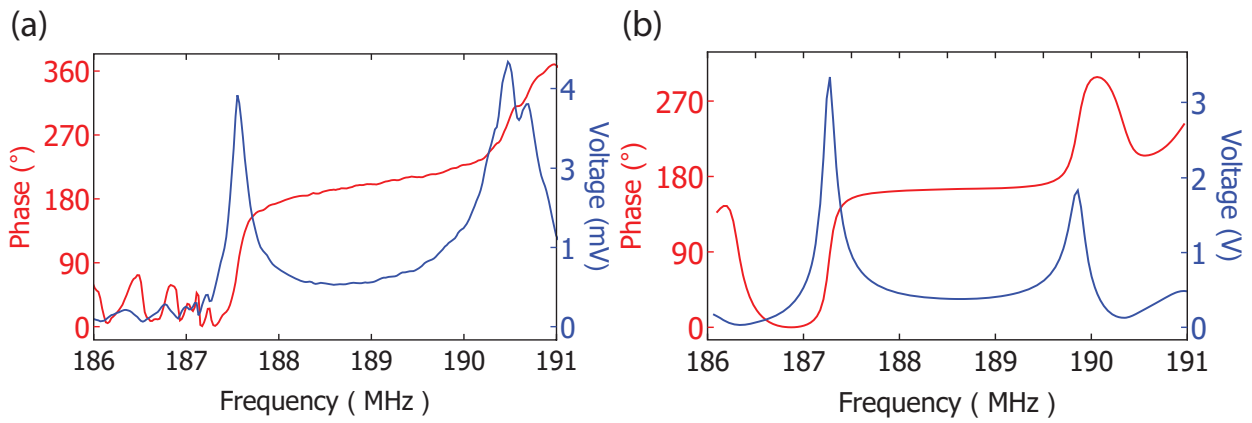

Figure 4.13: (a) The measured amplitude and phase of a fabricated SAW resonator device with the same design as the COMSOL model used in (b). (b) The amplitude and phase of the signal measured at IDT2 as a function of the drive frequency of the 2D full resonator model in Figure 4.12a.

$LiNbO_3$, with the crystalline x-axis parallel to the direction of wave propagation.

A comparison between the frequency response of an actual SAW device and the frequency response of a COMSOL model with the same design is shown in Figure 4.13. The simulation correctly predicts the resonant frequency of the cavity as well as the corresponding quality factor of each resonance. The slight disagreement in the resonant frequency could come from that in this COMSOL model, the conductivity of gold and the 15 nm of titanium adhesion layer in the actual device are not considered. The introduction of the conductivity of gold into the model takes a much longer time for the COMSOL solver to calculate with the same model.

The good agreement between the simulation and measurement shows that we can indeed use the result from the COMSOL simulation to predict the performance of SAW resonators with different design parameters. Using the simulation result, we can improve our design and obtain high-quality SAW resonators, even with complicated contact electrode patterns inside the cavity. Some of the simulation result of SAW resonators with different l_{rr} and l_{rt} are shown in Appendix B.

4.6 Quantum transport in Graphene

To test whether our SAW resonator substrate is compatible with high-mobility device fabrication and electrostatic gating, we study magnetotransport of the hexagonal boron nitride (hBN)-encapsulated graphene heterostructures to calibrate our SAW resonant cavities technique.

4.6.1 Device

Figure 4.14a shows a schematic of the two-port, Fabry-Perot SAW resonators used in this study. These resonators consist of two IDTs for excitation and detection of the SAW and two Bragg mirrors placed behind the IDTs. The Bragg mirrors are made of a regular array of metallic strips and form the Fabry-Perot acoustic cavity where we place the sample [123]. 2D heterostructures typically require gate and ground electrodes, as well as possible transport electrodes if desired, which we fabricated from thinner metal than the Bragg mirrors to maintain a high cavity Q and to allow room for heterostructure fabrication.

Several devices, D0, D1 and D2, were used in this study. Each device consists of a SAW resonator and a graphene heterostructue. We fabricated our resonators on commercially-available, 128° Y-Cut, SAW-grade, black $LiNbO_3$ wafers from Precision Micro-Optics Inc. D0 and D1 used 15 nm gold electrodes and 300 nm, electrically-isolated gold reflectors, where the mass of the gold loads the resonator surface and confines the SAWs. To reduce the number of lithographic steps needed, D2 used electrodes and electrically-shorted reflectors that were both 50 nm thick. Electrically shorting the reflectors improves their reflectance and allows for the use of thinner gold. More details of the resonator fabrication are given in subsection 4.4.2.

Gate-tunable graphene devices were fabricated in the $LiNbO_3$ resonators using a layer-

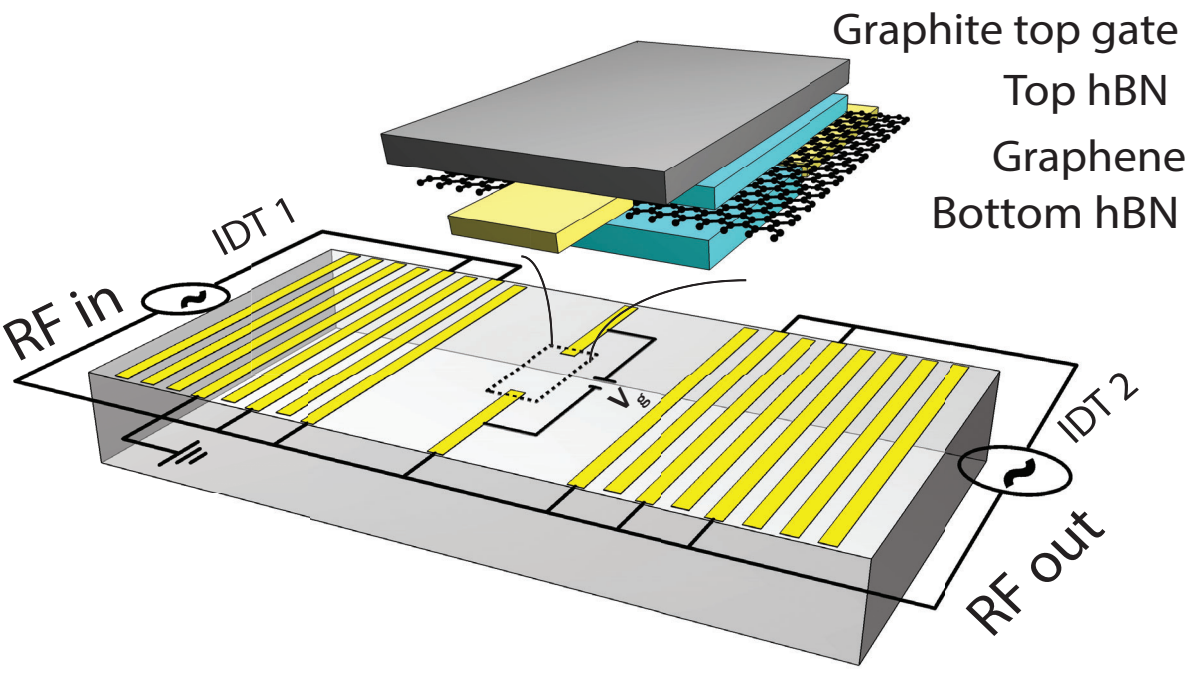

Figure 4.14: **Combining 2D materials with surface acoustic waves.** (a) Schematic of a SAW resonator driven by radiofrequency (RF) pulses across the interdigital transducers (IDTs). A 2D heterostructure is placed in the center of the cavity with gate electrodes.

by-layer, dry-transfer method [124]. The graphene and hexagonal boron nitride (hBN) flakes are first exfoliated from bulk graphite crystals onto silicon substrates and suitable flakes are identified using an optical microscope under ambient conditions. We use a polycarbonate (PC) stamp to pick up a few-layer graphite flake, an hBN flake, a graphene flake, and another hBN flake layer-by-layer. The few-layer graphite flake and the first hBN flake serve as the gate electrodes and the gate dielectrics. The PC stamp is then heated to 180°C to release the stack onto the SAW resonator. Finally, the device is immersed in chloroform for 30 minutes to remove any residue of the PC film.

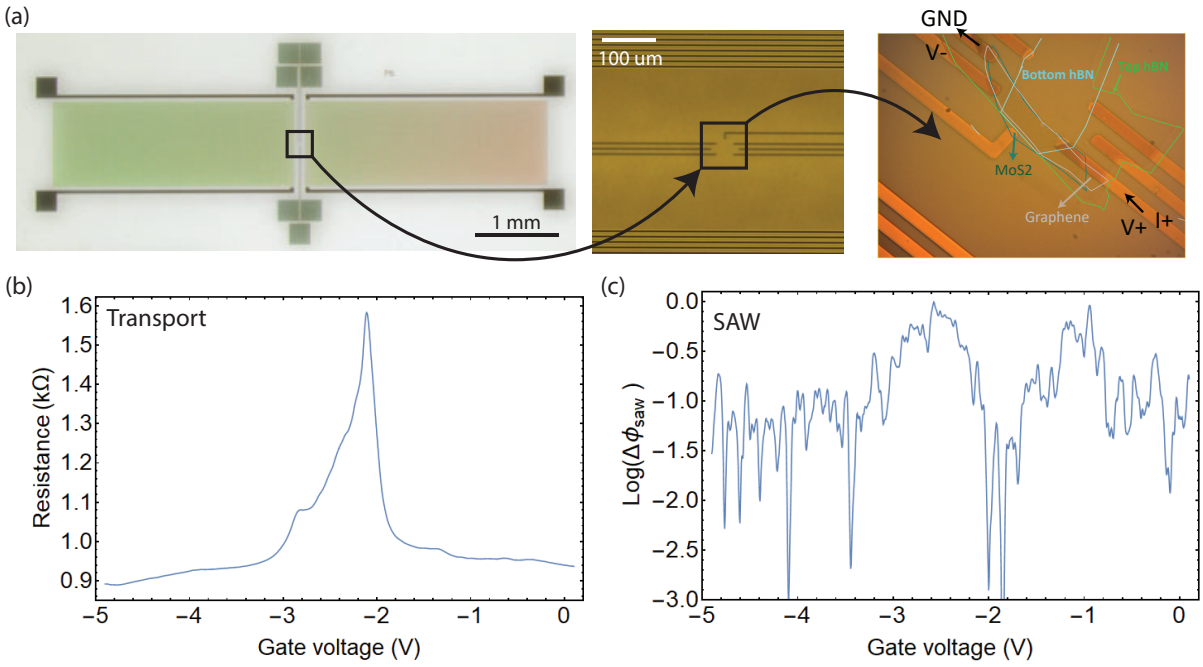

Figure 4.15: **Optical images and characteristics at zero field of D0.** (a) Optical microscope image of device D0. The left image shows a zoomed-out view of the full SAW resonator cavity. The image in the middle shows a zoomed-in view of the center of the cavity with the detail of the pre-patterned gold electrodes without the graphene sample. The image on the right shows the graphene device in detail. Gray-colored lines mark the monolayer graphene area, and dark-green-colored lines mark the MoS_2 top gate area. The graphene sample is only contacted with three gold electrodes, the transport measurement configuration is also labeled. (b) Measured graphene resistance as a function of gate voltage measured at 10 K. The peak feature is related to the CNP of the graphene sample. (c) The phase of the transmitted voltage through SAW resonant cavity D0, as a function of gate voltage, measured at 10 K. The phase shift is proportional to the change in 2D conductivity (see Figure 4.2 and Equation 4.19). However, no obvious peak features in the phase could be identified.

4.6.2 Experiment and Results

We tested several devices with different SAW resonator designs and gate materials. Here, we present results from three devices, D0, D1, and D2. D0 and D1 use the same resonator design. D0 uses MoS_2 as gate material, while D1 and D2 use graphite as gate materials.

Device D0

In subsection 4.5.1, the unit cell COMSOL simulation shows that the amount of SAW signal is reduced by almost an order of magnitude if a highly conducting gate material is used, with the same amount of conductivity change. As a result, in our first design, instead of the commonly used gate material, graphite, we use an indirect bandgap semi-conductor MoS_2, which is less conductive than graphite. However, when we measured our very first device (before D0), we saw complicated SAW signal as a function of magnetic field but not as a function of gate voltages. As this device did not have extra contacts for transport measurement, it is very difficult to identify whether the problem is with the sample or the measurement technique.

To better understand the measurement, we designed our second device with a MoS_2 gate, D0. Figure 4.15a shows an optical image of D0, and it can be seen that the graphene piece makes contact with three gold electrodes, allowing transport measurements. With this design, it is now possible to measure the resistance of the sample and the SAW phase shift as a function of gate voltage simultaneously. When we first cooled down the sample and performed a gate voltage sweep, we did not see any change in the resistance or the SAW phase shift, indicating a sample problem instead of a SAW technique problem. It turns out that the gate did not work because MoS_2 is an indirect bandgap semiconductor, and probably due to coupling to the substrate, it is doped to the point of being insulating, and therefore does not make electrical contact with the gate electrode.

To quickly fix the gate, we add a small graphite piece on top of the MoS_2. The result with the gate fixed is shown in Figure 4.15bc. This time, as a function of gate voltage sweep at zero magnetic fields, we can see a sharp peak in resistivity centered at around -2.2 V, a signature of the CNP, indicating that the gate is working. The broad peak features near the CNP are indications of sample inhomogeneity. With Figure 4.2 and Equation 4.19, the

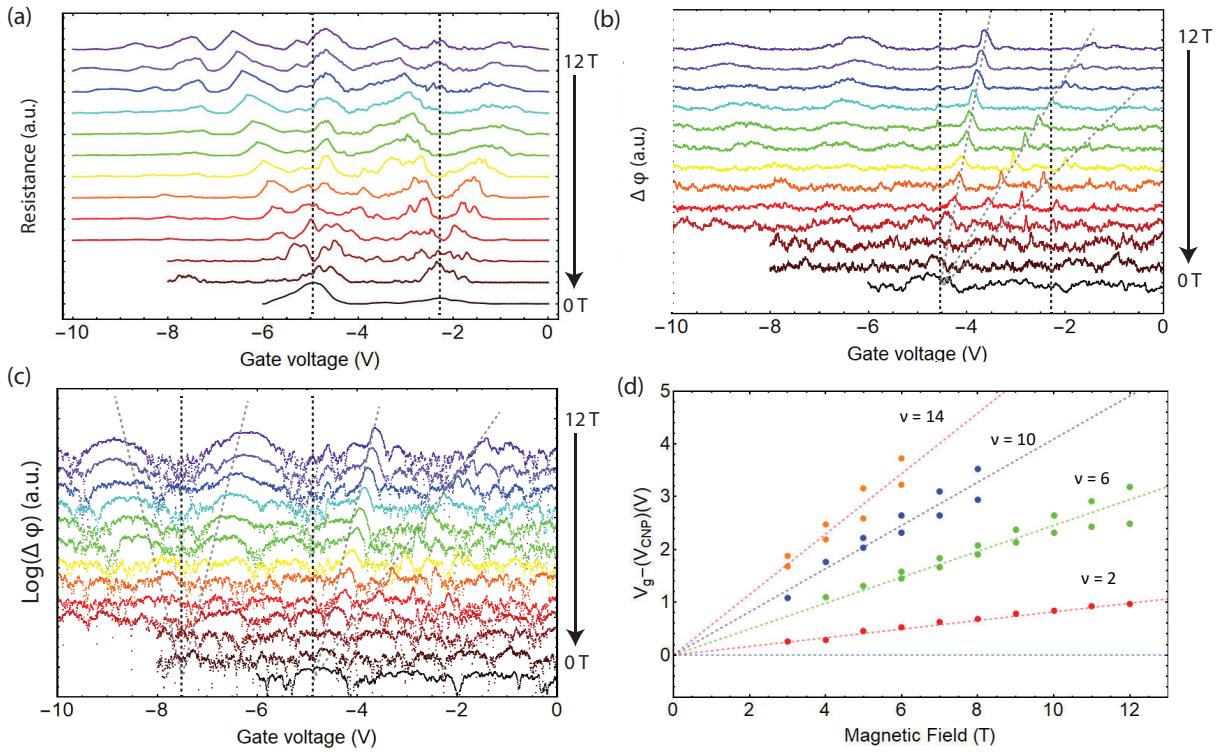

Figure 4.16: **Quantum transport signature in D0.** (a) Normalized resistance as a function of gate voltage from 0 to 12 T, measured at 10 K. The two dashed lines indicate the signatures of two CNPs in the sample. (b) Normalized phase as a function of gate voltage from 0 to 12 T, measured at 10 K. The two vertical dashed lines are placed at the gate voltages where the CNPs are seen in (a). Only the Landau levels associated with the CNP at around $V_g = -5$ V can be observed in the phase. (c) Normalized logarithm of the phase as a function of the gate voltage. Another set of Landau levels associated with the CNP at around $V_g = 7.5$ V can be observed. (a-c) Data measured at different fields are offset for clarity. (d) The gate voltage at the center of the peak features shown in (c) as a function of magnetic fields. The dash lines are $V_g - V_{CNP} = \nu e^2 d/(h\epsilon_{BN}\epsilon_0) \times B$, where V_g is the gate voltage, V_{CNP} is the gate voltage of the CNP (-5 V), ν is the filling factor, ϵ_{BN} is the dielectric constant of hBN, d is the thickness of the top hBN. This equation comes from $\nu = \frac{nh}{eB}$ and $\frac{ne}{V_g - V_{CNP}} = \frac{\epsilon_{BN}\epsilon_0}{d}$, where n is the electron density in the graphene. The points lie on top of the dashed line with ν to be 2, 6, 10, and 14, which is the quantum Hall sequence of graphene.

SAW phase is proportional to 2D resistance, and thus it is expected to see a peak in the phase where there is a peak in the sample resistance. However, no similar peak feature can be identified in the SAW phase shift.

Figure 4.16 shows both the resistance and the SAW phase shift as a function of gate

voltages from 0 T to 12 T. Signatures of Landau levels can be observed in both resistance and in the SAW phase shift. Two CNP can be clearly seen in the resistance measurement, while one CNP at $V_g = -5V$ can be seen in the SAW measurement. This different result between resistance measurement and SAW measurement could come from the fact that the resistance measurement is usually affected by current paths in inhomogeneous samples, while SAW measurement probe the bulk of the sample. We analyze the peak features in Figure 4.16c, by plotting the gate voltage at the center of the peaks as a function of the magnetic field. The result is shown in Figure 4.16b. We found that those peak features' magnetic field dependence follows the Landau levels' behavior in graphene, indicating that the quantum transport regime is reached with the SAW technique.

Although we can see indications of quantum oscillation with D0, the sample is very inhomogeneous, which could be a result of the MoS_2 gate and the extra transport contacts. As we have already seen indications of quantum oscillations in D0, which has a piece of graphite on top of the sample, we are confident that although with a graphite gate, the signal size may be reduced, it might still be large enough that we can observe the quantum oscillation in graphene in the SAW measurement. To improve the sample homogeneity, we use a graphite gate instead of the MoS_2 gate and get rid of the extra transport contact in D1.

Device D1

Figure 4.17a shows the frequency and phase response of D1. IDT1 was driven at 10 mV with a Zurich Instrument UHF lockin amplifier with both the graphene and the graphite gate grounded. The signal from IDT2 was filtered with a ZX75BP-204 band pass filter from Mini-Circuits, amplified with a AM-1571 amplifier from MITEQ, and measured with the lockin. Two resonances, labeled f_1 and f_2, near 190 MHz are each accompanied by a phase shift of approximately 180 °. Each resonance corresponds to a different integer number of

wavelengths in the cavity; $f_1 - f_2 = 3$ MHz is equal to surface wave velocity 3980 m/s divided by twice the effective cavity length of 660 μm (note that multiple reflections set the boundary conditions of the cavity, making the effective length much longer than the physical length of 240 μm). The two peaks near f_2 may be the result of additional reflection from gate electrodes in the middle of the cavity. The quality factor of the resonance at f_1 is 1500: we use this resonance for our measurements.

Figure 4.17b shows the change in cavity phase at the f_1 resonance as a function of magnetic field. Traces at two different gate voltages are shown, both taken at 1.7 K. Shubnikov-de Haas oscillations are clearly observed down to approximately 0.6 tesla, illustrating both the sensitivity of the technique and the quality of the sample. To determine the carrier densities and quantum lifetimes, we perform a standard Lifshitz-Kosevich analysis of the oscillation data following the procedure described in section 2.3.

To obtain the carrier densities, we first subtract a linear background from the data shown in Figure 4.17 of the main text to obtain the oscillatory component. We then perform a fast Fourier transform on the background-subtracted data, the result of which is shown in Figure 4.18. The primary quantum oscillation frequencies F obtained are 17 T and 32 T at $V_g = -5$ V and $V_g = 0$ V, respectively. The quantum oscillation frequency F is related to the Fermi surface area A_F through the Onsager relation $A_k = (2\pi/\hbar)F$. The Fermi surface area can be translated to a 2D carrier density through $n_{2\mathrm{D}} = A_k/A_{BZ} \times 2^2/A_{uc} = 2^2 \times A_k/(2\pi)^2$, where A_{BZ} is the Brillouin zone area, A_{uc} is the unit cell are in real space, and the factor of 2^2 accounts for spin and valley degeneracy. This gives $n_{2\mathrm{D}} = 1.6 \times 10^{12}$ cm^{-2} and $n_{2\mathrm{D}} = 3.1 \times 10^{12}$ cm^{-2} , at $V_g = -5$ V and $V_g = 0$ V, respectively.

To obtain the quantum lifetime, we first obtain the effective mass using $m^\star = \frac{\hbar}{v_F} k_F$ with $k_F = \sqrt{A_k/\pi}$, to be 0.03 m_0 and 0.04 m_0, for $V_g = -5$ V and $V_g = 0$ V respectively. From Figure 4.18, it can be seen that strong higher harmonics can be observed. For simplicity, we only focus on the oscillatory signal at the primary frequency. The oscillatory signal at

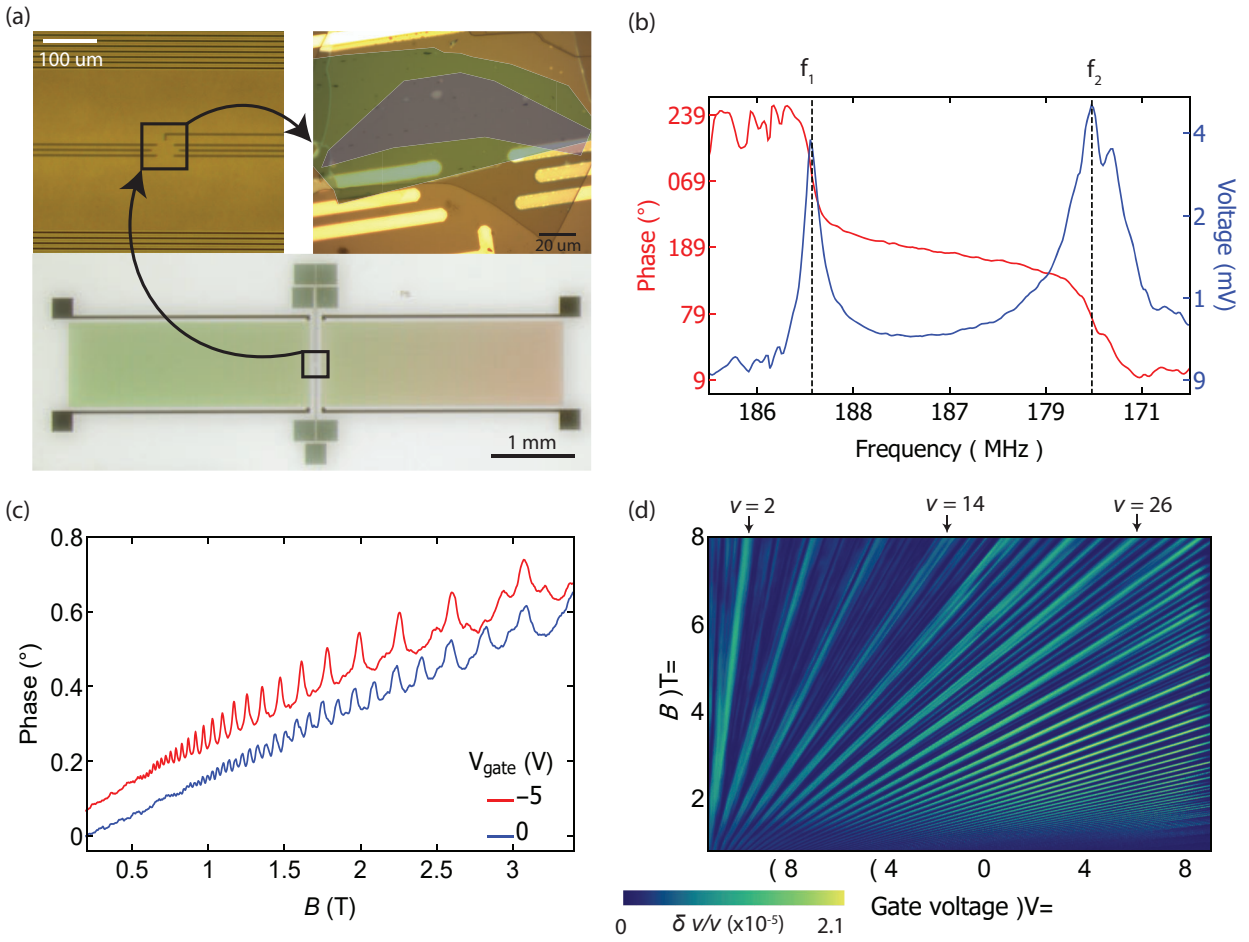

Figure 4.17: **Quantum transport in graphene using a surface acoustic wave resonator.** (a) Optical microscope images device D1. The lower image shows a zoomed-out view of the full SAW resonator cavity. The image on the top left shows a zoomed-in view of the center of the cavity with the detail of the pre-patterned gold electrodes without the graphene sample. The image on the top right shows the graphene device in detail. The monolayer graphene is colored in light purple and the graphite top gate is colored in light green. (b) Amplitude and phase of the transmitted voltage through SAW resonant cavity D1, as a function of frequency at room temperature. Two resonances, marked as f_1 and f_2, are indicated. (c) The change in the phase of D1 at fixed frequency f_1 as a function of magnetic field at two different gate voltages at 1.7 K. Clear quantum oscillations can be observed above 0.6 tesla and oscillations related to degeneracy-broken Landau levels can be observed above 3 tesla. The data have been offset for clarity. (d) Landau fan diagram at 1.7 K, from 1 tesla to 8 tesla. The color scale corresponds to the shift in cavity phase.

the primary frequency is obtained by Fourier-filtering the data over a frequency that only includes the primary frequency. Then, we extract τ_q by directly fitting the filtered oscillatory signal with Equation 2.4, and the result is shown in Figure 4.19. The extracted lifetimes are

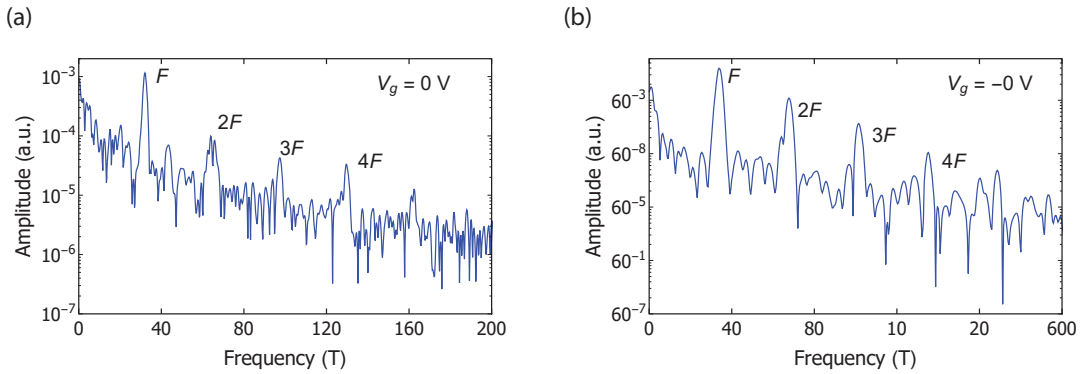

Figure 4.18: **Fast Fourier transform (FFT) of the quantum oscillation data.** FFT of the quantum oscillation data shown in Figure 4.17 after subtraction of a linear background for $V_g = 0$ V (a) and $V_g = -5$ V (b). The pirmary frequency is 32 T and 17 T, for $V_g = 0$ V and $V_g = -5$ V respectively. For both gate voltages, higher harmonics up to the fourth order can be clearly observed.

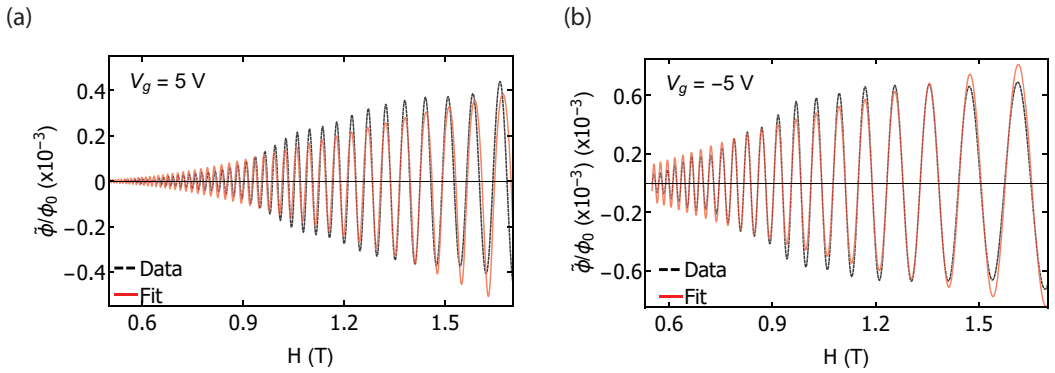

Figure 4.19: **Quantum lifetime extraction.** The dashed black lines are the Fourier-filtered data for the primary oscillation frequency for $V_g = 0$ V (a) and $V_g = -5$ V (b). The red lines are fits to Equation 2.4, which yield quantum scattering times τ of around 0.26 ps for $V_g = 0$ V, and around 0.4 ps for $V_g = -5$ V.

around 0.26 ps for $V_g = 0$ V, and around 0.4 ps for $V_g = -5$ V, corresponding to a quantum mean free path of around 300 nm to 400 nm and quantum mobility of greater than 10^4 cm^2 V^{-1}s^{-1}. This high mobility demonstrates the suitability of black $LiNbO_3$ for high-quality 2D devices.

Next, we examine D1 as a function of gate voltage at fixed magnetic fields. Figure 4.17c shows a Landau fan diagram over the entire available gate voltage range and up to 8

tesla. Above 3 tesla, additional peaks emerge between the main peaks at filling factor $\nu = 2, 6, 10, 14$, etc. At high gate voltage there are clearly three intermediate peaks: these are the additional Landau levels (LLs) that emerge when Zeeman and valley degeneracy have been broken and these have been characterized extensively in high-quality transport devices [125]. At lower gate voltage—closer to the charge neutrality point (CNP)—additional peaks emerge between the main sequence. Some of these features are potentially fractional quantum Hall states, although additional peaks seem to indicate that device inhomogenaity may be responsible. This highlights the fact that SAWs are truly bulk probes: everything in the cavity contributes to the measured phase shift, including lower-mobility regions of the device, the top gate, and any pieces of material left behind during fabrication.

A significant problem with D1 is that only the electron-doped side of the CNP can be reached within the available gate-voltage range. Related to this, the CNP is shifted to nearly -10 volts, which is somewhat surprising given the high quality of the device. This is likely a result of the substrate: $LiNbO_3$ is highly pyroelectric and changes device temperature result in strong electric fields at the surface of the substrate [126]. In addition, the range of accessible gate voltages is a lot smaller than expected. The dielectric constant and the breakdown voltage of hBN are generally $\epsilon \approx 3 - 4$ and $V_{\text{breakdown}} \approx 0.7$ V nm^{-1}[127]. The top hBN of D1 is approximately 64 nm, which should give a gate voltage range of more than 40 volts. Instead, we observe less than 20 volts. One posible explanation for the reduced range is that D1 was designed to maximize the amount of signal by utilizing a thick top hBN layer to reduce the interaction between the top gate and the SAW. Thicker hBN, however, is more likely to have cracks that limit the voltage range over which it can be used as a gate dielectric.

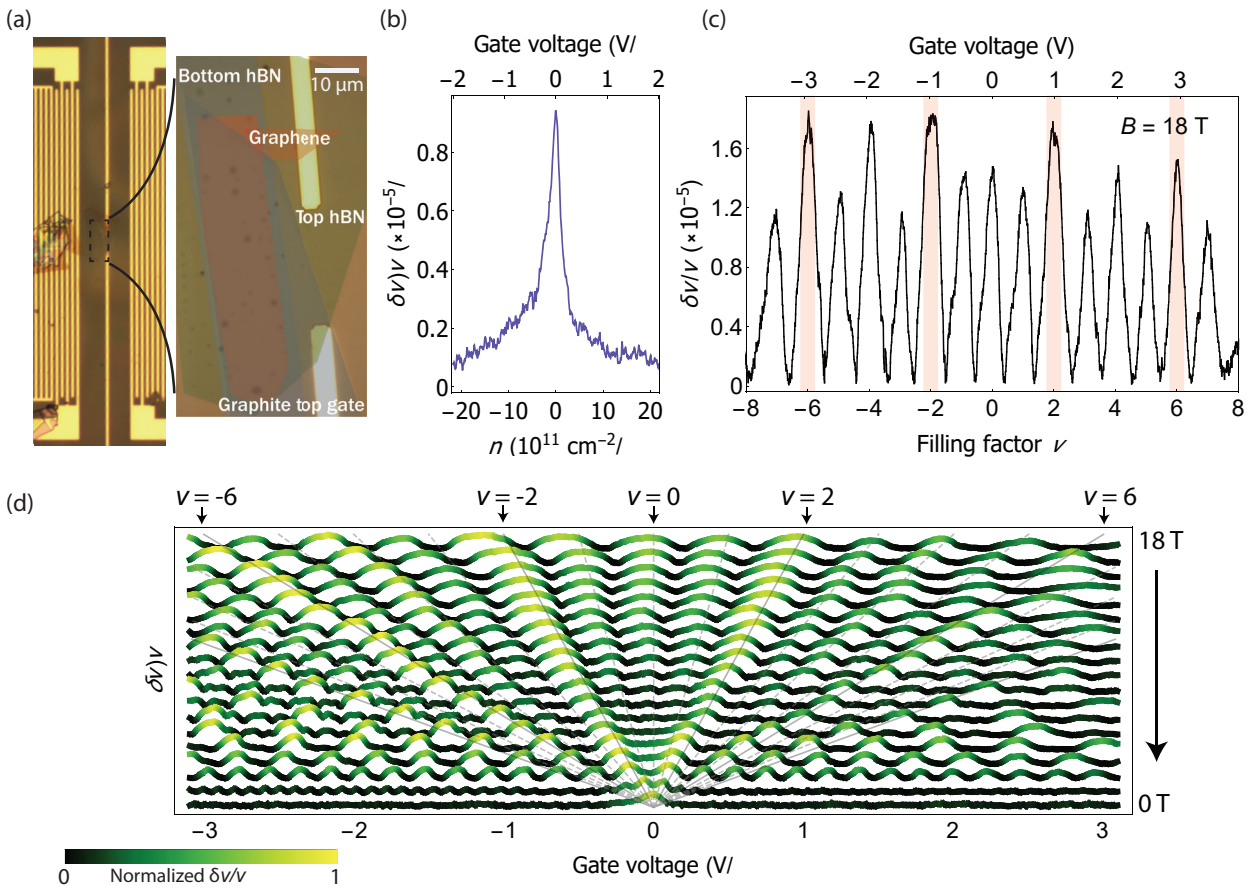

Figure 4.20: **Optimized device geometry and quantum transport to 18 tesla.** (a) Optical microscope images of the SAW resonator cavity and the graphene device. The image on the left shows a zoomed-out view of the SAW resonator cavity, with IDTs and reflectors visible. The image on the right shows a zoomed-in view of the area inside the dashed black box on the left, which shows the graphene device in detail.(b) The phase shift through device D2 as a function of gate voltage at 0.3 kelvin and zero tesla. The phase shift is proportional to the change in 2D conductivity (see Figure 4.14). The width of the peak near the CNP at zero density provides an estimate of the charge-carrier inhomogeneity resulting from electron-hole puddle formation at low densities[14]. (c) $\frac{\delta v}{v}$ as a function of filling factor at 18T and 300 mK. The main peaks marked in pink indicate the regular Landau levels without degeneracy lifting. The three peaks in between indicate the complete lifting of the fourfold degeneracy. (d) Landau fan digram at 300 mK, from 18 T to 0 T. The regular sequence of LLs are indicated by a solid grey line; the degeneracy-broken sequence is indicated by a dashed grey line. Note that the voltage axis has been shifted to align the $\nu = 0$ LLs.

Device D2

Motivated by the successes and challenges of D1, we modified the designs of both our resonator and our graphene heterostructure. To reduce the chance of cracked hBN, as well as

to reduce the chance of having an inhomogeneous device, the top-gate hBN was reduced by a factor of 2. To compensate for the smaller signal, we further reduced the thickness of the graphite top gate, which screens the SAW electric fields and reduces the signal size in proportion to its total conductance. We also optimized the Q-factor of resonator by simulating the full resonators with the model described in subsection 4.5.2 and then producing several different devices with different spacings between the IDTs and the reflectors. We also used thinner gold reflectors that were shorted together, which have been shown to reduce the coupling of the SAWs to the bulk acoustic modes[128]. Device D2 had a quality factor of approximately 5000—a significant improvement over D1.

Device D2 is shown in Figure 4.20b. At zero magnet field, there is a clear and narrow peak in the phase shift measured as a function of carrier density (Figure 4.20a). We identify this peak as the CNP of the graphene, as the phase shift is inversely proportional to the conductivity of the graphene layer. The width of this resistivity peak provides an estimate of the charge-carrier inhomogeneity in the device [14]. The full width at half-maximum of the peak is approximately $\delta n \approx 10 \times 10^{10}$ cm^{-2}, which is comparable to that of typical high-quality hBN encapsulated monolayer graphene devices on Si/SiO_2 substrates [127].

Figure 4.20c shows a gate sweep on D2 at 18 tesla and 300 mK. The symmetry-broken LLs are all clearly resolved, with none of the extraneous peaks that were seen in D1. Figure 4.20d shows gate sweeps at fields from 18 down to 0 tesla at 300 mK, producing a Landau fan diagram centered around the CNP. Note that the data in Figure 4.20 has been shifted horizontally to align the CNP at zero gate voltage.

4.7 Discussion

We have demonstrated that high-quality-factor, two-port, Fabry-Perot SAW resonators fabricated on $LiNbO_3$ can be used to measure quantum transport in graphene heterostructures. We observe degeneracy-broken LLs at less than 3 tesla and extract a quantum lifetime of 0.2 ps, both indicative of high carrier mobility. With improvements to the resonator and sample design, we observe a relatively sharp peak in the cavity phase shift—proportional to the resistivity of the graphene—at the CNP, indicating device homogeneity that is comparable to those produced on typical Si/SiO_2 substrates. It is worth noting again that SAWs are sensitive to the entire bulk of the graphene device, whereas DC transport measurements are weighted toward the cleanest current path: this means that a DC transport measurement of the charge homogeneity in our device would likely be even narrower.

Gate voltage sweep hysteresis

In the measurement we find that there is strong gate hysteresis in D2 likely associated with polarizing the $LiNbO_3$ substrate. D2 shows strong hysteresis in its phase response as the gate voltage is swept in different directions, as shown in Figure 4.21a and b. However, the peak associated with the charge neutrality point at zero field and the quantum oscillations at 8 tesla look very similar, indicating that this hysteresis doesn't seem to be associated with hysteresis in device mobility, only in the carrier density. This hysteresis is removed from Figure 4.20 of the main text by aligning the 0^{th} Landau level and the charge neutrality point at zero volts.

D1 shows significantly less gate hysteresis: the Landau levels at 4.2 tesla are offset by only about a volt (see Figure 4.21b). The origin of the difference in gate hysteresis between the two devices is unknown. One possibility is the difference in bottom hBN: D1 has 10 nm, whereas D2 has 37 nm. This may mean that the graphene in D2 interacts much more

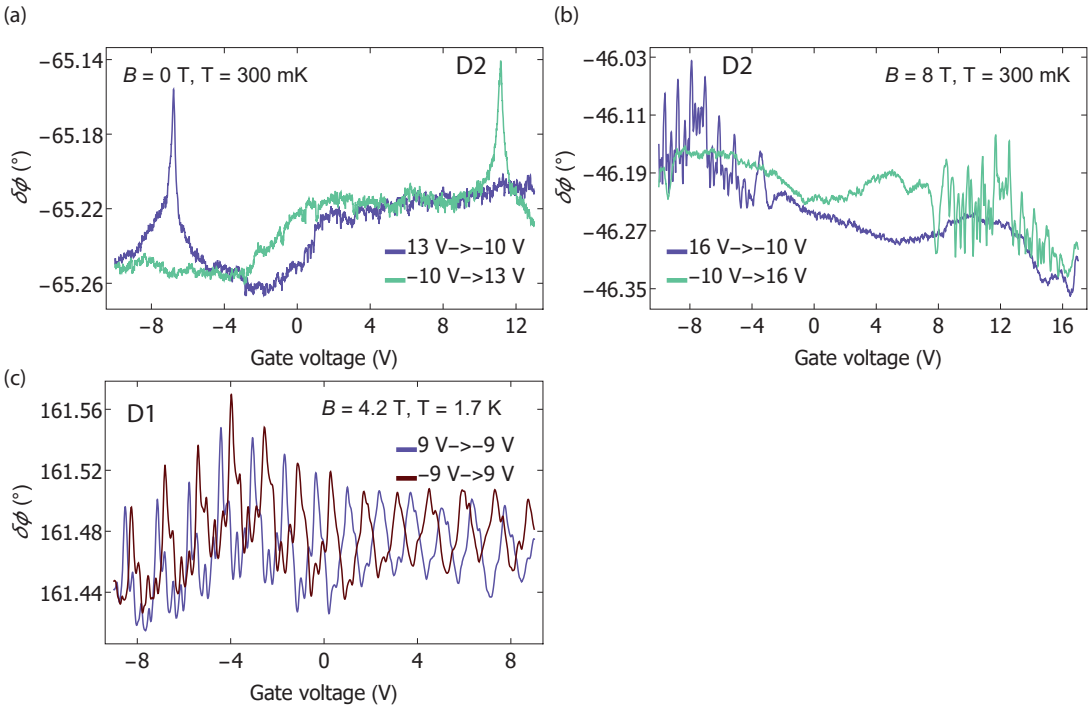

Figure 4.21: **Gate hysteresis.** (a-b) Gate hysteresis in D2. The raw data of gate voltage sweep in two directions at 0T (a) and 8T (b), 300 mK. A large gate hysteresis can be observed. At 0 T, a sharp peak associated with the CNP of the graphene device can be observed at around 12 V at gate sweep up and at around -8 V at gate sweep down. The peaks are of similar width, indicating that the gate hysteresis does not seem to impact the device inhomogeneity level. At 8 T, the Landau levels feature at both gate sweep directions are also similar. (c) Gate hysteresis in D1. The raw data of gate voltage in two directions at 4.2 T and 1.7 K. The gate hysteresis in D1 is much smaller than in D2.

strongly with the highly polar $LiNbO_3$ substrate surface than the graphene in D1. There may be piezoelectric domains in the $LiNbO_3$ substrate that are being switched by the application of the gate voltage, which is significantly closer to the substrate in D2.

The strong gate hysteresis does not seem to negatively impact the device mobility but does indicate that strong surface electric fields are present.

Conversion between conductivity change and SAW phase shift

In principle, Equation 4.19 allows us to convert the change in cavity phase shift and SAW amplitude back to the conductivity of the graphene sample. In 2DESs in GaAs/AlGaAs, this conversion is performed with a simple relaxation-type model, and the calculated result agrees well with the experiment [113]. We used published conductivity data from the quantum Hall regime to estimate the change in cavity phase shift. The longitudinal sheet conductance, σ_{xx}, of graphene changes from 0 when the chemical potential is in a gap in the quantum Hall regime to approximately 4×10^{-6} S when the chemical potential is between gaps at 15 T [129]. A naive application of Equation 4.19, using $Q = 1500$, $A_s = 1000\mu\text{m}^2$, $A_c = 6.6 \times 10^5\mu$ m^2, gives a predicted phase shift of approximately 5.5° as the chemical potential is swept between integer filling factors. This is roughly an order of magnitude larger than the measured phase shift of approximately 0.1° (Figure 4.17).

The disagreement is likely a result of the graphite top gate partially shorting the SAW electric field and the estimation of the effective cavity length. To better estimate the expected cavity phase shift, we perform finite element method simulations to simulate the resonator with the actual sample dimensions.

The 2D model of the resonator used in the estimation of the change in sample conductivity from the measured phase shift consists of five fingers in each IDT, one hundred metallic strips in each Bragg mirror, and a cavity length of 12 λ. The design of this model is the same as the SAW resonant cavity used in Device 1, except in Device, there are 250 metal strips in each Bragg mirror. This reduction in the number is to speed up the simulation. Each eigenmode of the analysis corresponds to a integer number of SAW wavelengths in the cavity. Using the spacing between each resonance frequency (3 MHz) and the known speed of sound we calculate an effective cavity length of around 660 μm—much longer than the physical distance of 240 μm between the reflectors. This is because of the large number of metallic

strips required to produce a Bragg mirror that effectively contains the SAW.

we perform a COMSOL simulation with a full model of D1, including 100 reflectors on each side of the cavity, shown in Figure 4.12. This simulation produces a quality factor of approximately 2000 and a resonance frequency of approximately 187 MHz (Figure 4.13b): both values are very similar to those measured for device D1. We set the conductivity of the graphite top gate to 3×10^7 S/m[122] and vary the conductance of the graphene sample between 0 and 4×10^{-6} S. The phase shift produced near the resonance frequency for this variation in graphene conductance is approximately 6.6 °—closer to the measured phase shift. This value is improved by considering the real device geometry in the third dimension that is omitted from the simulation: the real sample spans only approximately 100 μm of the 1 mm cavity width (Figure 4.17a). Accounting for this third dimension then reduces the phase shift by a factor of 10: this result is shown in Figure 4.22. The total phase shift expected when gating between Landau level is then approximately 0.66 °, which is now within an order of magnitude of the measured values shown in Figure 4.17c of the main text. Note that the conductivity of our graphite and graphene could vary considerably from the values we have chosen for the simulations. In addition, because one of the graphene dimensions is roughly equal to the SAW wavelength, the position of the sample with respect to the nodes of the standing waves can change the phase shift considerably. Finally, the presence of gate and transport electrodes in D1 will impact the amplitude of the electric fields seen at the sample—these were not included in the 2D model.

Although the estimated phase shift from the simulation still overestimates the cavity phase shift, they are within the same order of magnitude. The remaining discrepancy could come from sample geometry, sample inhomogeneity, and sample position in the cavity. In order to quantitatively extract conductivity, a homogeneous sample with well-defined simple rectangular geometry is required.

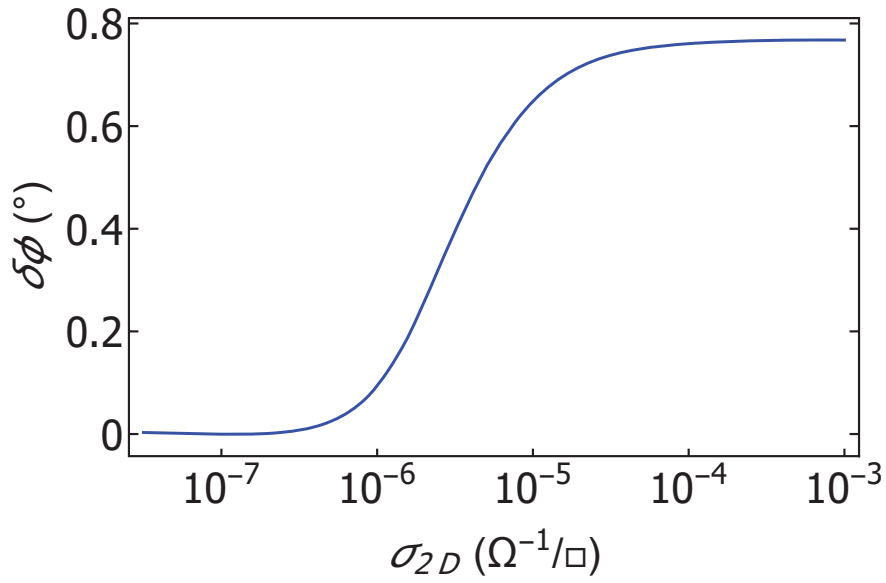

Figure 4.22: **COMSOL simulation of SAW resonators.** The simulated phase at IDT2 as a function of the graphene longitudinal sheet conductance, scaled by the 0.1 to account for the ratio between the width of the sample and the cavity. In the simulation, the drive frequency is fixed to be 187.33 MHz, and the conductivity of the graphite top gate is set to be 3×10^7 S/m.

4.8 Conclusion and outlook

We used SAW resonators operating at 200 MHz in this study because the 20 μm feature size is easily achievable with cost-efficient, standard photolithographic techniques. SAW resonators operating up into the GHz frequency range, however, are a well-established and mature technology—a typical smartphone contains more than a dozen SAW filters and delay lines, and SAW filters operating at 3 GHz can be purchased for under a dollar. Having demonstrated that SAW resonators on $LiNbO_3$ have the requisite signal to noise for measuring small heterostructures, it should now be possible to explore wave-vector dependent effects down to hundreds-of-nanometer lengthscales. Immediately accessible experiments based on existing theoretical proposals include searching for the crossover from Dirac to

Schrodinger-like behaviour in the longitudinal conductivity of graphene [24], and measuring the SAW attenuation of a twisted bilayer graphene device as a function of chemical potential to look for non-Fermi-liquid signatures [25]. With further development, one could imagine using SAW resonators to impose a dynamic, periodic potentials on 2D heterostrucures that are both tunable and switchable on ns timescales.

APPENDIX A

MATHEMATICA CODE FOR THE CALCULATION OS ADMR WITH CDW FERMI SURFACE RECONSTRUCTION

The calculation of the angular-dependent magnetoresistance can be divided into two steps. The first step is to find a uniform grid of points in momentum space on the Fermi surface. Using an analytical model for the energy-momentum dispersion relation, we can find a uniform grid on the Fermi surface (FS) with some form of Newton's method with cleverly chosen initial conditions. However, the same initial condition may fail for FS of a different shape. For example, the initial conditions that work for a closed FS may fail for an open FS, and the initial conditions that work for a large square FS may fail for a small circular FS. Moreover, obtaining the FS grid with a complicated dispersion relation that does not have an analytical model would be very challenging, such as a dispersion computed with density functional theory (DFT) or the charge density wave reconstructed FS in this thesis. The FS griding find problem for a general dispersion can be considered a contour finding problem in computer vision. One of the standard algorithms for this task is the marching squares algorithm. In this thesis, a modified version of the marching squares algorithm is implemented with Wolfram Mathematica and proceeds as follows. For simplicity, I will only discuss finding the FS in 2D here. Finding the FS with a 3D dispersion could be done by repeating this 2D method for each k_z.

1. The first step is to load the energy as a function of momentum data. The dispersion data can be obtained from the DFT calculation or the CDW reconstructed dispersion calculated with Equation 3.7. There could be multiple bands in the dispersion data. As only the bands that cross the Fermi energy and only their part near the Fermi energy are relevant in the calculation (Equation 3.2), these data need to be isolated. For example, in the calculation of ADMR with the CDW reconstructed FS, we are only interested in the small electron pocket at nodal positions in the Brillouin zone. However, there are other pieces of the FS

near the electron pocket. We isolate the electron pocket by applying some cutoffs in k_x and k_y in the momentum space, where only the electron pocket is inside the selected momentum space region.

2. With the relevant data points isolated, the next step is to build a smooth and differentiable function by interpolating the data points from step 1 using the "Interpolation" function in Wolfram Mathematica with "InterpolationOrder" usually set to be one. Although this choice of "InterpolationOrder" is not required, as the isolated data is usually not on a uniform grid in the momentum space, lower order usually makes a better approximation.

3. Then, divide the 2D k-space of interest into regularly spaced square/rectangular grids and compute the energy of the four vertices of each grid.

4. Then, the grids that intersect the FS need to be identified. If we draw the FS contour, a grid will have the FS contour going through it if some vertices have energy larger than zero and some have energy smaller than zero.

5. The grids that belong to different FS pieces are then grouped together for extra processing in later steps. This is achieved by building an undirected graph by joining adjacent grids and grouping the connected ones using the "ConnectedComponents" function in Wolfram Mathematica.

6. The grouped grids are further refined by repeating steps 3-4 for each grid by subdividing the grid and selecting the finer grid that intersects the FS.

7. The points on the FS contours are determined from the selected grids in step 6. There are several methods for picking the points. Here in the calculation, the middle points of the edges on which the FS contours intersect are selected. The edges with only one of the vertices having energy greater than zero will have the FS contours going through it.

8. The points need to be ordered and joined together properly. Although points belonging

to different FS pieces are grouped, they need to be sorted and joined together for later processing. Here, we sort the points by cleverly choosing a center for each FS piece. For example, for a closed convex closed FS, the actual center of the FS could be used, and for an open FS piece, a point outside the FS piece needs to be used. Then, we compute the angle between the vector, pointing from the center to the FS points and the unit vector $\hat{k_x}$, and sort the points by the angle.

9. The last step is to obtain a uniform grid of each FS piece. This is acheived by computing the accumulative sum of the distance between each adjacent point in the sorted point list and building an interpolated function of the x and y coordinate as a function of the accumulative distance.

With a uniform grid of the Fermi surface, the remaining task is to solve the differential equation as described in subsection 3.3.2. From step 2, a smooth and differentiable function is obtained for the dispersion near the Fermi energy. The rest of the calculation is the same as that for any other simple band structure.

The sample codes for the calculation of ADMR with CDW reconstructed FS can be found in `https://github.com/yf257/admr_cdw_9x9`.

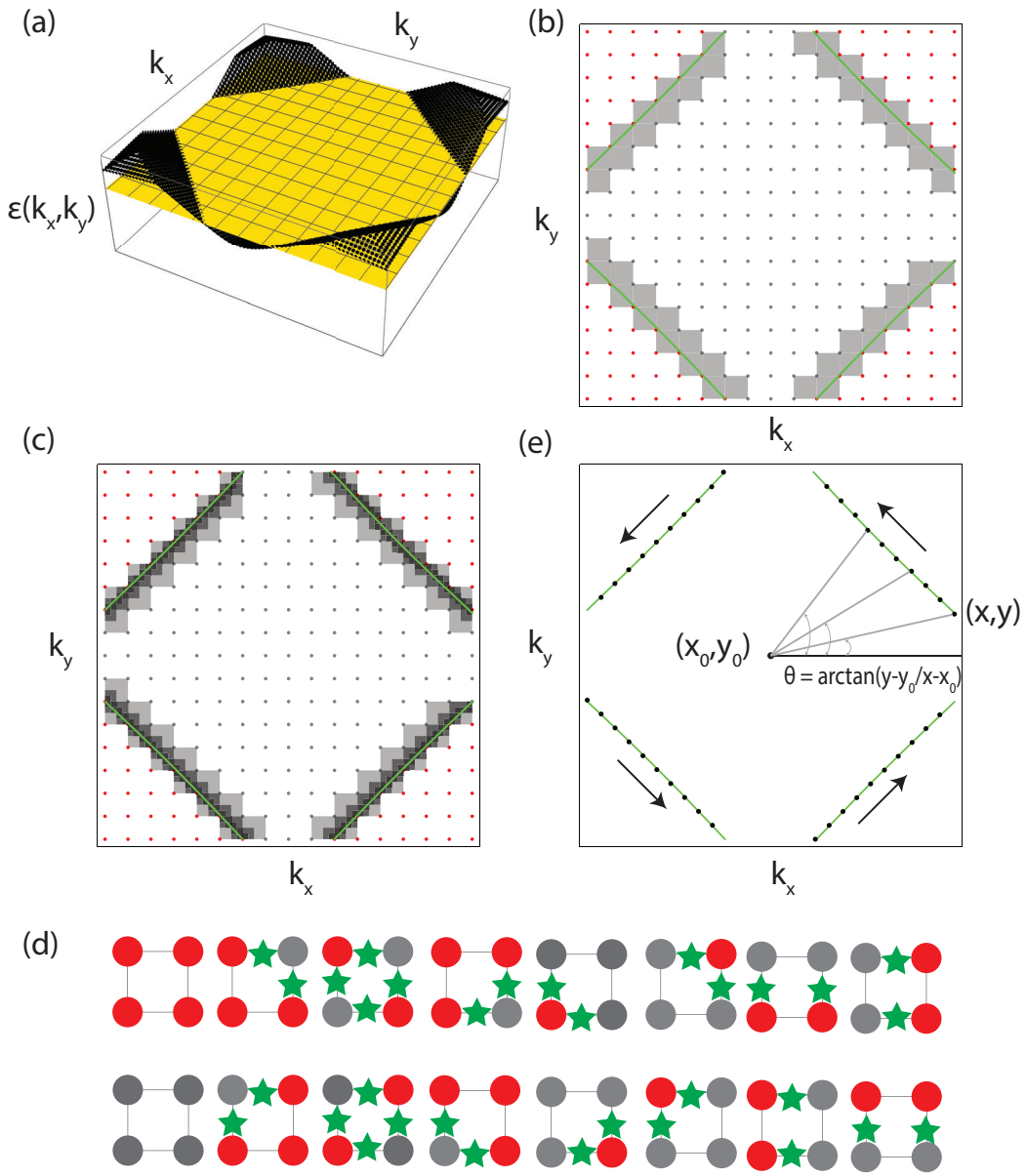

Figure A.1: (a) Illustration of step 1. Black points represent the dispersion data point, and the orange plane represents the Fermi energy. Their intersection represents the Fermi surface contour. For simplicity, here, a 2D dispersion is used as an example; in principle, this method can also be used in 3D cases. (b) Illustration of steps 3 and 4. The green line represents the Fermi surface contour, the red dots represent the vertices that have energy larger than the Fermi energy, and the gray dots represent the vertices that have energy smaller than the Fermi energy. The gray boxes represent the selected grid that intersects the FS. (c) Illustration of step 6. Steps 3 and 4 are repeated twice. (d) Illustration of step 7. All 16 possible cases are shown. The red dots represent the vertices that have energy larger than the Fermi energy, and the gray dots represent the vertices that have energy smaller than the Fermi energy. The green stars represent the selected middle points of the edges on which the FS contours intersect. (e) Illustration of steps 8 and 9. The arrow represents the order of the sorted point list. The black dots represent the final uniform grid of the FS.

APPENDIX B

COMSOL FULL MODEL RESULT FOR SAW RESONATOR DESIGN

This appendix presents some results of the full resonator COMSOL model (see subsection 4.5.2 for the detail) with 300 nm of gold as reflectors, the wavelength to be 20 μm, no sample inside the cavity, and different design parameters, l_{rr} and l_{rt}.

Figure B.1 shows the voltage amplitude at IDT2 as a function of frequency at three different l_{rr} and each at nine different l_{rt}. These simulation results clearly show that the cavity's resonant frequency and Q factor greatly depend on l_{rr} and l_{rt}. It can be roughly identified that the pass band of the IDTs is between 186 MHz and 191 MHz and the center of the pass band is around 188.5 MHz. It can be clearly seen that with different l_{rr}, the resonant frequency is shifted slightly, and when the resonant frequency is near the center of the pass band (Figure B.1bc), the maximum measurable voltage is larger with optimum l_{rt}.

Table B.1 shows the Q factor of f1 in Figure B.1b for different l_{rt}. From Figure B.1 and Table B.1, it can be clearly observed that with slightly different l_rt, the Q factor of the resonance is very different. Using these simulation results, we can screen out the parameters that result in resonators that have resonances with a low Q factor in the simulation. For example, in Table B.1, with l_{rr} to be $\lambda(12 + (-0.125))$, the quality factor of the resonance with l_{rt} to be $0.5\lambda(1+0.25)$ is one 1069, half of that with l_{rt} to be $0.5\lambda(1-0.25)$, so we won't use the set of parameters with $l_{rr} = \lambda(12 + (-0.125))$ together with $l_{rt} = 0.5\lambda(1 - 0.25)$.

In reality, the experimental result can sometimes differ from the simulation result, as the simulation does not take the conductivity of the gold reflectors or the impedance of the drive and measure circuit into account. Instead of only fabricating the resonator with the one set of parameters leading to the highest Q factor, we select the first ten sets of parameters with the highest Q factor. Most of the time the experimental result agrees well with the simulation result (see Figure 4.13).

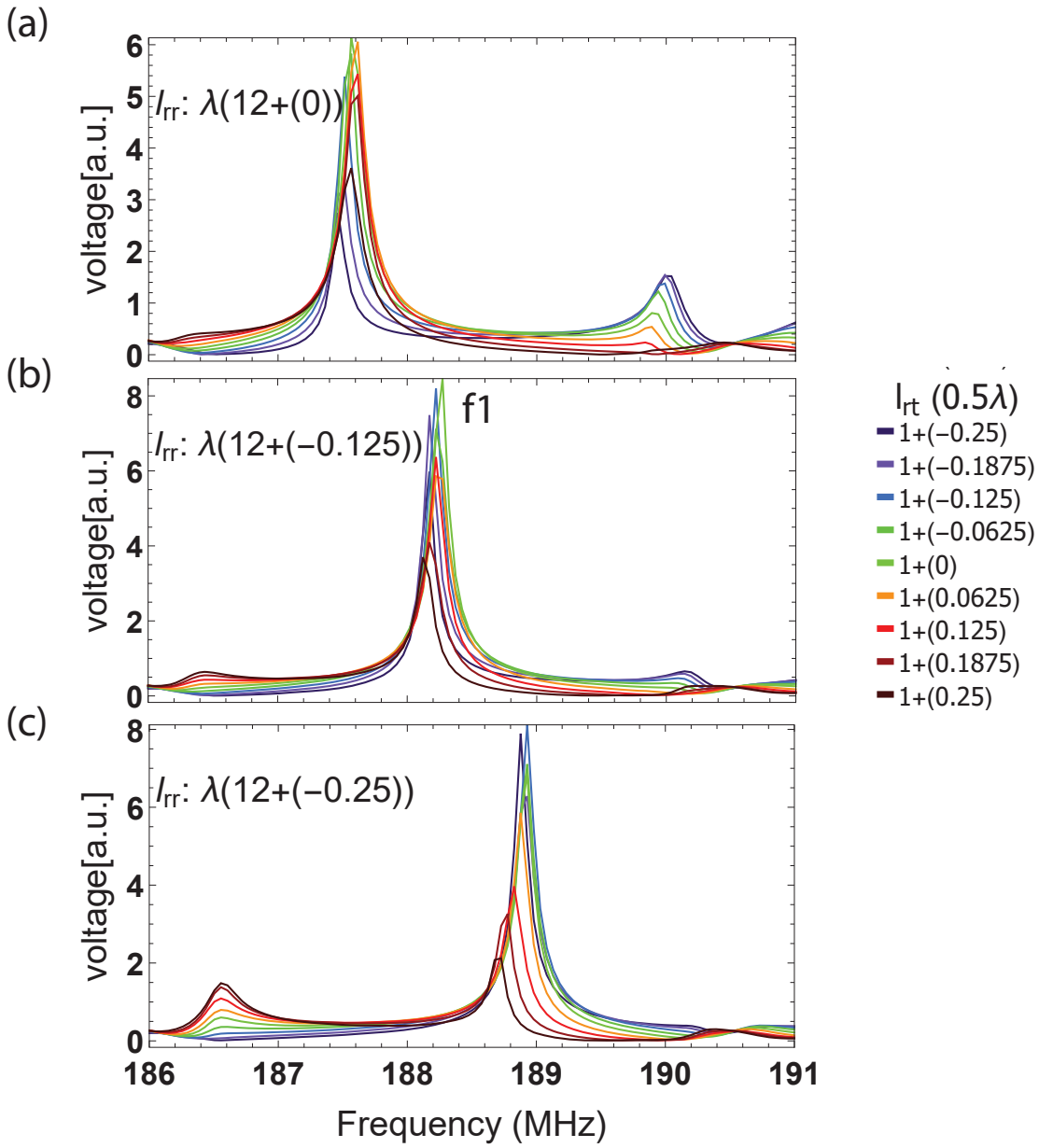

Figure B.1: The simulation results of the full resonator model (subsection 4.5.2). The voltage amplitude at IDT2 as a function of frequency.(a) Simulation results with l_{rr} to be 12λ. (b) Simulation results with l_{rr} to be $\lambda(12 + (-0.125))$. (c) Simulation results with l_{rr} to be $\lambda(12 + (-0.25))$. λ is the wavelength of the resonantor, and is set to be 20 μm in the simulation.

l_{rt} **(0.5λ)**	**Q factor**
1-0.25	2283
1-0.1875	1967
1-0.125	1657
1-0.0625	1969
1	1530
1+0.0625	1472
1+0.125	1457
1+0.1875	1276
1+0.25	1069

Table B.1: The quality factor of resonance f_1 in Figure B.1b with l_{rr} to be $\lambda(12 + (-0.125))$ and different l_{rt}.

BIBLIOGRAPHY

[1] Bulat Burganov, Carolina Adamo, Andrew Mulder, M Uchida, PDC King, JW Harter, DE Shai, AS Gibbs, AP Mackenzie, Reinhard Uecker, et al. Strain control of fermiology and many-body interactions in two-dimensional ruthenates. *Physical review letters*, 116(19):197003, 2016.

[2] C Bergemann, SR Julian, AP Mackenzie, AW Tyler, DE Farrell, Y Maeno, and S Nishizaki. Quantum oscillations and overcritical torque interaction in Sr_2RuO_4. *Physica C: Superconductivity*, 317:444–447, 1999.

[3] C Bergemann, JS Brooks, L Balicas, AP Mackenzie, SR Julian, ZQ Mao, and Y Maeno. Normal state of the unconventional superconductor Sr_2RuO_4 in high magnetic fields. *Physica B: Condensed Matter*, 294:371–374, 2001.

[4] A. P. Mackenzie, S. R. Julian, A. J. Diver, G. J. McMullan, M. P. Ray, G. G. Lonzarich, Y. Maeno, S. Nishizaki, and T. Fujita. Quantum oscillations in the layered perovskite superconductor Sr_2RuO_4. *Phys. Rev. Lett.*, 76:3786–3789, May 1996.

[5] Christian E Matt, Claudia G Fatuzzo, Yasmine Sassa, Martin Månsson, S Fatale, V Bitetta, X Shi, Stéphane Pailhès, MH Berntsen, Tohru Kurosawa, et al. Electron scattering, charge order, and pseudogap physics in $La_{1.6-x}Nd_{0.4}Sr_xCuO_4$: an angle-resolved photoemission spectroscopy study. *Physical Review B*, 92(13):134524, 2015.

[6] Masafumi Horio, Kevin Hauser, Yasmine Sassa, Zarina Mingazheva, Denys Sutter, Kevin Kramer, Ashley Cook, Elisabetta Nocerino, Ola Kenji Forslund, Oscar Tjernberg, et al. Three-dimensional fermi surface of overdoped La-based cuprates. *Physical review letters*, 121(7):077004, 2018.

[7] Alberto Hernández-Mínguez, YT Liou, and PV Santos. Interaction of surface acoustic waves with electronic excitations in graphene. *Journal of Physics D: Applied Physics*, 51(38):383001, 2018.

[8] Qianli Ma, Kirrily C. Rule, Zachary W. Cronkwright, Mirela Dragomir, Gabrielle Mitchell, Evan M. Smith, Songxue Chi, Alexander I. Kolesnikov, Matthew B. Stone, and Bruce D. Gaulin. Parallel spin stripes and their coexistence with superconducting ground states at optimal and high doping in $La_{1.6-x}Nd_{0.4}Sr_xCuO_4$. *Phys. Rev. Research*, 3:023151, May 2021.

[9] Ramzy Daou, Nicolas Doiron-Leyraud, David LeBoeuf, SY Li, Francis Laliberté, Olivier Cyr-Choiniere, YJ Jo, Luis Balicas, J-Q Yan, J-S Zhou, et al. Linear temperature dependence of resistivity and change in the fermi surface at the pseudogap critical point of a high-T_c superconductor. *Nature Physics*, 5(1):31–34, 2009.

[10] C Collignon, S Badoux, SAA Afshar, B Michon, F Laliberté, O Cyr-Choinière, J-S Zhou, S Licciardello, S Wiedmann, N Doiron-Leyraud, et al. Fermi-surface transformation across the pseudogap critical point of the cuprate superconductor $La_{1.6-x}Nd_{0.4}Sr_xCuO_4$. *Physical Review B*, 95(22):224517, 2017.

[11] Naman K. Gupta, C. McMahon, R. Sutarto, T. Shi, R. Gong, Haofei I. Wei, K. M. Shen, F. He, Q. Ma, M. Dragomir, B. D. Gaulin, and D. G. Hawthorn. Vanishing nematic order beyond the pseudogap phase in overdoped cuprate superconductors. *Proceedings of the National Academy of Sciences*, 118(34), 2021.

[12] JM Tranquada, BJ Sternlieb, JD Axe, Y Nakamura, and S Uchida. Evidence for stripe correlations of spins and holes in copper oxide superconductors. *nature*, 375(6532):561–563, 1995.

[13] BJ Ramshaw, N Harrison, SE Sebastian, S Ghannadzadeh, KA Modic, DA Bonn, WN Hardy, Ruixing Liang, and PA Goddard. Broken rotational symmetry on the Fermi surface of a high-T_c superconductor. *npj Quantum Materials*, 2(1):8, 2017.

[14] K.I. Bolotin, K.J. Sikes, Z. Jiang, M. Klima, G. Fudenberg, J. Hone, P. Kim, and H.L.

Stormer. Ultrahigh electron mobility in suspended graphene. *Solid state communications*, 146(9-10):351–355, 2008.

[15] Kostya S Novoselov, Andre K Geim, Sergei Vladimirovich Morozov, Dingde Jiang, Michail I Katsnelson, IVa Grigorieva, SVb Dubonos, and andAA Firsov. Two-dimensional gas of massless dirac fermions in graphene. *nature*, 438(7065):197–200, 2005.

[16] Andrej Pustogow, Yongkang Luo, Aaron Chronister, Y-S Su, DA Sokolov, Fabian Jerzembeck, Andrew Peter Mackenzie, Clifford William Hicks, Naoki Kikugawa, Srinivas Raghu, et al. Constraints on the superconducting order parameter in sr2ruo4 from oxygen-17 nuclear magnetic resonance. *Nature*, 574(7776):72–75, 2019.

[17] Yi-Ting Hsu, Weejee Cho, Alejandro Federico Rebola, Bulat Burganov, Carolina Adamo, Kyle M Shen, Darrell G Schlom, Craig J Fennie, and Eun-Ah Kim. Manipulating superconductivity in ruthenates through fermi surface engineering. *Physical Review B*, 94(4):045118, 2016.

[18] Hari P Nair, Jacob P Ruf, Nathaniel J Schreiber, Ludi Miao, Morgan L Grandon, David J Baek, Berit H Goodge, Jacob PC Ruff, Lena F Kourkoutis, Kyle M Shen, et al. Demystifying the growth of superconducting sr2ruo4 thin films. *APL Materials*, 6(10):101108, 2018.

[19] Gaël Grissonnanche, Yawen Fang, Anaëlle Legros, Simon Verret, Francis Laliberté, Clément Collignon, Jianshi Zhou, David Graf, Paul A Goddard, Louis Taillefer, et al. Linear-in temperature resistivity from an isotropic planckian scattering rate. *Nature*, 595(7869):667–672, 2021.

[20] C Bergemann, AP Mackenzie, SR Julian, D Forsythe, and E Ohmichi. Quasi-two-dimensional fermi liquid properties of the unconventional superconductor Sr_2RuO_4. *advances in Physics*, 52(7):639–725, 2003.

[21] I Razado-Colambo, J Avila, J-P Nys, C Chen, X Wallart, M-C Asensio, and D Vignaud. Nanoarpes of twisted bilayer graphene on sic: absence of velocity renormalization for small angles. *Scientific reports*, 6(1):1–7, 2016.

[22] Nikhil Tilak, Xinyuan Lai, Shuang Wu, Zhenyuan Zhang, Mingyu Xu, Raquel de Almeida Ribeiro, Paul C Canfield, and Eva Y Andrei. Flat band carrier confinement in magic-angle twisted bilayer graphene. *Nature communications*, 12(1):1–7, 2021.

[23] R. L. Willett, R. R. Ruel, K. W. West, and L. N. Pfeiffer. Experimental demonstration of a fermi surface at one-half filling of the lowest landau level. *Phys. Rev. Lett.*, 71:3846–3849, Dec 1993.

[24] Peter Thalmeier, Balázs Dóra, and Klaus Ziegler. Surface acoustic wave propagation in graphene. *Physical Review B*, 81(4):041409, 2010.

[25] Ajesh Kumar, Zihan Cheng, and Andrew C Potter. Fractal non-fermi liquids from moiré hofstadter phonons. *Physical Review B*, 102(23):235120, 2020.

[26] Yawen Fang, Hari P Nair, Ludi Miao, Berit Goodge, Nathaniel J Schreiber, Jacob P Ruf, Lena F Kourkoutis, Kyle M Shen, Darrell G Schlom, and BJ Ramshaw. Quantum oscillations and quasiparticle properties of thin film sr 2 ruo 4. *Physical Review B*, 104(4):045152, 2021.

[27] A. Pustogow, Yongkang Luo, A. Chronister, Y.-S. Su, D. A. Sokolov, F. Jerzembeck, A. P. Mackenzie, C. W. Hicks, N. Kikugawa, S. Raghu, E. D. Bauer, and S. E. Brown. Constraints on the superconducting order parameter in Sr_2RuO_4 from oxygen-17 nuclear magnetic resonance. *Nature*, 574(7776):72–75, 2019.

[28] Steven Allan Kivelson, Andrew Chang Yuan, Brad Ramshaw, and Ronny Thomale. A proposal for reconciling diverse experiments on the superconducting state in Sr_2RuO_4. *npj Quantum Materials*, 5(1):1–8, 2020.

[29] Sayak Ghosh, Arkady Shekhter, F Jerzembeck, N Kikugawa, Dmitry A Sokolov, Manuel Brando, AP Mackenzie, Clifford W Hicks, and BJ Ramshaw. Thermodynamic evidence for a two-component superconducting order parameter in Sr_2RuO_4. *Nature Physics*, 17(2):199–204, 2021.

[30] S. Raghu, A. Kapitulnik, and S. A. Kivelson. Hidden quasi-one-dimensional superconductivity in Sr_2RuO_4. *Phys. Rev. Lett.*, 105:136401, Sep 2010.

[31] Li-Da Zhang, Wen Huang, Fan Yang, and Hong Yao. Superconducting pairing in Sr_2RuO_4 from weak to intermediate coupling. *Phys. Rev. B*, 97:060510, Feb 2018.

[32] Clifford W Hicks, Daniel O Brodsky, Edward A Yelland, Alexandra S Gibbs, Jan AN Bruin, Mark E Barber, Stephen D Edkins, Keigo Nishimura, Shingo Yonezawa, Yoshiteru Maeno, et al. Strong increase of tc of Sr_2RuO_4 under both tensile and compressive strain. *Science*, 344(6181):283–285, 2014.

[33] S Madhavan, DG Schlom, A Dabkowski, HA Dabkowska, and Y Liu. Growth of epitaxial a-axis and c-axis oriented Sr_2RuO_4 films. *APPLIED PHYSICS LETTERS*, 68(4):559–561, JAN 22 1996.

[34] A. P. Mackenzie, R. K. W. Haselwimmer, A. W. Tyler, G. G. Lonzarich, Y. Mori, S. Nishizaki, and Y. Maeno. Extremely strong dependence of superconductivity on disorder in Sr_2RuO_4. *Phys. Rev. Lett.*, 80:161–164, Jan 1998.

[35] M Uchida, M Ide, H Watanabe, KS Takahashi, Y Tokura, and M Kawasaki. Molecular beam epitaxy growth of superconducting Sr_2RuO_4 films. *APL Materials*, 5(10):106108, 2017.

[36] Carla Maria Palomares Garcia, Angelo Di Bernardo, Graham Kimbell, Mary E Vickers, Fabien CP Massabuau, Sachio Komori, Giorgio Divitini, Yuuki Yasui, Han Gyeol Lee, Jinkwon Kim, et al. Pair suppression caused by mosaic-twist defects in superconducting

Sr_2RuO_4 thin-films prepared using pulsed laser deposition. *Communications Materials*, 1(1):1–8, 2020.

[37] Mark A Zurbuchen, Yunfa Jia, Stacy Knapp, Altaf H Carim, Darrell G Schlom, Ling-Nian Zou, and Ying Liu. Suppression of superconductivity by crystallographic defects in epitaxial sr 2 ruo 4 films. *Applied Physics Letters*, 78(16):2351–2353, 2001.

[38] Mark A Zurbuchen, Yunfa Jia, Stacy Knapp, Altaf H Carim, Darrell G Schlom, and XQ Pan. Defect generation by preferred nucleation in epitaxial $Sr_2RuO_4/LaAlO_3$. *Applied physics letters*, 83(19):3891–3893, 2003.

[39] Mark A Zurbuchen, Yunfa Jia, Stacy Knapp, Altaf H Carim, Darrell G Schlom, and XQ Pan. Defect generation by preferred nucleation in epitaxial sr 2 ruo 4/laalo 3. *Applied physics letters*, 83(19):3891–3893, 2003.

[40] David Shoenberg. *Magnetic oscillations in metals*. Cambridge university press, 1984.

[41] RG Chambers. The kinetic formulation of conduction problems. *Proceedings of the Physical Society. Section A*, 65(6):458, 1952.

[42] A.P. Mackenzie, S.R. Julian, A.J. Diver, G.G. Lonzarich, N.E. Hussey, Y. Maeno, S. Nishizaki, and T. Fujita. Calculation of thermodynamic and transport properties of Sr_2RuO_4 at low temperatures using known fermi surface parameters. *Physica C: Superconductivity*, 263(1-4):510–515, May 1996.

[43] Nicholas P. Breznay, Ian M. Hayes, B. J. Ramshaw, Ross D. McDonald, Yoshiharu Krockenberger, Ai Ikeda, Hiroshi Irie, Hideki Yamamoto, and James G. Analytis. Shubnikov-de haas quantum oscillations reveal a reconstructed fermi surface near optimal doping in a thin film of the cuprate superconductor $Pr_{1.86}Ce_{0.14}CuO_{4\pm\delta}$. *Phys. Rev. B*, 94:104514, Sep 2016.

[44] Rahul Sharma, Stephen D Edkins, Zhenyu Wang, Andrey Kostin, Chanchal Sow, Yoshiteru Maeno, Andrew P Mackenzie, JC Séamus Davis, and Vidya Madhavan. Momentum-resolved superconducting energy gaps of sr_2ruo_4 from quasiparticle interference imaging. *Proceedings of the National Academy of Sciences*, 117(10):5222–5227, 2020.

[45] M. J. Manfra, S. H. Simon, K. W. Baldwin, A. M. Sergent, K. W. West, R. J. Molnar, and J. Caissie. Quantum and transport lifetimes in a tunable low-density AlGaN/GaN two-dimensional electron gas. *Applied Physics Letters*, 85(22):5278–5280, nov 2004.

[46] Darrell G Schlom, Long-Qing Chen, Craig J Fennie, Venkatraman Gopalan, David A Muller, Xiaoqing Pan, Ramamoorthy Ramesh, and Reinhard Uecker. Elastic strain engineering of ferroic oxides. *Mrs Bulletin*, 39(2):118, 2014.

[47] Yawen Fang, Gael Grissonnanche, Anaelle Legros, Simon Verret, Francis Laliberté, Clément Collignon, Amirreza Ataei, Maxime Dion, Jianshi Zhou, David Graf, et al. Fermi surface transformation at the pseudogap critical point of a cuprate superconductor. *Nature Physics*, 18(5):558–564, 2022.

[48] G. Grissonnanche, Y. Fang, A. Legros, S. Verret, F. Laliberté, C. Collignon, J. Zhou, D. Graf, P. Goddard, L. Taillefer, and B. J. Ramshaw. Linear in temperature resistivity from an isotropic planckian scattering rate. *Nature*, 595(7869):667–672, 2021.

[49] Bernhard Keimer, Steven A Kivelson, Michael R Norman, Shinichi Uchida, and J Zaanen. From quantum matter to high-temperature superconductivity in copper oxides. *Nature*, 518(7538):179–186, 2015.

[50] NE Hussey, M Abdel-Jawad, A Carrington, AP Mackenzie, and L Balicas. A coherent three-dimensional fermi surface in a high-transition-temperature superconductor. *Nature*, 425(6960):814–817, 2003.

[51] M. Platé, J. D. F. Mottershead, I. S. Elfimov, D. C. Peets, Ruixing Liang, D. A. Bonn, W. N. Hardy, S. Chiuzbaian, M. Falub, M. Shi, L. Patthey, and A. Damascelli. Fermi surface and quasiparticle excitations of overdoped $Tl_2Ba_2CuO_{6+\delta}$. *Phys. Rev. Lett.*, 95:077001, Aug 2005.

[52] B Vignolle, A Carrington, RA Cooper, MMJ French, AP Mackenzie, C Jaudet, D Vignolles, Cyril Proust, and NE Hussey. Quantum oscillations in an overdoped high-T_c superconductor. *Nature*, 455(7215):952–955, 2008.

[53] Andrea Damascelli, Zahid Hussain, and Zhi-Xun Shen. Angle-resolved photoemission studies of the cuprate superconductors. *Reviews of modern physics*, 75(2):473–541, 2003.

[54] RA Cooper, Y Wang, B Vignolle, OJ Lipscombe, SM Hayden, Yoichi Tanabe, T Adachi, Yoji Koike, Minoru Nohara, H Takagi, et al. Anomalous criticality in the electrical resistivity of $La_{2-x}Sr_xCuO_4$. *Science*, 323(5914):603–607, 2009.

[55] Nicolas Doiron-Leyraud, Cyril Proust, David LeBoeuf, Julien Levallois, Jean-Baptiste Bonnemaison, Ruixing Liang, DA Bonn, WN Hardy, and Louis Taillefer. Quantum oscillations and the fermi surface in an underdoped high-T_c superconductor. *Nature*, 447(7144):565–568, 2007.

[56] BJ Ramshaw, SE Sebastian, RD McDonald, James Day, BS Tan, Z Zhu, JB Betts, Ruixing Liang, DA Bonn, WN Hardy, et al. Quasiparticle mass enhancement approaching optimal doping in a high-T_c superconductor. *Science*, 348(6232):317–320, 2015.

[57] Mun K Chan, Ross D McDonald, Brad J Ramshaw, Jon B Betts, Arkady Shekhter, Eric D Bauer, and Neil Harrison. Extent of fermi-surface reconstruction in the high-temperature superconductor HgBa2CuO4+ δ. *Proceedings of the National Academy of Sciences*, 117(18):9782–9786, 2020.

[58] S. Blanco-Canosa, A. Frano, E. Schierle, J. Porras, T. Loew, M. Minola, M. Bluschke, E. Weschke, B. Keimer, and M. Le Tacon. Resonant x-ray scattering study of charge-density wave correlations in $YBa_2Cu_3O_{6+x}$. *Phys. Rev. B*, 90:054513, Aug 2014.

[59] JM Tranquada, JD Axe, N Ichikawa, AR Moodenbaugh, Y Nakamura, and S Uchida. Coexistence of, and competition between, superconductivity and charge-stripe order in $La_{1.6-x}Nd_{0.4}Sr_xCuO_4$. *Physical Review Letters*, 78(2):338–341, 1997.

[60] Mehdi Frachet, Igor Vinograd, Rui Zhou, Siham Benhabib, Shangfei Wu, Hadrien Mayaffre, Steffen Kramer, Sanath K. Ramakrishna, Arneil P. Reyes, Jerome Debray, Tohru Kurosawa, Naoki Momono, Migaku Oda, Seiki Komiya, Shimpei Ono, Masafumi Horio, Johan Chang, Cyril Proust, David LeBoeuf, and Marc-Henri Julien. Hidden magnetism at the pseudogap critical point of a cuprate superconductor. *Nature Physics*, 16(10):1064–1068, OCT 2020.

[61] So Kunisada, Shunsuke Isono, Yoshimitsu Kohama, Shiro Sakai, Cédric Bareille, Shunsuke Sakuragi, Ryo Noguchi, Kifu Kurokawa, Kenta Kuroda, Yukiaki Ishida, et al. Observation of small Fermi pockets protected by clean CuO_2 sheets of a high-T_c superconductor. *Science*, 369(6505):833–838, 2020.

[62] P. Bourgeois-Hope, S. Y. Li, F. Laliberté, S. Badoux, S. M. Hayden, N. Momono, T. Kurosawa, K. Yamada, H. Takagi, Nicolas Doiron-Leyraud, and Louis Taillefer. Link between magnetism and resistivity upturn in cuprates: a thermal conductivity study of $La_{2-x}Sr_xCuO_4$. *arXiv:1910.08126*, 2019.

[63] Mathias S Scheurer, Shubhayu Chatterjee, Wei Wu, Michel Ferrero, Antoine Georges, and Subir Sachdev. Topological order in the pseudogap metal. *Proceedings of the National Academy of Sciences*, 115(16):E3665–E3672, 2018.

[64] PA Goddard, SJ Blundell, J Singleton, RD McDonald, A Ardavan, A Narduzzo, JA Schlueter, AM Kini, and T Sasaki. Angle-dependent magnetoresistance of the

layered organic superconductor κ-(et) 2 cu (ncs) 2: Simulation and experiment. *Physical Review B*, 69(17):174509, 2004.

[65] Kunihiko Yamaji. On the angle dependence of the magnetoresistance in quasi-two-dimensional organic superconductors. *Journal of the Physical Society of Japan*, 58(5):1520–1523, 1989.

[66] M Abdel-Jawad, MP Kennett, L Balicas, A Carrington, AP Mackenzie, RH McKenzie, and NE Hussey. Anisotropic scattering and anomalous normal-state transport in a high-temperature superconductor. *Nature Physics*, 2(12):821–825, 2006.

[67] John Singleton. Studies of quasi-two-dimensional organic conductors based on BEDT-TTF using high magnetic fields. *Reports on Progress in Physics*, 63(8):1111–1207, 2000.

[68] MV Kartsovnik, T Helm, C Putzke, F Wolff-Fabris, I Sheikin, S Lepault, Cyril Proust, D Vignolles, N Bittner, W Biberacher, et al. Fermi surface of the electron-doped cuprate superconductor $Nd_{2-x}Ce_xCuO_4$ probed by high-field magnetotransport. *New Journal of Physics*, 13(1):015001, 2011.

[69] B Michon, C Girod, S Badoux, J Kačmarčík, Q Ma, M Dragomir, HA Dabkowska, BD Gaulin, J-S Zhou, S Pyon, et al. Thermodynamic signatures of quantum criticality in cuprate superconductors. *Nature*, 567(7747):218–222, 2019.

[70] T Adachi, Takashi Noji, and Yoji Koike. Crystal growth, transport properties, and crystal structure of the single-crystal $La_{2-x}Ba_xCuO_4$(x= 0.11). *Physical Review B*, 64(14):144524, 2001.

[71] David LeBoeuf, Nicolas Doiron-Leyraud, Julien Levallois, Ramzy Daou, J-B Bonnemaison, NE Hussey, Luis Balicas, BJ Ramshaw, Ruixing Liang, DA Bonn, WN Hardy, S Adachi, Cyril Proust, and Louis Taillefer. Electron pockets in the fermi surface of hole-doped high-T_c superconductors. *Nature*, 450(7169):533–536, 2007.

[72] Takuya Noda, Hiroshi Eisaki, and Shin-ichi Uchida. Evidence for one-dimensional charge transport in $La_{2-x-y}Nd_ySr_xCuO_4$. *Science*, 286(5438):265–268, 1999.

[73] B. Michon, A. Ataei, P. Bourgeois-Hope, C. Collignon, S. Y. Li, S. Badoux, A. Gourgout, F. Laliberté, J.-S. Zhou, Nicolas Doiron-Leyraud, and Louis Taillefer. Wiedemann-Franz Law and Abrupt Change in Conductivity across the Pseudogap Critical Point of a Cuprate Superconductor. *Phys. Rev. X*, 8:041010, Oct 2018.

[74] Sudip Chakravarty, Asle Sudbø, Philip W Anderson, and Steven Strong. Interlayer tunneling and gap anisotropy in high-temperature superconductors. *Science*, 261(5119):337–340, 1993.

[75] Elihu Abrahams and CM Varma. What angle-resolved photoemission experiments tell about the microscopic theory for high-temperature superconductors. *Proceedings of the National Academy of Sciences*, 97(11):5714–5716, 2000.

[76] JG Analytis, M Abdel-Jawad, L Balicas, MMJ French, and NE Hussey. Angle-dependent magnetoresistance measurements in $Tl_2Ba_2CuO_{6+\delta}$ and the need for anisotropic scattering. *Physical Review B*, 76(10):104523, 2007.

[77] Christoph Bergemann, SR Julian, AP Mackenzie, S NishiZaki, and Y Maeno. Detailed topography of the fermi surface of Sr_2RuO_4. *Physical review letters*, 84(12):2662, 2000.

[78] Matthew Newville, Till Stensitzki, Daniel B. Allen, and Antonino Ingargiola. LMFIT: Non-Linear Least-Square Minimization and Curve-Fitting for Python, September 2014.

[79] Michael Vershinin, Shashank Misra, S Ono, Y Abe, Yoichi Ando, and Ali Yazdani. Local ordering in the pseudogap state of the high-T_c superconductor $Bi_2Sr_2CaCu_2O_{8+\delta}$. *Science*, 303(5666):1995–1998, 2004.

[80] Tao Wu, Hadrien Mayaffre, Steffen Krämer, Mladen Horvatić, Claude Berthier, WN Hardy, Ruixing Liang, DA Bonn, and Marc-Henri Julien. Magnetic-field-induced

charge-stripe order in the high-temperature superconductor $YBa_2Cu_3O_y$. *Nature*, 477(7363):191–194, 2011.

[81] Suchitra E Sebastian, N Harrison, FF Balakirev, MM Altarawneh, PA Goddard, Ruixing Liang, DA Bonn, WN Hardy, and GG Lonzarich. Normal-state nodal electronic structure in underdoped high-T_c copper oxides. *Nature*, 511(7507):61–64, 2014.

[82] Andrea Allais, Debanjan Chowdhury, and Subir Sachdev. Connecting high-field quantum oscillations to zero-field electron spectral functions in the underdoped cuprates. *Nature communications*, 5(1):5771, 2014.

[83] Mun K Chan, Neil Harrison, Ross David Mcdonald, BJ Ramshaw, Kim Ann Modic, N Barišić, and Martin Greven. Single reconstructed fermi surface pocket in an underdoped single-layer cuprate superconductor. *Nature communications*, 7(1):12244, 2016.

[84] Scott C Riggs, O Vafek, JB Kemper, JB Betts, A Migliori, FF Balakirev, WN Hardy, Ruixing Liang, DA Bonn, and GS Boebinger. Heat capacity through the magnetic-field-induced resistive transition in an underdoped high-temperature superconductor. *Nature Physics*, 7(4):332–335, 2011.

[85] Subir Sachdev and Rolando La Placa. Bond order in two-dimensional metals with antiferromagnetic exchange interactions. *Physical review letters*, 111(2):027202, 2013.

[86] C. Collignon, A. Ataei, A. Gourgout, S. Badoux, M. Lizaire, A. Legros, S. Licciardello, S. Wiedmann, J.-Q. Yan, J.-S. Zhou, Q. Ma, B. D. Gaulin, Nicolas Doiron-Leyraud, and Louis Taillefer. Thermopower across the phase diagram of the cuprate $La_{1.6-x}Nd_{0.4}Sr_xCuO_4$: Signatures of the pseudogap and charge density wave phases. *Phys. Rev. B*, 103:155102, Apr 2021.

[87] Nicolas Doiron-Leyraud, S. Lepault, O. Cyr-Choinière, B. Vignolle, G. Grissonnanche, F. Laliberté, J. Chang, N. Barišić, M. K. Chan, L. Ji, X. Zhao, Y. Li, M. Greven,

C. Proust, and Louis Taillefer. Hall, seebeck, and nernst coefficients of underdoped $HgBa_2CuO_{4+\delta}$: Fermi-surface reconstruction in an archetypal cuprate superconductor. *Phys. Rev. X*, 3:021019, Jun 2013.

[88] Xiao-Gang Wen and Patrick A. Lee. Theory of underdoped cuprates. *Phys. Rev. Lett.*, 76:503–506, Jan 1996.

[89] Sudip Chakravarty, RB Laughlin, Dirk K Morr, and Chetan Nayak. Hidden order in the cuprates. *Physical Review B*, 63(9):094503, 2001.

[90] T Maurice Rice, Kai-Yu Yang, and Fu-Chun Zhang. A phenomenological theory of the anomalous pseudogap phase in underdoped cuprates. *Reports on Progress in Physics*, 75(1):016502, 2011.

[91] JG Storey. Hall effect and fermi surface reconstruction via electron pockets in the high-T_c cuprates. *EPL (Europhysics Letters)*, 113(2):27003, 2016.

[92] André-Marie S Tremblay. Two-particle-self-consistent approach for the hubbard model. In *Strongly Correlated Systems*, pages 409–453. Springer, 2012.

[93] S Badoux, W Tabis, F Laliberté, G Grissonnanche, B Vignolle, D Vignolles, Jerome Béard, DA Bonn, WN Hardy, R Liang, et al. Change of carrier density at the pseudogap critical point of a cuprate superconductor. *Nature*, 531(7593):210–214, 2016.

[94] Zi-Xiang Li and Dung-Hai Lee. The thermal hall conductance of two doped symmetry-breaking topological insulators. *arXiv preprint arXiv:1905.04248*, 2019.

[95] Sylvia K. Lewin and James G. Analytis. Angle-dependent magnetoresistance oscillations of cuprate superconductors in a model with fermi surface reconstruction and magnetic breakdown. *Phys. Rev. B*, 92:195130, Nov 2015.

[96] David Sénéchal and A-MS Tremblay. Hot spots and pseudogaps for hole-and electron-doped high-temperature superconductors. *Physical review letters*, 92(12):126401, 2004.

[97] D. J. Scalapino. A common thread: The pairing interaction for unconventional superconductors. *Rev. Mod. Phys.*, 84:1383–1417, Oct 2012.

[98] Wei Wu, Michel Ferrero, Antoine Georges, and Evgeny Kozik. Controlling Feynman diagrammatic expansions: Physical nature of the pseudogap in the two-dimensional Hubbard model. *Phys. Rev. B*, 96:041105, Jul 2017.

[99] Yuval Gannot, Brad J Ramshaw, and Steven A Kivelson. Fermi surface reconstruction by a charge density wave with finite correlation length. *Physical Review B*, 100(4):045128, 2019.

[100] S. Badoux, S. A. A. Afshar, B. Michon, A. Ouellet, S. Fortier, D. LeBoeuf, T. P. Croft, C. Lester, S. M. Hayden, H. Takagi, K. Yamada, D. Graf, N. Doiron-Leyraud, and Louis Taillefer. Critical doping for the onset of fermi-surface reconstruction by charge-density-wave order in the cuprate superconductor $La_{2-x}Sr_xCuO_4$. *Phys. Rev. X*, 6:021004, Apr 2016.

[101] Carsten Putzke, Siham Benhabib, Wojciech Tabis, Jake Ayres, Zhaosheng Wang, Liam Malone, Salvatore Licciardello, Jianming Lu, Takeshi Kondo, Tsunehiro Takeuchi, Nigel E. Hussey, John R. Cooper, and Antony Carrington. Reduced hall carrier density in the overdoped strange metal regime of cuprate superconductors. *Nature Physics*, 17:826–831, 2021.

[102] M. Lizaire, A. Legros, A. Gourgout, S. Benhabib, S. Badoux, F. Laliberté, M.-E. Boulanger, A. Ataei, G. Grissonnanche, D. LeBoeuf, S. Licciardello, S. Wiedmann, S. Ono, H. Raffy, S. Kawasaki, G.-Q. Zheng, N. Doiron-Leyraud, C. Proust, and L. Taillefer. Transport signatures of the pseudogap critical point in the cuprate superconductor $Bi_2Sr_{2-x}La_xCuO_{6+\delta}$. *Phys. Rev. B*, 104:014515, Jul 2021.

[103] Hiroaki Shishido, Rikio Settai, Hisatomo Harima, and Yoshichika Ōnuki. A drastic

change of the Fermi surface at a critical pressure in $CeRhIn_5$: dHvA study under pressure. *Journal of the Physical Society of Japan*, 74(4):1103–1106, 2005.

[104] P. Walmsley, C. Putzke, L. Malone, I. Guillamón, D. Vignolles, C. Proust, S. Badoux, A. I. Coldea, M. D. Watson, S. Kasahara, Y. Mizukami, T. Shibauchi, Y. Matsuda, and A. Carrington. Quasiparticle Mass Enhancement Close to the Quantum Critical Point in $BaFe_2(As_{1-x}P_x)_2$. *Phys. Rev. Lett.*, 110:257002, Jun 2013.

[105] S Uji, JS Brooks, M Chaparala, S Takasaki, J Yamada, and H Anzai. Rapid oscillation and fermi-surface reconstruction due to spin-density-wave formation in the organic conductor$(TMTSF)_2PF_6$. *Physical Review B*, 55(18):12446, 1997.

[106] James G. Analytis, Ross D. McDonald, Jiun-Haw Chu, Scott C. Riggs, Alimamy F. Bangura, Chris Kucharczyk, Michelle Johannes, and I. R. Fisher. Quantum oscillations in the parent pnictide $BaFe_2As_2$: Itinerant electrons in the reconstructed state. *Phys. Rev. B*, 80:064507, Aug 2009.

[107] B Friess, V Umansky, K Von Klitzing, and JH Smet. Current flow in the bubble and stripe phases. *Physical review letters*, 120(13):137603, 2018.

[108] I. V. Kukushkin, V. Umansky, K. von Klitzing, and J. H. Smet. Collective modes and the periodicity of quantum hall stripes. *Phys. Rev. Lett.*, 106:206804, May 2011.

[109] Yang Xu, Song Liu, Daniel A. Rhodes, Kenji Watanabe, Takashi Taniguchi, James Hone, Veit Elser, Kin Fai Mak, and Jie Shan. Correlated insulating states at fractional fillings of moiré superlattices. *Nature*, 587(7833):214–218, November 2020.

[110] Yuan Cao, Valla Fatemi, Ahmet Demir, Shiang Fang, Spencer L Tomarken, Jason Y Luo, Javier D Sanchez-Yamagishi, Kenji Watanabe, Takashi Taniguchi, Efthimios Kaxiras, et al. Correlated insulator behaviour at half-filling in magic-angle graphene superlattices. *Nature*, 556(7699):80–84, 2018.

[111] J. R. Lane, L. Zhang, M. A. Khasawneh, B. N. Zhou, E. A. Henriksen, and J. Pollanen. Flip-chip gate-tunable acoustoelectric effect in graphene. *Journal of Applied Physics*, 124(19):194302, November 2018. arXiv: 1801.05270.

[112] Masahiko Yokoi, Satoshi Fujiwara, Tomoya Kawamura, Tomonori Arakawa, Kazushi Aoyama, Hiroshi Fukuyama, Kensuke Kobayashi, and Yasuhiro Niimi. Negative resistance state in superconducting nbse2 induced by surface acoustic waves. *Science advances*, 6(34):eaba1377, 2020.

[113] A. Wixforth, J. Scriba, M. Wassermeier, J. P. Kotthaus, G. Weimann, and W. Schlapp. Surface acoustic waves on GaAs/$Al_xGa_{1-x}As$ heterostructures. *Physical Review B*, 40(11):7874–7887, October 1989.

[114] MF Lewis. On rayleigh waves and related propagating acoustic waves. In *Rayleigh-Wave Theory and Application*, pages 37–58. Springer, 1985.

[115] AR Hutson and Donald L White. Elastic wave propagation in piezoelectric semiconductors. *Journal of Applied Physics*, 33(1):40–47, 1962.

[116] Robert Adler. Simple theory of acoustic amplification. *IEEE Transactions on Sonics and Ultrasonics*, 18(3):115–118, 1971.

[117] David Morgan. *Surface acoustic wave filters: With applications to electronic communications and signal processing*. Academic Press, 2010.

[118] B. Friess, Y. Peng, B. Rosenow, F. von Oppen, V. Umansky, K. von Klitzing, and J. H. Smet. Negative permittivity in bubble and stripe phases. *Nature Physics*, 13(11):1124–1129, November 2017.

[119] Christian Rembe, Georg Siegmund, Heinrich Steger, and Michael Wörtge. Measuring mems in motion by laser doppler vibrometry. In *Optical inspection of microsystems*, pages 297–347. CRC Press, 2019.

[120] W.H. Haydl, P. Hiesinger, R.S. Smith, B. Dischler, and K. Heber. Design of quartz and lithium niobate saw resonators using aluminum metallization. In *30th Annual Symposium on Frequency Control*, pages 346–357, 1976.

[121] WILLIAM H Haydl. Surface wave reflection from right angle corners in gallium arsenide. pages 363–368, 1973.

[122] DZ Tsang and MS Dresselhaus. The c-axis electrical conductivity of kish graphite. *Carbon*, 14(1):43–46, 1976.

[123] D.L.T. Bell and R.C.M. Li. Surface-acoustic-wave resonators. *Proceedings of the IEEE*, 64(5):711–721, 1976.

[124] Lei Wang, I Meric, PY Huang, Q Gao, Y Gao, H Tran, T Taniguchi, Kenji Watanabe, LM Campos, DA Muller, et al. One-dimensional electrical contact to a two-dimensional material. *Science*, 342(6158):614–617, 2013.

[125] Andrea F Young, Cory R Dean, Lei Wang, Hechen Ren, Paul Cadden-Zimansky, Kenji Watanabe, Takashi Taniguchi, James Hone, Kenneth L Shepard, and Philip Kim. Spin and valley quantum hall ferromagnetism in graphene. *Nature Physics*, 8(7):550–556, 2012.

[126] Per Delsing, Andrew N Cleland, Martin JA Schuetz, Johannes Knörzer, Géza Giedke, J Ignacio Cirac, Kartik Srinivasan, Marcelo Wu, Krishna Coimbatore Balram, Christopher Bäuerle, et al. The 2019 surface acoustic waves roadmap. *Journal of Physics D: Applied Physics*, 52(35):353001, 2019.

[127] C. R. Dean, A. F. Young, I. Meric, C. Lee, L. Wang, S. Sorgenfrei, K. Watanabe, T. Taniguchi, P. Kim, K. L. Shepard, and J. Hone. Boron nitride substrates for high-quality graphene electronics. *Nature Nanotechnology*, 5(10):722–726, October 2010.

[128] D. Hatanaka, M. Asano, H. Okamoto, Y. Kunihashi, H. Sanada, and H. Yamaguchi. On-Chip Coherent Transduction between Magnons and Acoustic Phonons in Cavity Magnomechanics. *Physical Review Applied*, 17(3):034024, March 2022.

[129] Youngwook Kim, Ajit C. Balram, Takashi Taniguchi, Kenji Watanabe, Jainendra K. Jain, and Jurgen H. Smet. Even denominator fractional quantum Hall states in higher Landau levels of graphene. *Nature Physics*, 15(2):154–158, February 2019.